FUNDAMENTALS OF LASER COOLING OF RARE-EARTH-ION DOPED SOLIDS AND ITS ENHANCEMENT USING NANOPOWDERS

by

Xiulin Ruan

A dissertation submitted in partial fulfillment
of the requirements for the degree of
Doctor of Philosophy
(Mechanical Engineering)
in the University of Michigan
2007

Doctoral Committee:

Professor Massoud Kaviany, Chair
Professor John Kieffer
Professor Stephen C. Rand
Assistant Professor David A. Reis

Acknowledgements

My time at Michigan has tremendous impacts on me, and for this I would like to thank many. My advisor, Professor Massoud Kaviany, led me into the exciting area of heat transfer physics, and encouraged me to take risks to explore new topics. I was allowed sufficient freedom to decide where the project should direct, while I could still benefit a lot from his insight and expertise. I am grateful to him for training me in every aspect to become a scholar. My committee member, Professor Stephen Rand, taught me a great deal when I was a newcomer to optics, and offered to meet with me many times all through my Ph.D. study, to discuss questions in my research. The other members of my committee, Professors John Kieffer, and David Reis, have provided support during the dissertation process. Professors Mahta Moghaddam, Gerard Mourou, Stephen Rand, David Reis, Duncan Steel, and James Wells taught courses that were very helpful to me for learning optics, quantum mechanics, and condensed matter physics. I would also like to thank the valuable discussions or communications with Barry Dunietz, Stephen Fahy, James Foresman, Bernd Kallies, Roberto Merlin, Richard Powell, Shawn Redmond, Juan F. Rivas, and Anton Van der Ven.

I have met many great people in Ann Arbor, and I would especially like to acknowledge Alan McGaughey, Luciana da Silva, Paddy K.L. Chan, Jin-Hyun Nam, Baoling Huang, Gi-Suk Hwang, and Jedo Kim. Special thanks go to my wife Limin Zhang and my parents, without whose support and understanding this work would not have been possible.

This work is partly supported by the Rackham Graduate School at the University of Michigan, through a Pre-doctoral Fellowship.

Table of Contents

List of Figures

List of Tables

Nomenclature

a_{i-p}	ion-phonon coupling constant
$B_{e,a}$	excitation coefficient (1/(s-J/m^3))
c_{o}	speed of light in vaccum (m/s)
D_p	phonon density of states (1/m^3)
d_s	diameter of the solid particle (m)
E	complex electric field (V/m)
$\dot{E}$	energy flow rate (W)
E_{pump}	pumping energy (J)
e_e	electron charge (C)
$e_{ph,i}$	energy density of the pumping field (J/m^3)
$\boldsymbol{e}_\alpha$	unit photon polarization vector
$f_p,\ f_{ph}$	phonon, photon distribution function
H	Hamiltonian (J)
$\hbar$	Planck constant/2π, 1.0546×10^{-34} J-s
I	intensity (W/m^2)
k	wave vector (1/m), thermal conductivity (W/m-K)

k_{B}	Boltzmann constant, 1.3806×10^{-23} J/K
L	optical pathlength, (m)
l	index of the layers
M	interaction matrix
m_f, m_s	complex refractive index of fluid, solid
N	number of layers
N_p	number of phonons
n_a, n_b	electronic population at the ground and excited states (cm^{-3})
n_d	dopant concentration, (cm^{-3})
n_f, n_s	refractive index of fluid, solid
Q	power (W)
q	charge (C)
r	interatomic distance (m)
$\dot{s}$	energy conversion per unit volume ($\mathrm{W/m}^3$)
$\dot{S}$	energy conversion (W)
T	temperature (K)
t	time (s)
$\mathbf{u}_{i_\beta}$	velocity of particle i_β (m/s)
u_p, u_{ph}	speed of phonon, photon (m/s)
V	volume (m^3)

Greek symbols

$\alpha_{ph,i}$	absoptance
δ_{D}	Dirac delta function (1/J)
Γ	velocity autocorrelation function
$\dot{\gamma}$	transition rate (1/s)
$\dot{\gamma}_{e,a}$	transition probability per unit time per unit energy density [1/s/(J/m^3)])
ϵ_e	electronic permittivity (F/m)
ε	porosity
η_c	cooling efficiency
η_{e-ph}	quantum efficiency
κ_s	index of extinction of solid
λ	wavelength (m)
l_m	photon mean free path (m)
μ	magnetic permeability (H/m)
$\boldsymbol{\mu}_e$	electronic transition dipole moment (C m)
ρ	mass density (kg/m^3)
$\sigma_{ph,a}$	absorption coefficient (1/m)
τ	lifetime (s)
φ	potential energy (J)
ψ	wavefunction
ω	angular frequency (rad/s)

Subscripts

a	absorption, ground state
b	excited state
C	Carnot
c	critical
d	decay, dopant
E	energy
e	emission, electron
F	flux
f	fluid, final state, fluorescence
i	incident, initial state
ion	ion
m	mediate
nr	non-radiative
o	free space
p	phonon
ph	photon
r	radiative, real part of a complex number
S	entropy
s	solid
t	thermal
0	incident frequency ω_0

Superscripts

o	equilibrium

Abbreviations

BKS	van Beest-Kramer-van Santen
BTE	Boltzmann transport equation
DFT	density functional theory
DOS	density of states
EMS	electromagnetic statistical
ERT	equation of radiative transfer
FDTD	finite-difference time-domain
MD	molecular dynamics
QC	quadratic convergent
SCF	self consistent function
TD	time dependent

Abstract

Chair: Massoud Kaviany

The Fermi golden rule is applied as the primary theory for laser cooling of solids, by recognizing that the absorption is a photon-induced, phonon-assisted, electronic transition. The limiting factors are identified as the coupling and population of the energy carriers (photon, electron, and phonon), which include the photon-electron coupling, electron-phonon coupling, ion-dopant concentration, phonon density of states, and the photon population.

The photon-electron and electron-vibration coupling rates for ion-doped materials are calculated using ab initio methods for the first time. Using the calculated first-principle wavefunctions, the electric transition dipole moment between the ground and excited states is determined by its definition. The electron-phonon coupling is calculated by taking into account the modification of the electronic wavefunction in response to the nuclei motion, and the modifications of the vibrational modes before and after the transition. This ab initio approach does not require any fitting to experiment, providing a theoretical foundation for the optimal selection of laser

cooling materials (both dopant and host).

Nanostructure is proposed for the first time to enhance laser cooling performance, through the optimization of carrier populations using nanopowders. The concept of optimum dopant concentration is established and determined using the energy transfer theory, and is found to be larger than that currently used. The phonon density of states of nanopowders, calculated using molecular dynamics simulations, exhibits broadened modes, and extended tails at low and high frequencies. This is advantageous over the bulk material since more phonon modes are available in the desired range. The pumping field energy is calculated by solving the Maxwell equations in random nanopowder media. Photons are multiply scattered and do not propagate through the medium, and large field enhancement is observed. This leads to the trapping of more photons in nanopowder media, compared to the bulk material, implying more efficient absorption and cooling performance. Due to these enhancement effects, thermal predictions show that nanopowders can be cooled to the cryogenic temperature range, for the first time.

Chapter 1

Introduction

1.1 History and background

Cooling is a process in which thermal energy is absorbed from a lower temperature reservoir and is deposited to a higher temperature reservoir, by consuming a small amount of higher grade energy. Mechanical, electrical, and optical energies are among the high grade energies, and are expected to be used for cooling purpose. Gas compression refrigerators, which consume mechanical energy, and thermoelectric coolers, which consume electrical energy, are matured techniques which have found very broad applications. High grade optical energies like lasers are, however, well-known for their heating effects rather than cooling capabilities. In fact, gases have been cooled to the order of nano-Kelvin by lasers, and this technique resulted in the 1997 and 2001 Nobel Prizes in Physics [9, 10, 11, 12]. Its counterpart, laser cooling of solids, has also attracted great interests recently, for the potential to develop an optical cryocooler for important applications such as the cooling of electronic devices.

The concept of laser cooling (optical refrigeration) of solids dates back to 1929, when Pringsheim recognized that thermal vibrational energy (phonon) can be removed by the anti-Stokes fluorescence, i.e., the average energy of the emitted photons is higher than that of the absorbed photons [13]. Initially, it was believed that optical cooling by the anti-Stokes fluorescence contradicted the second law of thermodynamics. Predictions suggested that the cycle of excitation and fluorescence was reversible, and hence the optical refrigeration indicated an 100% transformation of heat into work [14, 15]. This issue was cleared by Landau by assigning entropy to radiation [16]. It was shown that the entropy of a radiation field increases with its frequency bandwidth and also the solid angle through which it propagates. Since the incident laser light has a very small bandwidth and propagates in a well-defined direction, it has almost zero entropy. On the other hand, the fluorescence is relatively broadband and is emitted in all directions, and therefore, it has a comparatively larger entropy. In this way, the second law of thermodynamics is satisfied. A detailed analysis is given in Chapter 2.

Many attempts have been made to realize radiative refrigeration experimentally, and the associated theoretical interpretations have been discussed. The earliest experiment was performed by Kushida and Geusic on Nd: YAG [17]. Reduced heating other than net cooling was observed, which was suggested to be a result of the impurities in the crystal and multiphonon decay in the optical transition. Later Djeu and Whitney laser cooled low-pressure CO_2 by 1 K from 600 K by using a CO_2 laser for pumping [18]. In 1995, Epstein et al. [1] reported the first successful experiment of laser cooling in solids. Since then, various Yb or Tm doped glasses and crystals have

been cooled [19, 20, 21, 2, 22, 23, 24, 25, 26, 27]. Particularly, bulk solids have been cooled from room temperature to 208 K (creating a temperature difference $\Delta T = 92$ K) [27]. Continuous progress has been made [28, 29, 25] towards achieving cryogenic temperatures. For semiconductors, theoretical predictions have shown their potential to be cooled to as low as 50 K starting from room temperature [30], but experimental success is yet to be achieved due to some serious challenges to be overcome.

These progresses, as well as the recent success in laser cooling of gases and the subsequent achievement of Bose-Einstein condensation [9, 10, 11, 12], again stimulated interest in optical cooling of solids.

1.2 Principles of laser cooling of solids

Laser cooling can be viewed as the inverse cycle of lasers, and laser materials are in principle also good candidates for laser cooling. Common laser materials in the solid state include ion-doped solids and semiconductors, which are currently being studied for laser cooling.

In Fig. 1.1(a), the fundamental energy carriers involved in the laser cooling of rare-earth-ion doped solids are shown. The host crystal lattice is idealized as transparent to the pumping laser, while some of the atoms are replaced by optically active, doped ions (eg., Yb^{3+}). The ion is represented by an effective transition dipole moment, which is the matrix element of the dipole operator $e_e\boldsymbol{r}$ [31], i.e.,

$$\boldsymbol{\mu}_e = \int \psi_f^* e_e \boldsymbol{r} \psi_i d^3 r. \tag{1.1}$$

where, e_e is the electron charge, $\boldsymbol{r}$ is the position vector, and ψ_i and ψ_f are the

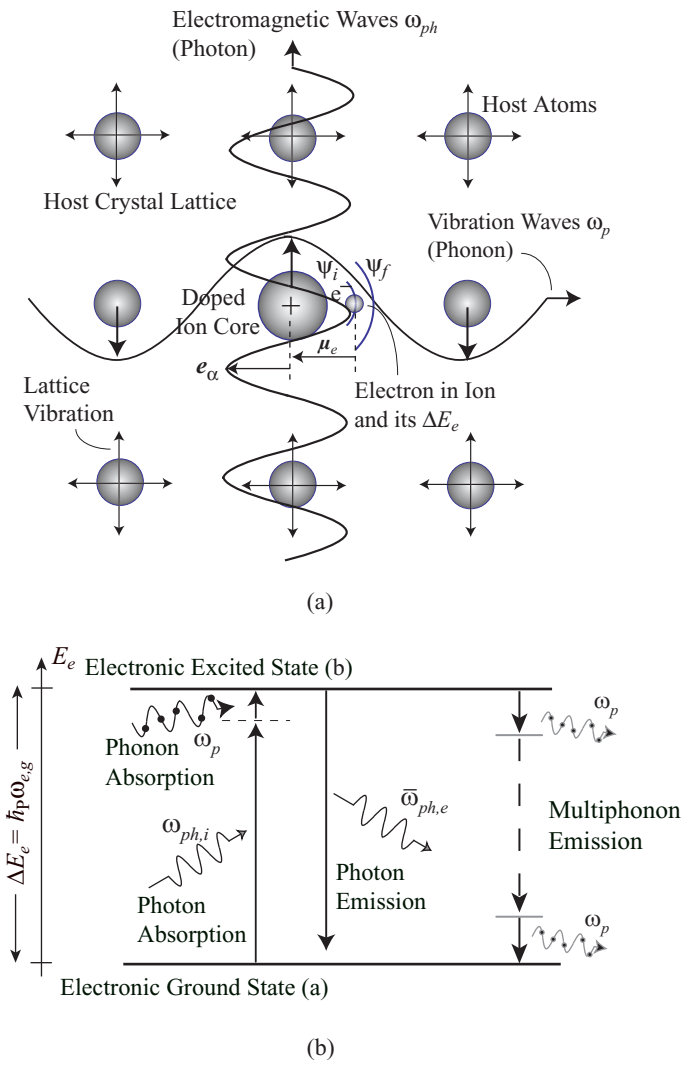

Figure 1.1: (a) Three fundamental energy carriers in rare-earth ion doped solids irradiated by laser light: photons from the pumping fields, phonons from the host crystal, and electrons of the doped ions. (b) Principles of laser cooling in rare-earth ion doped crystal. The electron is excited by absorbing a photon and one or more lattice phonons, and then decays by emitting a higher energy photon.

initial and final state wave functions of the two level system. One can regard this matrix element to couple the states ψ_i and ψ_f, which have different parity, creating or absorbing a photon. The electromagnetic field, which has a polarization vector $\boldsymbol{e}_\alpha$, may interact with the ion if the coupling factor $\boldsymbol{e}_\alpha \cdot \boldsymbol{\mu}_e$ is nonzero (i.e., they are not orthogonal).

Shown in Fig. 1.1(b) are the principles of the photon-electron-phonon interactions which result in the cooling effect in the solid. As the pumping wavelength is tuned to the red side of the resonance, the probability of a purely electronic transition between electronic sublevels, a first order process, becomes smaller. On the other hand, the phonon-assisted transition, a second-order process, starts to contribute significantly to absorption. As a result, the absorption turns out to be a combination of the first- and second-order transitions. Since a much longer pumping wavelength than the resonance is used in laser cooling, the total transition is believed to be dominated by the second-order process. In such a process, the medium is irradiated by laser light with a frequency $\omega_{ph,i}$ that is below the resonance frequency $\omega_{e,g}$ for the energy gap (10,250 cm^{-1} for Yb^{3+} ion in $\mathrm{Y_2O_3}$), the electron may still be excited by absorbing a photon from the pumping field and a phonon with a frequency ω_p from the host, such that $\omega_{ph,i} + \omega_p = \omega_{e,g}$. The electron then undergoes a radiative decay by emitting a photon with a frequency $\omega_{ph,e}$, or undergoes a nonradiative decay by emitting a few phonons (multiphonon relaxation), leading to internal heating of the system. The energy magnitudes of these carriers involved in laser cooling process in Yb^{3+}:$\mathrm{Y_2O_3}$ are shown in Fig. 1.2 [32].

The quantum efficiency $\eta_{e\text{-}ph}$ is defined as the ratio of the radiative decay rate to

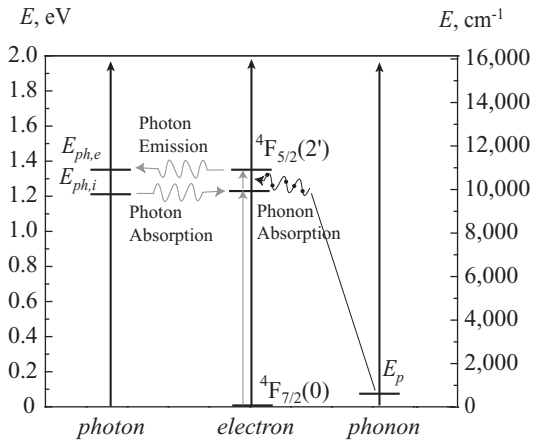

Figure 1.2: Energy spectra of all three carriers in irradiated Yb^{3+}:Y_2O_3. Yb^{3+} has only two main electronic levels: $^4F_{7/2}$ and $^4F_{5/2}$. Carriers may interact with each other as energy and momentum conservations are met.

the total decay rate, or, in this case, the ratio of the number of emitted photons to the number of absorbed photons [32]. The net cooling power per absorbed photon P_c is given by

$$P_c = \eta_{e\text{-}ph}\hbar\bar{\omega}_{ph,e} - \hbar\omega_{ph,i} = \hbar\omega_{ph,i}(\eta_{e\text{-}ph}\frac{\bar{\omega}_{ph,e}}{\omega_{ph,i}} - 1), \tag{1.2}$$

where $\bar{\omega}_{ph,e}$ is the mean frequency of emitted photons. The cooling efficiency is defined as the ratio of the net cooling power and the absorbed power, i.e.,

$$\eta_c = \frac{P_c}{\hbar\omega_{ph,i}} = \eta_{e\text{-}ph}\frac{\bar{\omega}_{ph,e}}{\omega_{ph,i}} - 1. \tag{1.3}$$

Cooling is achieved as η_c is positive. Evidently, high quantum efficiency $\eta_{e\text{-}ph}$ is desirable.

The cooling process in semiconductors, as shown in Fig. 1.3, is similar to that of ion-doped solids. An electron originally in the valence band absorbs a laser photon and is excited to the conduction band, leaving a hole in the valence band. It then gains

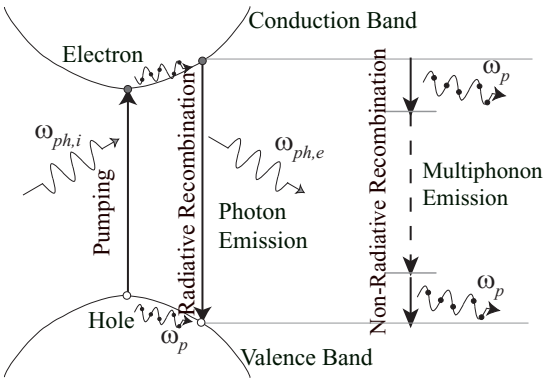

Figure 1.3: Process for laser cooling of a semiconductor in which a laser photon with frequency $\omega_{ph,i}$ is absorbed followed by emission of an up-converted fluorescence photon with frequency $\omega_{ph,e}$.

some energy by absorbing a phonon (intraband absorption) and climbs to a higher position in the conduction band. The electron then decays back to the valence band via either radiative recombination, or nonradiative recombination, which includes multiphonon process and Auger process. The net cooling power is in the same form as Eq. (1.2).

1.3 Macroscale role of laser cooling of solids

In Fig. 1.4, a macroscopic energy diagram is shown for a solid that is cooled by laser, where various energy flows are shown. To minimize the external thermal load to achieve the best cooling effect, in most of the existing experiments the solid was supported by very thin wires and was placed in vacuum, to eliminate the conduction and convection. The only external load is then the thermal radiation from surroundings, as shown in Fig. 1.4.

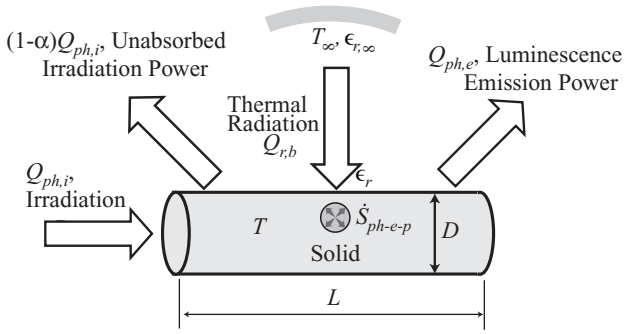

Figure 1.4: The energy diagram for laser cooling of a solid, where radiation is the only external thermal load.

Using Eq. (1.3), the total cooling power $\dot{S}_{ph\text{-}e\text{-}p}$ is given by

$$\dot{S}_{ph\text{-}e\text{-}p} = P_c \frac{Q_{ph,a}}{\hbar\omega_{ph,i}} = \eta_c Q_{ph,a} = \eta_c \alpha Q_{ph,i}, \tag{1.4}$$

where $Q_{ph,a}$ is the absorbed power, $Q_{ph,i}$ is the irradiation power, and α is the absorptivity. This equation links the macroscopic cooling behavior and the atomic level parameters. The results also indicate that the net cooling power $\dot{S}_{ph\text{-}e\text{-}p}$ is proportional to the absorbed power $Q_{ph,a}$.

The steady-state, integral-volume energy equation is

$$\dot{S}_{ph\text{-}e\text{-}p} - Q_{r,b} = 0. \tag{1.5}$$

Assuming that the surface area of the surrounding is much larger than that of the sample, the thermal radiation load $Q_{r,b}$ is given by [33]

$$Q_{r,b} = A_r \epsilon_r \sigma_{\mathrm{SB}} (T_\infty^4 - T^4), \tag{1.6}$$

where A_r is the surface area of the solid, σ_{SB} is the Stefan-Boltzmann constant, and T_∞ is the temperature of the ambient radiation field (or the effective temperature in

case the ambient field does not have a thermal spectra). It is evident that the amount of cooling power $\dot{S}_{ph\text{-}e\text{-}p}$ governs how much the sample temperature can be lowered from the surrounding temperature.

1.4 Applications of laser cooling

Since the process of anti-Stokes fluorescence does not require any mechanical movement, such a solid-state cooler is likely to have a longer lifetime than other coolers. This is particularly useful in space, where reliability and lifetime are crucial considerations.

Despite the low cooling efficiency (2-3% at room temperature so far, and lower efficiency at lower temperatures), laser cooling is a promising candidate for cryocoolers, with the potential to cool ion-doped dielectrics and semiconductors to 50 K or even 10 K starting from room temperature [34]. Predictions have shown that at these cryogenic temperatures, thermoelectric coolers become ineffective or incapable, compared to laser coolers [35].

Another application is in the heat-balanced laser system. This process would employ fluorescence cooling to offset the heat produced in the generation of laser radiation [36, 37, 38, 39, 40, 41].

1.5 Advance in laser cooling of rare-earth ion-doped solids

Ion-doped solids were the first class of materials on which laser actions were demonstrated [42], and were attempted early for laser cooling.

1.5.1 Existing experimental investigations

The earliest experiment was performed on Nd^{3+}:YAG by Geusic et al. at Bell Laboratories in 1968 [17], just a few years after he demonstrated the first laser action in this transition-metal doped crystal [43]. This focused on flash-lamp-pumped crystals of Nd^{3+}:YAG, with the fluorescence from one crystal being used for cooling of another. When compared with an undoped reference sample, the neodymium-doped sample showed reduced heating, but net cooling was not observed. This was conjectured to be due to impurities in the crystals, which offset the cooling effects. A simple model yielded the rate of temperature change, and the results agreed with the experiment. Later laser emissions were realized in rare-earth-ion doped solids, and these materials immediately became attractive for laser cooling purpose, since the optical $4F$ levels are shielded from the surroundings by the filled $5S$ and $5P$ levels, leading to the suppression of the multiphonon relaxation. In 1995, Epstein et al. reported the first experimental success of laser cooling in solids [1]. The absorption and fluorescence spectra were measured, as shown in Fig. 1.5(a), where the mean fluorescence wavelength is marked. As the pumping wavelength was tuned longer than the mean fluorescence wavelength, a local temperature decrease of 0.3 K was

detected, as shown in Fig. 1.5(b). However, the cooling effect diminished when the pumping wavelength is tuned too far away, since the off-resonance absorptivity becomes too small. The cooling efficiency achieved was up to 2%. Mungan et al. used optical fibre which is a favorable geometry for cooling and obtained a temperature decrease of 16 K [44]. Gosnell again cooled this fiber by 65 K from room temperature [2]. His experimental apparatus was very carefully designed, as shown in Fig. 1.6. Fernandez et al cooled ytterbium-doped glasses by nearly 70 K below room temperature [22]. This record was again pushed to 92 K below room temperature by Epstein in 2005 [27]. Besides room temperature, cooling from lower starting temperature has also been achieved in a number of Yb^{3+}-doped glasses [3]. Using photothermal deflection and spectroscopic techniques, Mungan et al. [19] observed local cooling in a Yb-doped glass at starting temperatures 100-300 K, achieving a cooling efficiency of about 0.01. Fernandez et al [22] also measured local cooling between 77 K and room temperature in Yb^{3+}:CNBZn and Yb^{3+}:BIG samples. Continuous progress has been made [28, 29, 25] towards achieving cryogenic temperatures.

In these experiments, accurate temperature measurements of the cooling sample is very important. As well known, temperature can be measured by contact or noncontact methods, both of which have been used in experiments. A noncontact method, fluorescence thermometry, has been used in many of the existing experiments [1, 2]. It is based on the fact that the fluorescence spectrum of the glass is independent of the pump laser wavelength but only dependent on temperature. A spectrum-temperature relation can be calibrated over a wide range of temperatures using a thermostat. Then the observed spectrum is compared to the reference spectra and the temperature is

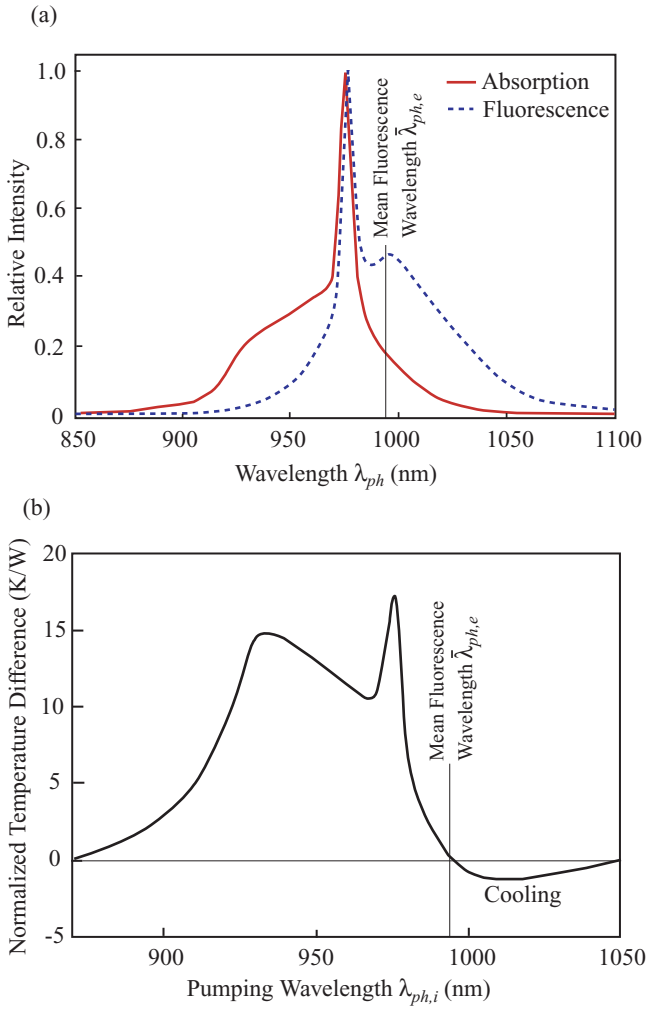

Figure 1.5: (a) The absorption and fluorescence spectra of Yb^{3+}:ZBLANP, with the mean fluorescence wavelength marked [1]. (b) The normalized temperature difference with respect to the pumping wavelength. Cooling is detected as the pumping wavelength is tuned longer than the mean fluorescence wavelength [1].

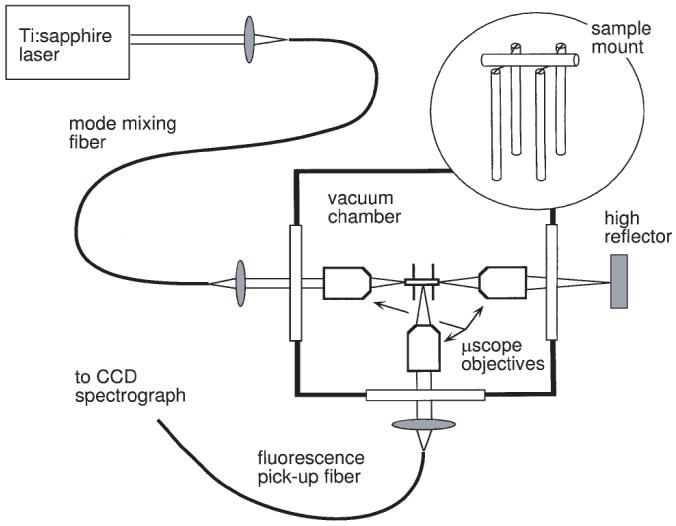

Figure 1.6: Experimental apparatus used for observing laser cooling of Yb:ZBLANP [2]. Pump radiation from a cw Ti:sapphire laser undergoes mode scrambling within an external multimode silica fiber before injection into the sample fiber, which is positioned upon a sample mount (inset), imposing an extremely low conductive thermal load. Unabsorbed pump radiation is collected from the output end of the sample fiber and reinjected into the sample with the help of an external high reflector. Finally, emitted fluorescence is collected with a third internal optic and is spectrally resolved to determine the temperature.

determined. This method is capable of measuring temperature without disturbing the original system, and is very suitable for systems as fine as laser cooling. Thermocouple is another obvious choice for its simplicity. However, it introduces an external thermal load to the cooling element and may reduce or even eliminate the cooling effect. This method is thus usually used for a rough examination of whether or not the system can be cooled, but not for an accurate temperature measurement [21].

To enhance laser cooling performance, one perspective is finding new materials, including dopants and hosts. Thulium-doped glasses are good candidates, since

thulium has a transition resonance at 1.8 μm, whereas the ytterbium transition is near 1 μm. Then the Thulium system is capable of obtaining the same amount of cooling power with a much smaller pumping photon energy. Hoyt et al. showed cooling of a sample of Tm^{3+}-doped ZBLANP by 1.2 K from room temperature, under vacuum, when approximately 3 W of laser power at 1.9 μm was incident on the sample from a periodically-poles lithium-niobate-based optical parametric oscillator in turn pumped by a 20-W cw Nd:YAG laser. Their results indicated a cooling efficiency of 3.4%, which compared favorably with the efficiencies achieved for ytterbium doped glasses. To date, Yb^{3+} and Tm^{3+} are the only two rare-earth elements on which laser cooling has been demonstrated, although some other elements are considered to be good candidates.

A number of ytterbium-doped crystal hosts were also investigated by Bowman and Mungan [28], to determine which of them can be cooled. Besides a number that did not exhibit net cooling, they found that crystals of ytterbium -doped $KGd(WO_4)_2$ can indeed be cooled. This was the first demonstration of anti-Stokes laser cooling of a crystal. Fernandez et al. achieved internal cooling of other ytterbium doped glasses (CNBZn and BIG)[22, 45]. Recently, another set of results showing cooling of crystals was reported by Epstein et al. [23]. These results show cooling of 2.3% ytterbium-doped YAG crystals and 3% ytterbium-doped Y_2SiO_5. A comparison is made with ytterbium-doped ABLAN, which shows that the cooling efficiency is slightly larger in ZBLAN, but the thermal and mechanical properties of YAG may be advantageous for some applications. Several other groups have tried to find other materials suitable for cooling, but even materials that have shown promise from an analysis of their absorp-

tion and emission spectra have had either too low a quantum efficiency or excessive absorption due to impurities for cooling to be achieved. Using the experimental data for lifetimes, Hoyt studied the possibility of laser cooling of a few Tm-doped solids, and identified those which have a potential for cooling due to their high quantum efficiencies [3].

Another perspective to enhance the cooling performance is modifying the structure. Gosnell used a long, thin optical fibre as the host, in order to increase the optical pathlength for a larger absorptivity, and to reduce the external thermal load [2]. To further enhance the absorptivity, some researchers [3, 27] placed the sample between two dielectric mirrors of high reflectance at the pumping wavelength only, as shown in Fig. 1.7(a). The laser pumping is then reflected back and forth, while the fluorescence can escape. Recognizing that the mirrors may bring in extra loss, Heeg et al. proposed an alternative approach [46, 26]. By locating the cooling medium inside a laser cavity, it was efficiently pumped by the inherent multipassing and high circulating power of the laser resonator. Recently, we attempted this problem from a new perspective: nanostructure [47]. The medium in our model is a Yb^{3+} doped Y_2O_3 nanopowder, as shown in Fig. 1.7(b). It is predicted that the absorption can be significantly enhanced due to the optimized dopant concentration, the size effect of the phonon density of states, and the multiple scattering of the pumping photons.

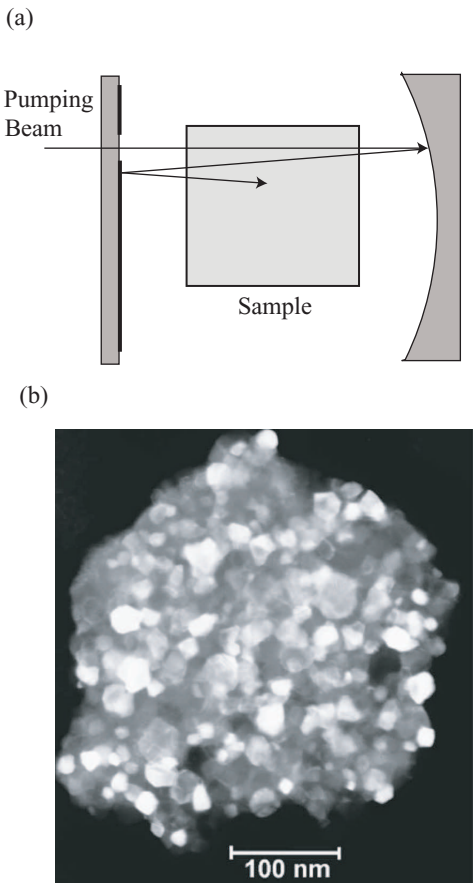

Figure 1.7: Modified structures for enhanced laser cooling performance: (a) Cavity arrangement for multiple passes [3], (b) A micrograph of Yb^{3+}:Y_2O_3 nanopowder [4].

1.5.2 Existing theoretical analyses

The basic principles of laser cooling and its thermodynamic validity provided motivation for the above mentioned experiments. Except for these, more detailed theoretical analysis achieved very limited progress, compared to the rapid improvements of laser cooling experiments. This is mainly due to very complicated physical mechanisms under the laser cooling process. Lamouche considered the temperature dependence of cooling efficiency [5]. By analyzing the temperature dependence of fluorescence and absorption spectra of Yb^{3+}:ZBLAN, they concluded that cooling would

decrease with decreasing temperature, as shown in Fig. 1.8. Fernandez et al. used the Fermi's Golden Rule to interpret their experimental results, by assuming that the absorption is dominated by the phonon-assisted process [22]. The absorption rate $\dot{\gamma}_{e,a}$ is given by

$$\dot{\gamma}_{e,a} = \sum_f \dot{\gamma}_{e,i\text{-}f} = \frac{2\pi}{\hbar_{\mathrm{P}}} \sum_f |M_{fi}|^2 \delta(\hbar_{\mathrm{P}}\omega_{ph,i} + \hbar_{\mathrm{P}}\omega_p - \hbar_{\mathrm{P}}\omega_{e,g}), \tag{1.7}$$

where $\hbar_{\mathrm{P}}\omega_{e,g}$ is the energy difference of the two electronic levels, and M_{fi} is the interaction matrix element. The δ function guarantees the energy conservation, that the sum of the pumping photon energy and the phonon energy should be equal to the electronic gap energy. In this theory, the decreasing cooling efficiency with decreasing temperature is that the phonon distribution function decreases. Heeg et al. investigated the effect of another important factor, the fluorescence reabsorption, on the cooling performance [48, 49]. They used the random-walk model, in which the absorption and fluorescence spectra of Yb^{3+}:ZBLAN are the input data, to determine the fluorescence escape efficiency as well as cooling efficiency. They concluded that moderate concentration and sample size should be used to avoid the dominance of fluorescence reabsorption.

Despite these interesting theoretical studies, a more important issue, if not the most important, is to develop a theory that can provide the guidance for the material selection. Although there are many factors limiting the laser cooling performance, the materials properties, including dopants and hosts, are essential. An ideal dopant-host pair should allow for an effective ion-phonon coupling, which otherwise should not be large enough to result in multiphonon relaxation. To develop such a theoretical

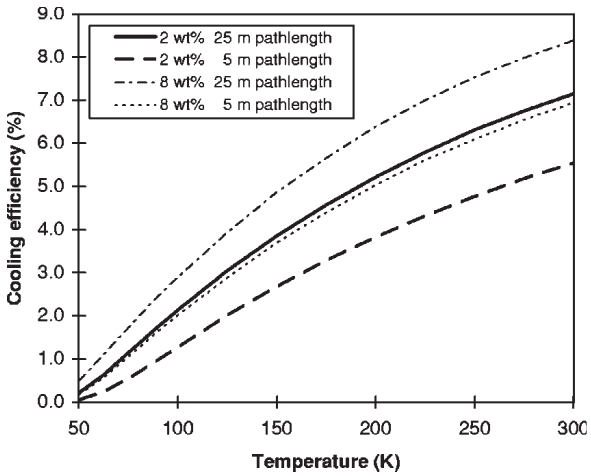

Figure 1.8: Predicted cooling efficiency as a function of temperature, for the 2 and 8 wt % Yb^{3+}:Y_2O_3 in the linear regime for two optical pathlengths [5].

foundation for laser cooling of solids is the primary goal of this study.

1.6 Advance in laser cooling of semiconductors

Given the recent advance in fabrication of semiconductor devices and their use as lasers, it is not surprising that a number of researchers have considered these candidates for optical cooling. Gauck et al considered a GaAs/GaInP heterostructure for possible cooling effects [6]. By using the index-matching technique, they measured an ultrahigh external quantum efficiency of 96% and observed blue-shifted luminescence. Although net cooling was not observed due to heating from nonradiative process, the cooling mechanism was shown to be feasible. Rivlin et al. modelled the absorption of narrow band laser light and the spontaneous emission, and discussed the feasibility of cooling of semiconductors [50]. Finkeiben et al. reported a local temperature drop of 7 K from the liquid nitrogen temperature in a GaAs quantum well [51]. This cooling

effect was due to the luminescence up-conversion mechanism. Sheik-Bahae [30] et al. performed a theoretical analysis considering non-radiative decay and luminescence reabsoption, and proposed the feasibility of laser cooling in semiconductors. Nevertheless, the bulk cooling of semiconductors has not yet been realized experimentally, where the luminescence trapping due to total internal reflection remains the major challenge.

One possible solution is to use an index-matched dome lens attached to the cooling element [6], as shown in Fig. 1.9(a). Since the dome lens is much larger than the heterostructure, the fluorescence emitted at any angle would become nearly normal to the dome surface, making the extraction much more efficiently. The drawback is that the dome lens introduces more external thermal load and increases the system size. Another possible solution is to use a nanogap structure [7], as shown in Fig. 1.9(b). For the onset of the total internal reflection, there exists an evanescent wave on the other side of the surface which has an exponentially decaying amplitude and does not transfer any energy. If another surface is brought closely to the the first one at a distance shorter than the wavelength, the evanescent waves will be coupled to the second surface and become propagating waves. In this way, the originally trapped fluorescence can be efficiently coupled out of the cooling element.

1.7 Summary and discussions

Over the past decade, substantial progress has been made in laser cooling of solids. Cooling of rare-earth-ion doped solids has been demonstrated and improved, and

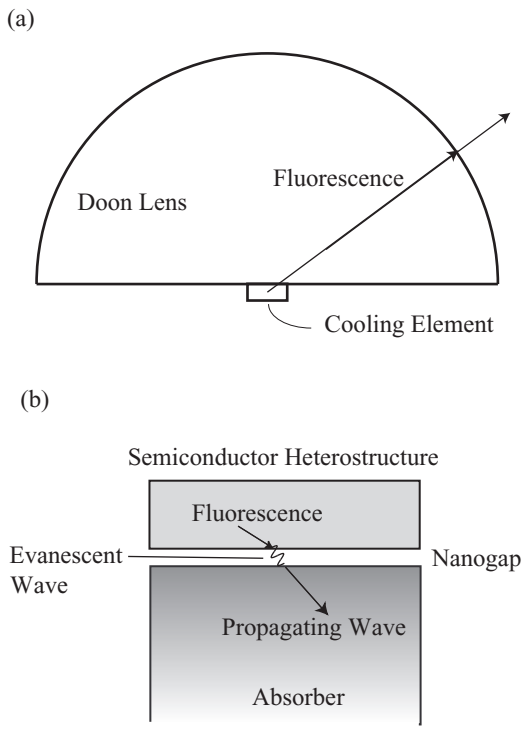

Figure 1.9: Possible structures for extracting the fluorescence from the high refractive-index semiconductors: (a) An index-matching dome lens attached on the cooling element [6], (b) A nanogap structure to couple the evanescent waves out of the cooling element [7].

cooling in semiconductors are anticipated in the near future. Current work is focused on finding new materials and structures that can enhance the cooling performance, or that can be cooled (for semiconductors). Ways are also being explored in which a practical optical cooler might be engineered.

Further research into laser cooling of solids should firstly explore new materials and structures for enhanced cooling performance. Material properties determine the maximum cooling efficiency that can be achieved, so further advances could result from investigation of other dopants, such as thulium and others, to replace ytterbium. Consideration should also be given to other host materials, including crystals

and glasses. New structures such as nanostructure are promising due to the quantum size effect, and should be considered as a major direction. Given the rate of advancement of semiconductor manufacturing techniques, they may be ideal candidates for laser cooling in the near future, since the electronic structures could be engineered to optimize cooling efficiency for specific applications. Equally important to the experimental investigations is the development of a theory that can provide a criterion for the material selection. Although this is very challenging considering the complexity of the electron-phonon coupling, useful results are expected to be obtained in the near future, which can then provide guidance for searching new materials and structures.

1.8 Statement of objective and scope of thesis

The major objective of this work is to develop an understanding of the atomic level mechanisms of laser cooling of solids, and based on this understanding, to enhance the cooling performance through quantum size effects of nanostructures. The thesis is organized in the following way.

In Chapter 2, the thermodynamics is analyzed for laser cooling of solids, an energy conversion process. Using the general theory of radiation entropy, the important roles of the optical frequency and the photon distribution function in determining the radiation entropy are identified. The usefulness of a narrowband approximation is established for a wide range of radiant sources. This approximation is then applied to compare the entropies of different light sources, including blackbody radiation, lasers, fluorescence, and the emerging class of random lasers. Using these results,

the Carnot efficiency for laser cooling of solids is determined, for emission fields with various entropy characteristics. This ideal efficiency indicates that there is room for enhancement, and this enhancement is likely to come from the enhanced off-resonance absorption.

Then in Chapter 3, this off-resonance absorption and the laser cooling power are analyzed using the Fermi golden rule. This treatment is inspired by recognizing that the absorption is a photon-induced, phonon-assisted, electron transition, and Fermi golden rule is the universal approach to determine the carrier interaction rates. This Fermi golden rule analysis shows that the laser cooling performance is indeed limited by absorption, and in turn by carrier couplings and populations. The carrier couplings include the photon-electron coupling and the electron-vibration coupling. The carrier populations include the ion concentration, the photon population, and the phonon density of states. These limiting factors will be treated in great detail in following chapters.

In Chapter 4, the photon-electron and electron-vibration coupling rates are calculated using ab initio methods. Using the calculated first-principle wavefunctions, the electric transition dipole moment between the ground and excited states is determined by its definition. The electron-phonon coupling is calculated by taking into account the modification of the electronic wavefunction in response to the nuclei motion, and the modifications of the vibrational modes before and after the transition. This ab initio approach provides a theoretical foundation for the optimal selection of laser cooling materials (both dopant and host).

Chapter 5 begins to optimize the photon population, using the unique transport

property of light in random nanopowders. The electromagnetic field distribution in a random multilayer is calculated by solving the Maxwell equations. Field enhancement and photon localization are predicted, which lead to more trapped photons in the medium and enhanced absorption.

Chapter 6 continues with the phonon population optimization. The phonon density of states of nanoparticles is calculated as a function of size, and compared to that of the bulk material. The difference is interpreted by decomposing the density to surface modes and internal modes of a particle. The phonon density is found to be enhanced in the desired range for nanopowders, compared to the bulk material.

Chapter 7 optimizes the population of the last carrier: electron (or dopant ion). Using the energy transfer theory, the relation between the dopant concentration and the quantum efficiency is established, giving the optimum dopant concentration. This mechanism is predicted to enhance the laser cooling power.

In Chapter 8, a thermal modelling predicts that the nanopowder system can be cooled to the cryogenic temperature range for the first time, due to the above enhancement mechanisms. Then the important results of the work presented are summarized, and future directions to extend the current work are suggested.

Chapter 2

Entropy and efficiency in laser cooling of solids

2.1 Introduction

As formulated by Boltzmann [52], thermodynamic entropy is determined by simply counting the number of available states associated with specified degrees of freedom of a system. However it is closely related to numerous other properties of systems such as information content [53, 54], temperature, and perhaps even the structure of matter and spacetime itself [55], because the states in question can be any of a multitude of internal or external degrees of freedom of the objects of which the system is composed. Entropy analyses can therefore place stringent limits on physical processes that alter the state of matter, provided the system is not displaced too far from thermodynamic equilibrium. For example, it can describe the evolution of the kinetic temperature during slow heating or cooling. In this paper, entropy calculations are

used to calculate the effects of various light sources and re-emission processes on the cooling of condensed matter by radiation in order to assess their comparative efficacy, by explicitly accounting for entropy content of the radiation fields. Just as for laser cooling of gases [56], spontaneous emission is shown to be important in mediating the irreversibility needed for laser cooling of solids using very general arguments.

The concept of optical refrigeration dates back to 1929, when Pringsheim recognized that thermal energy associated with the translational degrees of freedom of isolated atoms could be reduced by the process of anti-Stokes fluorescence [13]. In this process, an absorbed photon with a wavelength that is red-detuned with respect to an atomic resonance leads to re-emission at a higher mean energy (at the resonance wavelength), as shown in Fig. 2.1. As a result, the system loses an amount of energy equal to the frequency detuning multiplied by Planck's constant, every time a quantum is absorbed and the atom emits a photon. In gases it is important that this mechanism is consistent with a net loss of momentum because on average atoms moving toward the source present a higher probability for light absorption and are slowed by momentum transfer during the interaction. The average energy in a single translational degree of freedom is thereby reduced. One may refer to this as a reduced, one-dimensional kinetic temperature defined by $\frac{1}{2}k_{\mathrm{B}}T = \langle E_k \rangle$, although the velocity distribution is not likely to be Maxwellian in the presence of light, and the one-dimensional distribution might readily be different from the three-dimensional distribution that defines the equilibrium temperature [56]. In solids, although free translational motion of atoms does not take place, anti-Stokes fluorescence is also known to occur [1].

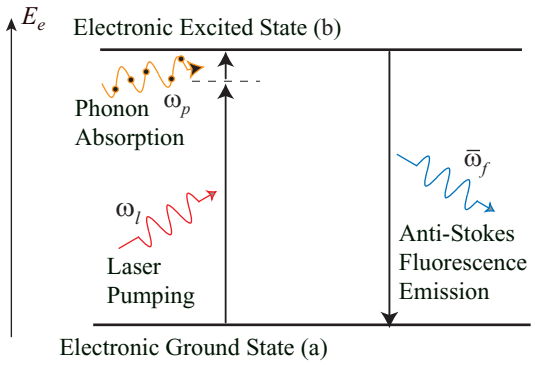

Figure 2.1: The principle of laser cooling in rare-earth ion doped crystal. The electron is excited by absorbing a laser pumping photon and one or more lattice phonons, and then decays by emitting a higher energy fluorescence photon.

Historically, it was believed at first that optical cooling by anti-Stokes fluorescence contradicted the second law of thermodynamics. Predictions suggested that the cycle of excitation and fluorescence was reversible, but that optical cooling would require the transformation of heat into work [14, 15]. This issue was cleared up by Landau, who pointed out that entropy had to be assigned to the radiation field [16] for a consistent description. Entropy of the radiation field was shown to be proportional to the frequency bandwidth and also to the solid angle of the propagating light. Typically, lasers have very small bandwidths and are highly directional, so their entropy is low. On the other hand, spontaneous fluorescence tends to be broadband and is emitted in all directions. Consequently its entropy is comparatively high. A consistent description of optical cooling must include the entropy of the incident and outgoing radiation fields.

2.2 Radiation entropy

The total power P of a steady, unpolarized beam of light (not necessarily collimated) crossing a surface A, that lies in the $x-y$ plane perpendicular to the direction z of propagation is given by the integral of the spectral radiance K_ω over frequency and solid angle [57]. That is,

$$P = \int_A \int_\Omega \int_\omega K_\omega d\omega \cos\theta d\Omega dA, \tag{2.1}$$

where ω is the optical frequency, Ω is the solid angle and θ is the polar angle between the surface normal and the z axis. The spectral radiance K_ω, which is the energy per unit time, area, angular frequency, and solid angle, is related to the light source characteristics by

$$K_\omega = (\hbar\omega)c\frac{D(\omega)f}{4\pi} = \frac{\hbar f\omega^3}{4\pi^3c^2}. \tag{2.2}$$

Here c is the speed of light in vacuum, $D(\omega)$ is the photon density of states given by $D(\omega) = \omega^2/(\pi^2c^3)$ [58], and f is the photon distribution function. The spectral radiance K_ω can be determined in practice with a spectrally dispersed measurement of the absolute intensity of the source, and then the photon distribution function f can be determined by inverting Eq. (2.2). The function f, which specifies how the radiant energy is distributed among available modes and frequencies, is the key quantity characterizing the nature of a light source in this paper.

In terms of f, the beam power can be written as

$$P = \frac{\hbar}{4\pi^3c^2} \int_A \int_\Omega \int_\omega f\omega^3 d\omega \cos\theta d\Omega dA. \tag{2.3}$$

Finding the entropy flow rate of a light beam is not as straightforward as deter-

mining power P, since the gas of photons is not necessarily in equilibrium. Landau [16] was the first to assign entropy to radiation fields by applying the Bose statistics to a "photon gas". A detailed derivation of entropy for light has been given in references [59, 60, 57].

We introduce the probability $P(N_1, N_2, ..., N_m)$ of finding N_1 photons in optical mode 1, N_2 photons in mode 2, ..., and N_m photons in mode m ($m \geq 1$). Then the entropy of the photons is given by [59]

$$S = -k_{\mathrm{B}} \sum_{N_1} \sum_{N_2} ... \sum_{N_m} P(N_1, N_2, ..., N_m) \ln P(N_1, N_2, ..., N_m), \tag{2.4}$$

where k_{B} is the Boltzmann constant. Denoting the probability of finding N_j photons in mode j ($j = 1, 2, ..., m$) by $p_j(N_j)$, and noting that $p_j(N_j)$ is independent of the occupation of other modes, the probability becomes

$$P(N_1, N_2, ..., N_m) = p_1(N_1) p_2(N_2) ... p_m(N_m), \tag{2.5}$$

where normalization requires

$$\sum_{N_j=1}^{\infty} p_j(N_j) = 1, \tag{2.6}$$

for each mode j. Substituting Eq. (2.5) into (2.4), and using (2.6), one finds

$$S = -k_{\mathrm{B}} \sum_{j=1}^{m} \sum_{N_j=0}^{\infty} p_j(N_j) \ln p_j(N_j) = \sum_{j=1}^{m} S_j, \tag{2.7}$$

where the partial entropy for one mode j is

$$S_j = -k_{\mathrm{B}} \sum_{N_j=0}^{\infty} p_j(N_j) \ln p_j(N_j). \tag{2.8}$$

These equations indicate that the total entropy of a multi-mode field can be decomposed into entropies for each mode.

Next assume that the probability of finding one additional photon in any state is independent of the number already occupying that state. Thus $p_j(N_j) \propto q_j^{N_j}$, where q_j is a number between 0 and 1 for all light sources. For example, $q_j = \exp(-\hbar\omega_j/k_{\mathrm{B}}T)$ for blackbody emission [58]. The normalization requirement Eq. (2.6) gives

$$p_j(N_j) = q_j^{N_j} / \sum_{l=0}^{\infty} q_j^l = (1-q_j)q_j^{N_j}, \ (0 \le q_j \le 1). \tag{2.9}$$

The distribution function f_j of state j, which gives the weighted occupation of the mode, can therefore be written as

$$f_j = \sum_{N_j=0}^{\infty} N_j p_j(N_j) = \sum_{N_j=0}^{\infty} N_j(1-q_j)q_j^{N_j} = \frac{q_j}{1-q_j}, \tag{2.10}$$

Substituting Eqs. (2.9) and (2.10) into (2.7), the entropy of the photons can be written in terms of f_j as

$$S = k_{\mathrm{B}} \sum_{j=1}^{m} [(1+f_j)\ln(1+f_j) - f_j \ln f_j], \tag{2.11}$$

and the entropy for the mode j becomes

$$S_j = k[(1+f_j)\ln(1+f_j) - f_j \ln f_j]. \tag{2.12}$$

In much the same way that we have defined the spectral energy radiance K_ω, a spectral entropy radiance L_ω (the entropy per unit time, area, angular frequency, and solid angle) can also be defined as

$$L_\omega = S_j c \frac{D(\omega)}{4\pi} = \frac{k_{\mathrm{B}}[(1+f)\ln((1+f)) - f\ln f]\omega^2}{4\pi^3 c^2}. \tag{2.13}$$

In terms of this quantity, the entropy flow rate $\dot{S}$ of a light beam can finally be written as

$$\dot{S} \ = \ \int_A \int_\Omega \int_\omega L_\omega d\omega \cos\theta d\Omega dA$$

$$= \frac{k_B}{4\pi^3 c^2} \int_A \int_\Omega \int_\omega [(1+f)\ln(1+f) - f\ln f]\omega^2 d\omega \cos\theta d\Omega dA. \quad (2.14)$$

The quantity $\dot{S}$ is suitable for characterizing the degree of disorder of a light beam. However, it is an extensive variable rather than an intensive variable. For example, if we just double the surface area of a blackbody, the entropy of its radiation is also doubled, although the radiation is essentially still of the same class. On the other hand, a high-power diode laser beam might contain the same amount of entropy as a very low-power blackbody radiation, although the nature of the radiation is very different. Hence, the amount of entropy is always dependent on the beam power, and can not be used meaningfully on its own to distinguish or characterize various radiation fields. A more suitable parameter for this purpose is the entropy flow rate per unit power:

$$\frac{\dot{S}}{P} = \frac{k_B}{\hbar} \frac{\int_A \int_\Omega \int_\omega [(1+f)\ln((1+f)) - f\ln f]\omega^2 d\omega \cos\theta d\Omega dA}{\int_A \int_\Omega \int_\omega f\omega^3 d\omega \cos\theta d\Omega dA}. \quad (2.15)$$

Here $\dot{S}/P$ has units of inverse temperature (K^{-1}), and the reciprocal of this quantity is often referred to as the "flux temperature" of the beam in the literature [59, 57]. This is adopted from the definition of temperature in a conventional thermodynamic system, given by

$$\frac{1}{T} = \left.\frac{\partial S}{\partial E}\right|_V, \quad (2.16)$$

where S is entropy, E is the internal energy, and V is the volume.

The entropy flow rate per unit power $\dot{S}/P$ covers many orders of magnitude for different radiation fields, and in the present paper represents the beam "quality". Hence, as will be seen in Section 2.5, $\dot{S}/P$ rather than $\dot{S}$ is an essential parameter in calculating the Carnot efficiency for laser cooling.

2.3 Roles of angular frequency and distribution function in radiation entropy

Equation (2.15) completely describes the roles of distribution function, area, frequency, and solid angle in the entropy flow rate per unit power. However, for non-thermal (non-equilibrium) radiation with arbitrary distribution functions the calculation of $\dot{S}/P$ is laborious. Consequently we proceed below to examine a useful approximation for the radiance based on an assumption that the radiation can be treated as "narrowband".

Introducing a central frequency ω_0, frequency bandwidth $\Delta\omega$, and divergence angle δ of the beam, we rewrite the power in a form that is more convenient for analysis. If the radiation is narrowband, and isotropic within the circular cone of half-angle δ, the power of the beam can be approximated as

$$P = \int_A \int_\Omega \int_{\Delta\omega} K_\omega \cos\theta d\omega d\Omega dA = \bar{K}_\omega A \Delta\omega \pi \sin^2\delta, \tag{2.17}$$

where $\bar{K}_\omega$ is the mean radiance over the frequency bandwidth and beam solid angle. Note that in the original spectrum the frequency runs over the interval 0 to ∞, while here, we only consider the range $\Delta\omega$ given by the full width at half-maximum (FWHM). This assumes that the energy and entropy outside this range can be neglected.

According to Eq. (2.2), an estimated or average distribution function $\bar{f}$ can be defined that is related to the average radiance $\bar{K}_\omega$ through

$$\bar{K}_\omega = \frac{\hbar \bar{f} \omega_0^3}{4\pi^3 c^2}. \tag{2.18}$$

Note that in this expression the variable ω has been replaced with the central frequency ω_0 in the optical spectrum. In the same way that f can be calculated from K_ω using Eq. (2.2), the average distribution function $\bar{f}$ can readily be calculated from the mean radiance $\bar{K}_\omega$ using 2.18.

The entropy flow rate is then approximated in a similar fashion,

$$\dot{S} = \frac{k_B}{4\pi^3 c^2}[(1+\bar{f})\ln((1+\bar{f})) - \bar{f}\ln\bar{f}]\omega_0^2 A\Delta\omega\pi\sin^2\delta, \tag{2.19}$$

Hence the entropy flow rate per unit power reduces to

$$\frac{\dot{S}}{P} = \frac{k_B}{\hbar\omega_0}\frac{(1+\bar{f})\ln((1+\bar{f})) - \bar{f}\ln\bar{f}}{\bar{f}}. \tag{2.20}$$

This expression, while being limited to narrowband radiation, is much simpler than the general relation in Eq. (2.15). It has the merit of showing that for narrowband sources the entropy flow rate per unit power is inversely proportional to the central frequency ω_0, and is decreasing with an increasing average distribution function $\bar{f}$.

To investigate the applicability of the narrowband approximation, we now compare results based on Eq. (2.20) with exact results based on Eq. (2.15). Narrowband radiation is considered for which the spectral radiance is described by a Gaussian distribution

$$K_\omega = K_0 \exp\left[-\left(\frac{\omega-\omega_0}{\sqrt{\ln 2}\Delta\omega}\right)^2\right]. \tag{2.21}$$

Here K_0 is the spectral radiance at the central frequency ω_0 of the source, and $\Delta\omega$ is the spectral width. Representative values for optical sources are $K_0 = 60$ W/m^2-(rad/s)-sr, $\omega_0 = 1.8850 \times 10^{15}$ rad/s (or the central wavelength $\lambda_0 = 1$ μm), and $\Delta\omega = 2.5133 \times 10^{11}$ rad/s (or $\Delta\lambda = 0.133$ nm). The corresponding spectral radiance

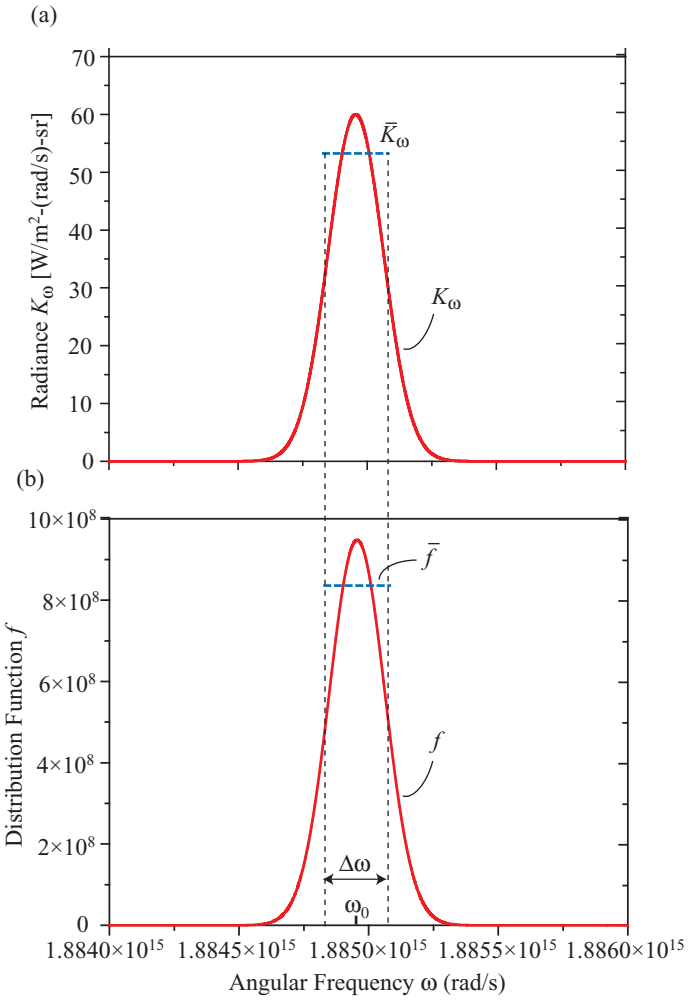

Figure 2.2: (a) The spectral radiance K_ω (solid curve) and the average radiance $\bar{K}_\omega$ (dashed curve), (b) The spectral distribution function f (solid curve) and the average distribution function $\bar{f}$ (dashed curve). The central frequency is $\omega_0 = 1.8850 \times 10^{15}$ rad/s, and the bandwidth $\Delta\omega = 2.5133 \times 10^{11}$ rad/s.

K_ω and distribution function f are shown in Figs. 2.2(a) and (b) respectively. The exact entropy flow rate per unit power, calculated using Eq. (2.15), is 5.59×10^{-12} K^{-1}. To use the narrowband approximation, the average radiance is first calculated using

$$\bar{K}_\omega = \frac{\int_{\Delta\omega} K_\omega d\omega}{\Delta\omega}, \tag{2.22}$$

and then the average distribution function is derived from it using

$$\bar{f} = \frac{4\pi^3 c^2 \bar{K}_\omega}{\hbar\omega_0^3}. \tag{2.23}$$

The results of the narrowband approximation are given by the dashed curves in Figs. 2.2(a) and (b). The approximate entropy flow rate per unit power calculated using Eq. (2.20) is found to be 1.79×10^{-12} K^{-1}. Although this value is about one third of the exact value, it is nevertheless a sufficiently good approximation for this highly-ordered light source in a thermodynamic sense, considering that both the exact and approximate values are negligibly small.

To further check the validity of the narrowband approximation for a variety of Gaussian sources, we calculated the exact and approximate entropy flow rate per unit power $\dot{S}/P$ over a wide range of values of K_0, ω_0, and $\Delta\omega$. Interestingly, $\dot{S}/P$ is not a function of the bandwidth $\Delta\omega$, since $\Delta\omega$ does not affect the mean distribution function $\bar{f}$, for a given K_0 and ω_0. Hence, $\dot{S}/P$ is plotted only as a function of K_0 and ω_0 in Fig. 2.3. In the figure, it is evident that the approximate results agree very well with the exact results in the low radiance region. This is because, for low radiance $\dot{S}/P$ is a weak function of K_0, while for high radiance, it decreases strongly as a function of K_0. Hence the approximate approach agrees best with exact calculations

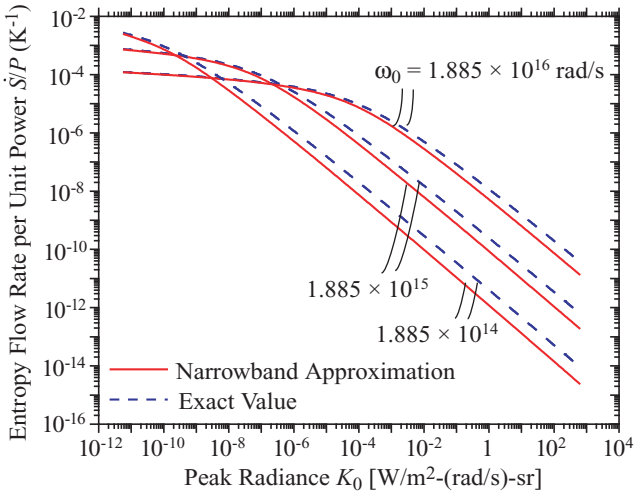

Figure 2.3: Entropy flow rate per unit power as a function of the peak radiance K_0, for a few central frequency ω_0. The narrowband approximation and exact results are shown, indicating convergence at low K_0.

at low radiance.

The narrowband approximation also works surprisingly well for some sources of broadband radiation. We show this by considering an additional case of the blackbody spectral radiance, which is

$$K_\omega^{\mathrm{o}} = \frac{\hbar}{4\pi^3 c^2} f^{\mathrm{o}} \omega^3, \tag{2.24}$$

with f^{o} being given by the equilibrium distribution function

$$f^{\mathrm{o}} = \frac{1}{e^{\hbar\omega/k_{\mathrm{B}}T_b} - 1}, \tag{2.25}$$

This is the usual Bose-Einstein distribution, and T_b is the temperature of the cavity which emits the blackbody radiation.

Blackbody emission is a special case for which an exact analytical expression for $\dot{S}/P$ can be obtained. As this form of radiation field is uniformly directed in space,

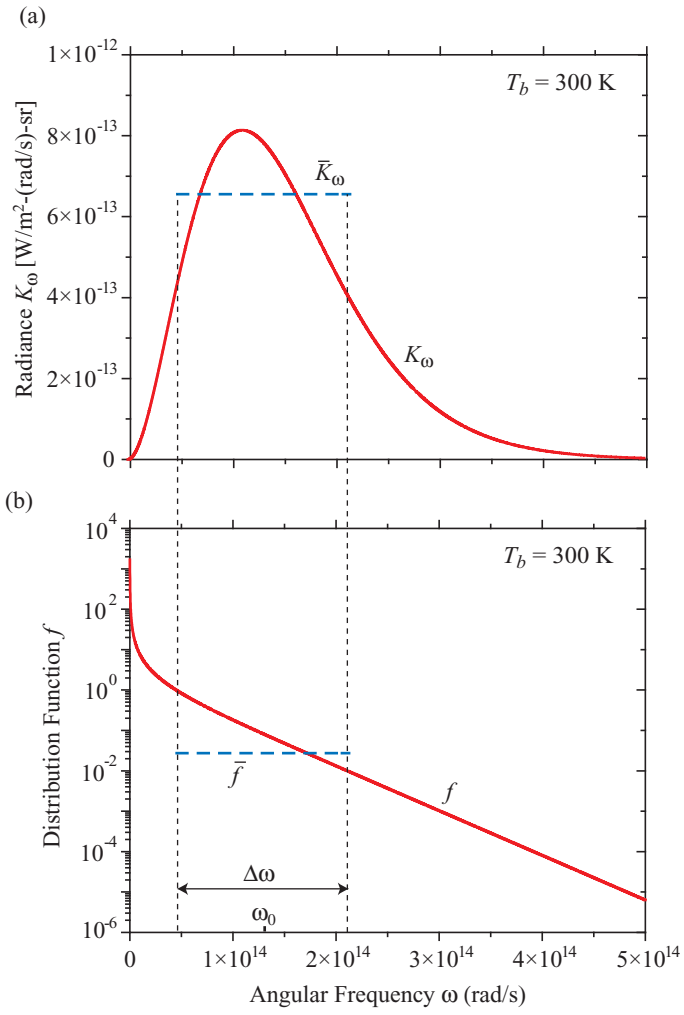

[t]

Figure 2.4: Variations of the radiance and distribution function, with respect to the angular frequency for blackbody emission at $T_b = 300$ K. The mean quantities are also shown.

its power P is given by Eq. (2.1), i.e.,

$$P = A\pi \frac{\hbar}{4\pi^3 c^2} \int_0^\infty f^{\mathrm{o}} \omega^3 d\omega = \sigma_{\mathrm{SB}} A T_b^4, \tag{2.26}$$

where σ_{SB} is the Stefan-Boltzmann constant. The corresponding entropy flow rate is

$$\dot{S} = A\pi \frac{k_{\mathrm{B}}}{4\pi^3 c^2} \int_0^\infty [(1+f^{\mathrm{o}}) \ln((1+f^{\mathrm{o}})) - f^{\mathrm{o}} \ln f^{\mathrm{o}}] d\omega = \frac{4}{3} \sigma_{\mathrm{SB}} A T_b^3, \tag{2.27}$$

with the result that the entropy flow rate per unit power is

$$\frac{\dot{S}}{P} = \frac{4}{3T_b}. \tag{2.28}$$

As a numerical example, consider blackbody emission from a cavity at room temperature $T_b = 300$ K. The spectral radiance and distribution function are shown in Fig. 2.4(a) and (b) respectively. The exact value of $\dot{S}/P$, calculated using Eq. (2.28), is $\dot{S}/P = 4.44 \times 10^{-3}$ K^{-1}, while the approximate value calculated using Eq. (2.20) is 4.51×10^{-3} K^{-1}. The difference is less than 2% and the approximation is therefore well justified in this case.

To further check the validity of this approximation for blackbody sources at a variety of temperatures of interest in this paper, we calculated the exact and approximate values of $\dot{S}/P$ as a function of temperature. The results are plotted in Fig. 2.5. Interestingly, over the entire range the approximation is in excellent agreement with the exact approach. This seems to be surprising since blackbody radiation is broadband, but in this temperature range the blackbody source has very low radiance, so there is little sensitivity to any small error in $\bar{f}$ introduced by the averaging process.

The reason the narrowband approximation works better than expected can be understood from another perspective. In this procedure we first truncate the original

[t]

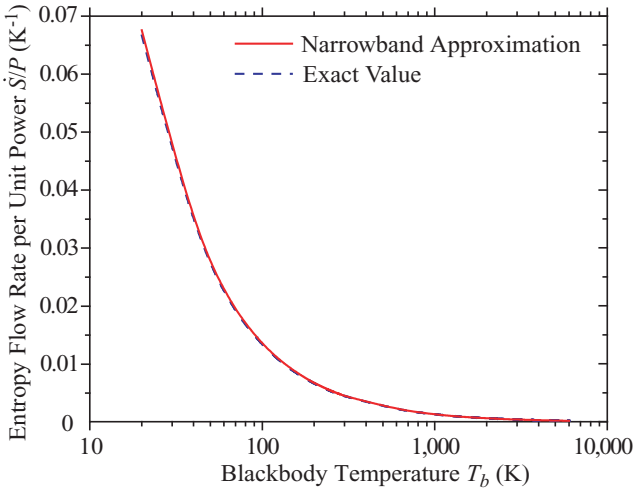

Figure 2.5: Entropy flow rate per unit power, for blackbody radiation, as a function temperature. The narrowband approximation and the exact results are shown.

spectrum and consider a restricted range of frequency $\Delta\omega$. This makes the approximated spectra narrower than the original ones, and *decreases* the degree of disorder. Second, this $\Delta\omega$ range of the original spectra is averaged to get the mean spectra, with the result that the average radiance becomes uniformly distributed at a lower value than the peak in the original spectra. Because $\dot{S}/P$ depends essentially inversely on f, the degree of disorder is artificially *increased* by this procedure. As a result, whether the approximate value of $\dot{S}/P$ is found to be higher or lower than the exact value is determined by how well these two steps compensate each other. Overall, our finding is that this narrowband approximation works particularly well for light sources of low radiance, for which $\dot{S}/P$ is a weak function of the mean distribution function.

2.4 Entropy of different light sources

A comparison of light sources with a wide variety of entropic characteristics is relevant for the evaluation of laser cooling of solids. Some sources are spectrally broadband and isotropic in space, such as blackbody sources. Some are spectrally narrowband and directional in space, such as lasers. These cases are sketched in Fig. 2.6. To calculate the corresponding $\dot{S}/P$ we only need to know the central frequency ω_0 and the average distribution function $\bar{f}$ for each type of source. The latter can be calculated if the average spectral radiance is known, and this is facilitated by relating $\bar{K}_\omega$ to more convenient, measurable parameters. Based on Eqs. (2.17) and (2.18), the average distribution function $\bar{f}$ can be rewritten in terms of power P, bandwidth $\Delta\omega$, beam angle δ and centreal frequency ω_0, as

$$\bar{f} = \bar{K}_\omega \frac{4\pi^3 c^2}{\hbar\omega_0^3} = \frac{P}{A\Delta\omega\pi\sin^2\delta}\frac{4\pi^3 c^2}{\hbar\omega_0^3}. \tag{2.29}$$

Numerical examples for four classes of radiation fields are presented below, and the associated parameters are listed in Table 2.1.

Blackbody emission has a high degree of disorder, since it is equilibrium emission from all possible electronic levels, and includes both spontaneous and stimulated emission fields. The average spectral radiance and the distribution function is determined by temperature alone. For a blackbody at $T_b = 4,395$ K, the average distribution function is $\bar{f} = 0.0324$, and the entropy flow rate per unit power is $(\dot{S}/P)_b = 3.078 \times 10^{-4}$ K^{-1}. This is comparable to the entropy of thermal energy at this temperature, and in this sense blackbody radiation is considered as "pure heat" or "low-grade" radiation energy [57].

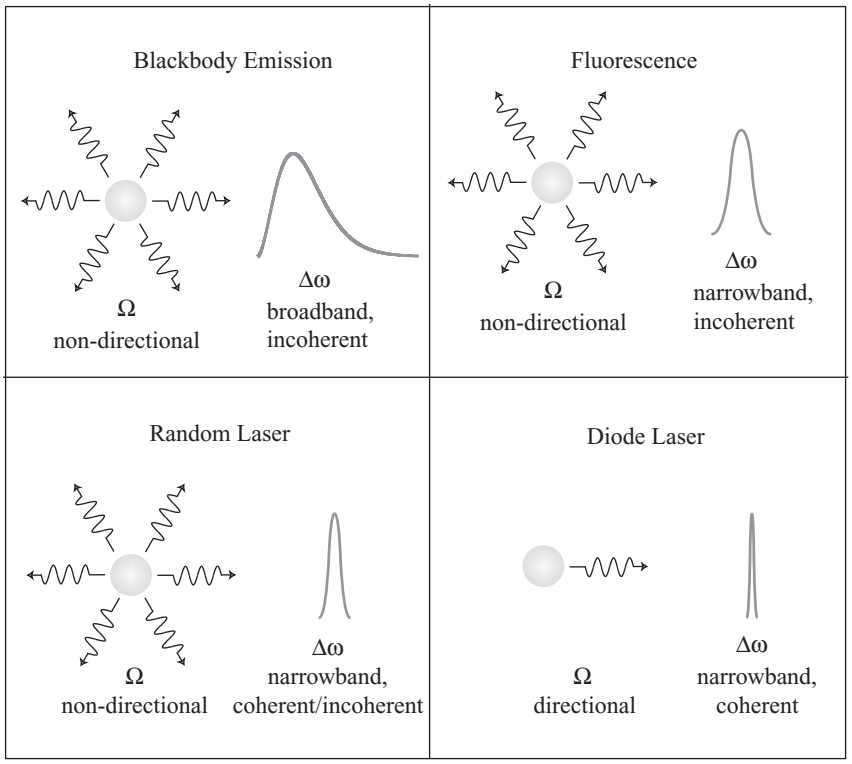

Figure 2.6: Schematics of the emission bandwidth and solid angle associated with four different emission sources.

Table 2.1: Beam parameters and entropy flow rates per unit power, for typical light sources

	Blackbody Emission ($T_b = 4,395$ K)	Fluorescence	Random Laser	Diode Laser
Beam Power P, W	80.05	0.06	0.06	0.06
Central Wavelength λ_0, nm	999.3	999.3	999.3	999.3
Wavelength Bandwidth $\Delta\lambda$, nm	2,223	35	1	0.1331
Central Frequency ω_0, rad/s	1.887×10^{15}	1.887×10^{15}	1.887×10^{15}	1.887×10^{15}
Frequency Bandwidth $\Delta\omega$, rad/s	2.448×10^{15}	5.666×10^{13}	1.888×10^{12}	2.513×10^{11}
Beam Area A, m^2	3.784×10^{-6}	3.784×10^{-6}	3.784×10^{-6}	7.854×10^{-9}
Beam Divergence δ, rad	$\pi/2$	$\pi/2$	$\pi/2$	0.001
Average Radiance $\bar{K}_\omega$, W/m^2-(rad/s)-sr	2.071×10^{-9}	8.908×10^{-11}	2.672×10^{-9}	9.6763
Average Distribution Function $\bar{f}$,	0.0324	1.404×10^{-3}	0.0421	1.525×10^{8}
Entropy Flow Rate per Unit Power $\dot{S}/P$, K^{-1}	3.078×10^{-4}	5.362×10^{-4}	2.906×10^{-4}	9.030×10^{-12}

In laser cooling of solids, the radiant output of the system is typically chosen to be fluorescence. Fluorescence is spatially isotropic spontaneous emission that is usually spectrally narrowband. Using values relevant to laser cooling of Yb^{3+}:ZBLANP from earlier experiments [2], where the central frequency and the bandwidth are $\omega_0 = 2\pi c/\lambda_0 = 1.886 \times 10^{15}$ rad/s (as $\lambda_0 = 999.3$ nm) and $\Delta\omega = 2\pi c \Delta\lambda/\lambda_0^2 = 5.662 \times 10^{13}$ rad/s (as $\Delta\lambda = 35$ nm) respectively, the cooling power of the system was estimated to be approximately 0.9 mW, and the corresponding fluorescence power P was 60 mW [2]. Assuming the fluorescence is emitted homogeneously and hemi-spherically out of the surface of the sample, the beam divergence is then $\delta = \pi/2$. The sample in Ref. [2] was a cylinder with diameter 170 μm and length 7 mm, giving the surface area $A = 3.784 \times 10^{-6}$ m^2. Hence the average distribution function $\bar{f}$ was

$$\bar{f} = \frac{P}{A\pi \sin^2 \delta \Delta\omega} \frac{4\pi^3 c^2}{\hbar \omega_0^3} = 1.404 \times 10^{-3}. \tag{2.30}$$

This determines the entropy flow rate per unit power to be $(\dot{S}/P)_f = 5.36 \times 10^{-4}$ K^{-1}.

In powder laser samples pumped with high intensity, random laser output with the same energy can be achieved. Emission may be considered to be homogeneous into the half space above the emitting surface. Assuming a bandwidth of $\Delta\lambda = 1$ nm [61, 62], which is much narrower than that of the fluorescence, one finds $\bar{f} = 0.0421$, and $(\dot{S}/P)_{rl} = 2.906 \times 10^{-4}$ K^{-1}.

If the output radiation field were to be in the form of a diode laser, again operating at 60 mW with a central wavelength of 999.3 nm, but with a typical beam size of 100 μm at the source, a bandwidth of 40 GHz and a divergence of $\delta = 1$ mrad, one would

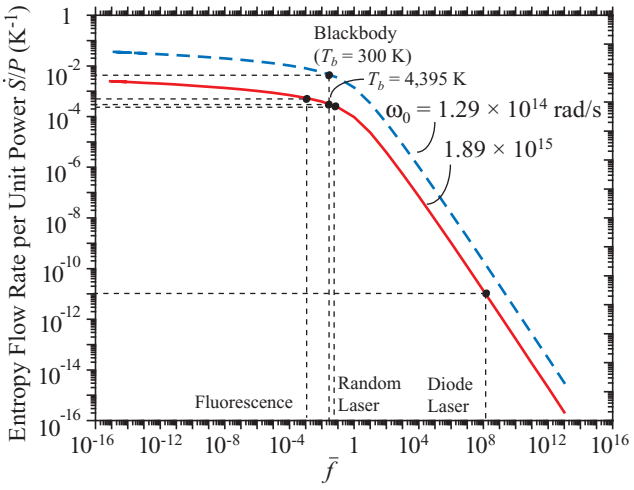

Figure 2.7: Variation of the entropy flow rate per unit volume as a function of the average distribution function $\bar{f}$ and central frequency ω_0, which characterizes different light sources.

find $\bar{f} = 1.525 \times 10^8$ and $(\dot{S}/P)_{dl} = 9.03 \times 10^{-12}$ K^{-1}.

These results for the entropy flow rate per unit power for various light sources are compared in Fig. 2.7. It is evident from the figure that $\dot{S}/P$ decreases rapidly with decreasing beam bandwidth and divergence. If either the bandwidth $\Delta\omega$ or the divergence δ of the source drops to nearly zero, then we see from Eq. (2.19) that $\dot{S}/P$ becomes

$$\dot{S} \simeq \lim_{f\to\infty} \frac{k_B A}{4\pi^2 c^2}[(1+\bar{f})\ln\bar{f} - \bar{f}\ln\bar{f}]\omega_0^2 \Delta\omega \sin^2\delta = 0. \tag{2.31}$$

Hence the limiting case of monochromatic or unidirectional radiation (which is highly ordered) constitutes a source that carries essentially no entropy.

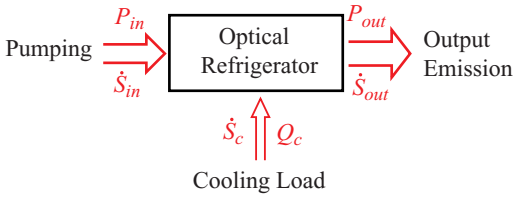

Figure 2.8: A control volume showing various input and output processes that control the energy balance during laser cooling of a solid.

2.5 Carnot cooling efficiency versus emission entropy

Now consider a control volume that is to be cooled radiatively. This volume is labelled "optical refrigerator" in Figure 2.8. The power flow in and out of this region reflects the balance of the pump laser, the external thermal load, and the fluorescence emission.

According to the first law of thermodynamics, we have

$$P_{out} = P_{in} + Q_c. \tag{2.32}$$

The cooling efficiency is defined in the customary way for a refrigerator [33], namely

$$\eta = \frac{Q_c}{P_{in}}. \tag{2.33}$$

The maximum value of η is the Carnot limit η_C determined by the second law of thermodynamics. The entropy carried by the fluorescence cannot be less than the sum of the entropy withdrawn from the cooling sample and the entropy transported in by the pump laser. That is,

$$\dot{S}_{out} \geq \dot{S}_{in} + \dot{S}_c, \tag{2.34}$$

where $\dot{S}_{in}$, $\dot{S}_{out}$ and $\dot{S}_c$ are the entropy flow rates for the absorbed irradiation, the output emission, and the thermal load. This equation can also be written as

$$P_{out}\left(\frac{\dot{S}}{P}\right)_{out} \geq P_{in}\left(\frac{\dot{S}}{P}\right)_{in} + \frac{Q_c}{T}, \tag{2.35}$$

where T is the temperature of the thermal load. The reversible Carnot limit is obtained by choosing the equality sign in Eq. (2.35). By substituting Eqs. (2.32) and (2.33) into Eq. (2.35) to eliminate P_{in}, P_{out} and Q_c, we find the Carnot efficiency to be

$$\eta_{\mathrm{C}} = \frac{\left[(\dot{S}/P)_{out} - (\dot{S}/P)_{in}\right]T}{1 - (\dot{S}/P)_{out}T}. \tag{2.36}$$

Thus the cooling power and the total output power are

$$Q_c = \eta_{\mathrm{C}} P_{in}, \tag{2.37}$$

and

$$P_{out} = (1 + \eta_{\mathrm{C}})P_{in}. \tag{2.38}$$

Equation (2.36) indicates that small $(\dot{S}/P)_{in}$ and large $(\dot{S}/P)_{out}$ are desirable to enhance η_{C}, and that it is important to control the characteristics of both the input and output fields. A pumping source with the smallest possible $(\dot{S}/P)_{in}$, corresponding to a monochromatic, unidirectional, single-mode laser, is desired since $(\dot{S}/P)_{in} = 0$. The emitted field could be in the form of fluorescence, random laser emission, or monomode laser quality emission, via appropriate selections of pumping level, sample, and feedback structures. It is therefore useful to know how the cooling efficiency can be influenced by controlling the radiation character of the emission

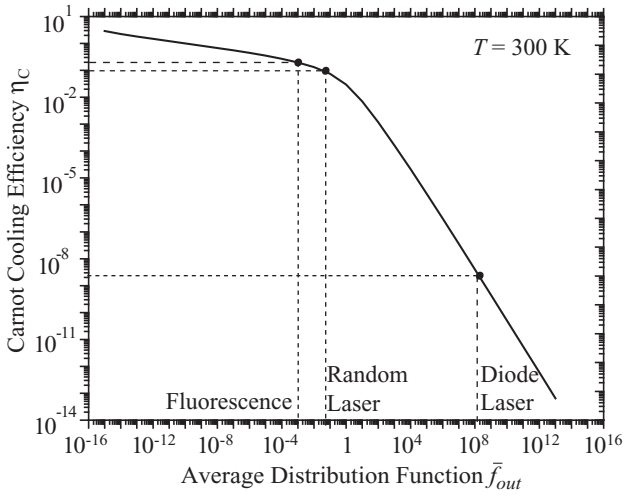

Figure 2.9: Variation of the Carnot efficiency with respect to the average distribution function for the output emission fields. Three typical emission fields are marked.

fields. Under the condition of single-mode laser pumping, Eq. (2.36) becomes

$$\eta_{\mathrm{C}} = \frac{(\dot{S}/P)_{out} T}{1 - (\dot{S}/P)_{out} T}. \tag{2.39}$$

Using Eq. (2.39), the Carnot efficiency can be calculated as a function of the entropy flow rate per unit power, or as a function of the average distribution function. The result is shown in Fig. 2.9. This figure indicates that fluorescent systems have the highest cooling efficiency. In the example of laser cooling of Yb^{3+}:ZBLANP discussed earlier [57], the entropy flow rate per unit power of the fluorescence emission was found to be $(\dot{S}/P)_{out} = 5.36 \times 10^{-4}$ K^{-1}. Correspondingly, the Carnot efficiency of this optical cooler is found to be about 20% at room temperature. If stimulated emission is employed in the system, the Carnot cooling efficiency is lower. One finds $\eta = 0.11$ for random laser emission and $\eta = 2.7 \times 10^{-9}$ for diode emission respectively. Fields of this nature are far less efficient than fluorescence emission.

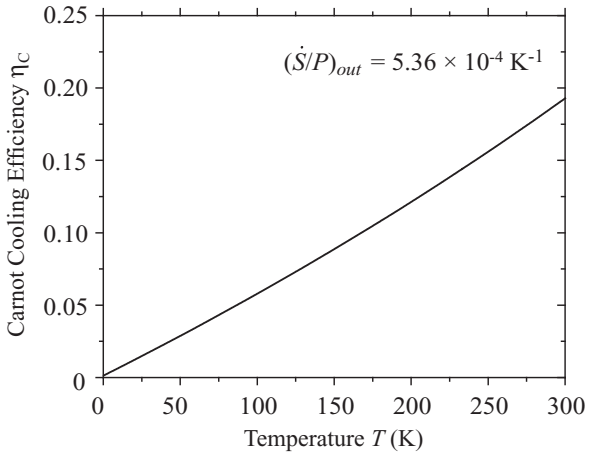

Figure 2.10: Optimum Carnot efficiency as a function of temperature.

Also using Eq. (2.39), the cooling efficiency as a function of temperature is shown in Fig. 2.10, for $(\dot{S}/P)_{out} = 5.36 \times 10^{-4}$ K^{-1}. It diminishes approximately linearly to zero as $T \to 0$.

2.6 Cooling efficiency for real systems including quantum efficiency

In real systems, the quantum efficiency is less than unity, and the energy loss during any internal relaxation process is irreversible, from a thermodynamic point of view. When considering such losses caused by nonradiative decay, it is helpful to account for the associated heat load explicitly by dividing the cooling load channel shown earlier in Fig. 2.8 into two parts. In Fig. 2.11 the cooling load channel is now considered to be the reversible part of the refrigerator cycle. No entropy is generated, and the cooling load is still given by Eq. (7.9). In the figure, the new heat generation

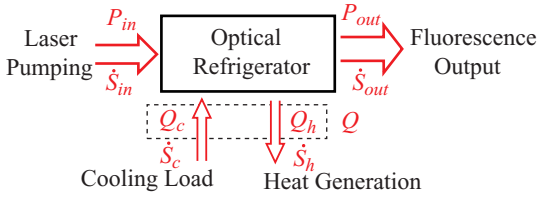

Figure 2.11: Designation of in and out powers and entropy flow rates. Laser pumping (in), fluorescence output (out), cooling (c), and heat generation (h).

channel corresponds to the irreversible losses from internal relaxation, and the entropy production for this channel, also for the entire cooling cycle, is

$$\Delta\dot{S} = \dot{S}_{out} + \dot{S}_h - \dot{S}_{in} - \dot{S}_c = \dot{S}_h - Q_h\left(\frac{\dot{S}}{P}\right)_{out} = Q_h\left[\frac{1}{T} - \left(\frac{\dot{S}}{P}\right)_{out}\right]. \quad (2.40)$$

Here, the irreversibility is considered to be introduced when part of the fluorescence output is turned into heat. The relations between the powers are

$$P_{out} + Q_h = P_{in} + Q_c \quad (2.41)$$

$$Q_c = \eta_C P_{in} \quad (2.42)$$

$$\frac{P_{out}}{P_{out} + Q_h} = \eta_q. \quad (2.43)$$

where η_q is the quantum efficiency. The net cooling power is then the difference between the cooling load and the heat generation, or

$$Q = Q_c - Q_h = P_{in}[\eta_C - (1 + \eta_C)(1 - \eta_q)], \quad (2.44)$$

and the cooling coefficient of performance is

$$\eta = \frac{Q}{P_{in}} = \eta_C - (1 + \eta_C)(1 - \eta_q). \quad (2.45)$$

Using Eq. (2.45) along with Eq. (2.36), the cooling coefficient may be plotted as a function of the quantum efficiency η_q, as shown in Fig. 2.12. The cooling coefficient

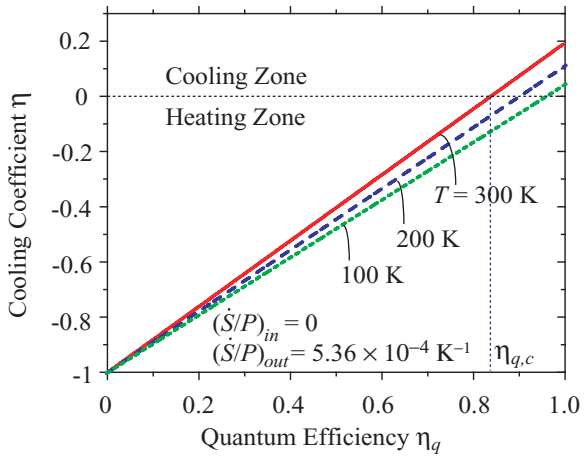

Figure 2.12: Cooling efficiency as a function of the quantum efficiency, for different temperatures.

has a linear relationship with the quantum efficiency. If the quantum efficiency is 1, the reversible cycle discussed in last section is recovered, and the cooling coefficient is the Carnot efficiency. In the other extreme, if the quantum efficiency is zero, the cooling coefficient becomes -1, indicating that all the laser pumping energy is turned into thermal energy and deposited into the cooling element. There exists a critical quantum efficiency $\eta_{q,c}$ below which the cooling effect is eliminated. For example, $\eta_{q,c}$ is 0.83 at room temperature, if the pumping is an ideal laser source and the fluorescence has an entropy flow rate per unit power of $\dot{S}/P = 5.36 \times 10^{-4}$ K^{-1}.

2.7 Discussions and summary

The above analysis indicates that the limiting efficiency of laser cooling of solids can be as high as 20%. However, the cooling efficiency achieved to date is only around 3% [34]. Hence a significant amount of irreversibility must be present in

the experiments. An existing strategy is to use a longer pumping wavelength to obtain higher cooling efficiency, but in practice the absorption coefficient drops more rapidly than the rise in efficiency beyond an optimum detuning. Also, trace impurity absorption eventually dominates over the desired Yb^{3+} absorption, causing heating. While the sample could be purified to suppress trace absorption, it seems that new methods would be more useful.

The results show that since current experiments already focus on the use of incident pump sources with zero entropy and spontaneous emission output, no improvements can be expected by resorting to other forms of output. For example monomode pumping together with random laser output is inherently less efficient than monomode pumping with spontaneous emission output, other things being equal. In the framework of fluorescence, one should explore ion-host combinations which can emit fluorescence with larger entropy flow rate per unit power. Higher quantum efficiency is essential, along with higher radiative decay rates (though the latter is only important close to saturation). In summary, improvements are most likely to come from enhanced quantum efficiency, enhanced absorption through manipulation of the electron-phonon interaction, improved emission rates, or from altogether new methods.

Next we will apply the Fermi golden rule to treat this off-resonance absorption, and to identify the limiting factors in the laser cooling process.

Chapter 3

Fermi golden rule theory for laser cooling of solids

3.1 Introduction

As pointed out in last chapter, laser cooling relies on tuning the pump wavelength longer than the mean emission wavelength while still retaining a significant amount of absorption. This off-resonance absorption is a photon-induced, phonon-assisted, electron transition. The absorption rate can be naturally treated with the Fermi golden rule, the universal approach to determine the interaction rates for various elastic and inelastic scattering processes among the same or different kinds of carriers. In this chapter the Fermi golden rule will be used as a primary theory to express the laser cooling power and to identify the limiting factors.

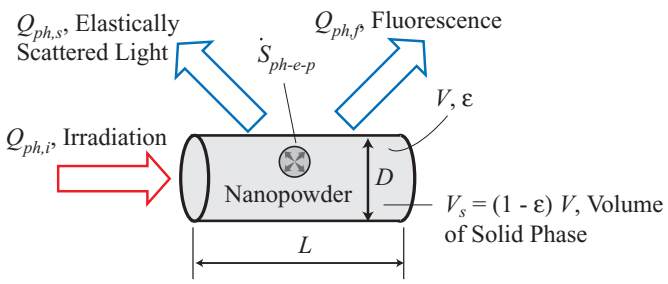

Figure 3.1: The energy diagram for the laser cooling of a nanopowder. The external thermal load is not shown.

3.2 Rate equation and cooling power

In Fig. 3.1, a steady state energy diagram is shown for the laser cooling of nanopowders. The energy entering the control volume is the laser irradiation power $Q_{ph,i}$, and those leaving the control volume are the elastically scattered power $Q_{ph,s}$ and the fluorescence emission power $Q_{ph,f}$. The net cooling power $\dot{S}_{ph\text{-}e\text{-}p}$ is given by $Q_{ph,i} - Q_{ph,s} - Q_{ph,f}$, and is balanced by some kind of external thermal load (for example, thermal radiation [2]), which is not shown in Fig. 3.1 since it is not the focus of this work. To minimize the fluorescence reabsorption, the sample is made into a very thin fiber-type geometry, as used by Gosnell in [2], where the length L is similar to 7 mm, and the diameter D is around 170 μm. The volume of the medium is V and the porosity is ε. The carrier interactions and energy conversions only take place in the volume of the solid phase, which is $V_s = (1-\varepsilon)V$. However, the presence of nano-pores are important in that they affect the photon transport and the phonon DOS, as will be seen in later sections.

In order to relate the absorbed and emitted power, the population dynamics of the ground and excited electronic states needs to be established. Although the rate

equation is not suitable for describing atoms with any correlations between them (such as in cooperative interactions or other interatomic couplings), it is correct to describe the population dynamics of statistically independent atoms. In the nanoparticles studied, cooperative effects are negligible [63]. Hence, the rate equation for the two-level system shown in Fig. 1.1(b) is

$$\frac{dn_b}{dt} = -\dot{\gamma}_{e,d} n_b + \dot{\gamma}_{e,a} n_a + (1-\eta_e)\dot{\gamma}_{e,r} n_b, \tag{3.1}$$

where n_b and n_a are the populations of the excited and ground states, respectively. Here, the intrinsic decay rate $\dot{\gamma}_{e,d}$ is the sum of the intrinsic radiative decay (includes the spontaneous and stimulated emissions) rate $\dot{\gamma}_{e,r}$ and the intrinsic nonradiative decay rate $\dot{\gamma}_{e,nr}$. The rate $\dot{\gamma}_{e,a}$ is the absorption (or excitation) rate. The last term in Eq. (3.1) accounts for the reabsorption effect, and η_e is the probability of a fluorescence photon to escape out of the medium without any reabsorption, or the so called escape efficiency [3]. The intrinsic quantum efficiency is defined as

$$\eta_{e-ph} = \frac{\dot{\gamma}_{e,r}}{\dot{\gamma}_{e,d}} = \frac{\dot{\gamma}_{e,r}}{\dot{\gamma}_{e,r} + \dot{\gamma}_{e,nr}}. \tag{3.2}$$

In Eq. (3.1), the reabsorption term can be combined into the decay term, and the rate equation becomes

$$\begin{aligned} \frac{dn_b}{dt} &= -[\dot{\gamma}_{e,r} + \dot{\gamma}_{e,nr} - (1-\eta_e)\dot{\gamma}_{e,r}] n_b + \dot{\gamma}_{e,a} n_a n_b \\ &= -(\eta_e \dot{\gamma}_{e,r} + \dot{\gamma}_{e,nr}) n_b + \dot{\gamma}_{e,a} n_a n_b. \end{aligned} \tag{3.3}$$

This implies that the original system with reabsorption can be equivalent to an effective system in which the reabsorption is absent, and the corresponding external

quantities for this effective system are

$$\tilde{\dot{\gamma}}_{e,r} = \eta_e \dot{\gamma}_{e,r} \tag{3.4}$$

$$\tilde{\dot{\gamma}}_{e,nr} = \dot{\gamma}_{e,nr} \tag{3.5}$$

$$\tilde{\dot{\gamma}}_{e,d} = \eta_e \dot{\gamma}_{e,r} + \dot{\gamma}_{e,nr} \tag{3.6}$$

$$\tilde{\eta}_{e-ph} = \frac{\eta_e \dot{\gamma}_{e,r}}{\eta_e \dot{\gamma}_{e,r} + \dot{\gamma}_{e,nr}} \tag{3.7}$$

These quantities are essentially affected by η_e, which can be calculated knowing the reabsorption coefficient and the medium geometry. The average reabsorption coefficient $\sigma_{ph,r}$ is determined by the overlap between the absorption and fluorescence spectra [49]. For a 2%-doped Yb^{3+}:ZBLAN, $\sigma_{ph,r} = 0.266$ cm^{-1} [49], and this value is used here for our estimation. For the thin cylinder medium, the average distance that a photon travels to escape the medium, L_{ave}, is estimated to be the diameter D. Then, the escape efficiency is approximated as

$$\eta_e = \exp(-\sigma_{ph,r} L_{ave}) = 0.995. \tag{3.8}$$

This is only 0.5% less than unity, due essentially to the small size of our sample. If the intrinsic quantum efficiency η_{e-ph} is 0.99, then the external quantum efficiency is found using Eq. (3.7) to be

$$\tilde{\eta}_{e-ph} = 0.98995, \tag{3.9}$$

which differs from the intrinsic quantum efficiency η_{e-ph} by only 0.005%. As a result, the red-shift of the mean fluorescence wavelength is also negligible. Therefore, for the small size medium considered here, the effect of reabsorption on the laser cooling

performance is safely neglected in the analysis that follows, and η_e is assumed to be unity.

The absorption rate $\dot{\gamma}_{e,a}$ is proportional to the energy density of the pumping field, as [64],

$$\dot{\gamma}_{e,a} = B_{e,a} e_{ph,i}. \tag{3.10}$$

Here, the excitation coefficient $B_{e,a}$ has a similar role with the Einstein B coefficient [64]. Note that, Einstein B coefficient describes the photon-electron coupling strength on resonance, while here $B_{e,a}$ describes the phonon-assisted photon-electron coupling strength. In Eq. (3.10), $e_{ph,i}$ is the energy density of the pumping field inside the nanopowder, given by the following expression for a monochromatic electromagnetic wave [65]

$$e_{ph,i} = \frac{1}{2} \epsilon_{e,r} |E|^2, \tag{3.11}$$

where $\epsilon_{e,r}$ is the real part of the permittivity of the medium, and $|E|$ is the amplitude of the local electric field. Alternatively, from the particle (photon) point of view, $e_{ph,i}$ can be written as

$$e_{ph,i} = \hbar_{\mathrm{P}} \omega_{ph,i} n_{ph,i}, \tag{3.12}$$

where $n_{ph,i}$ is the number density of the pumping photons. Equations (3.11) and (3.12) are compatible in that they are the classical and quantum pictures of light.

At steady state, Eq. (3.1) becomes

$$\frac{dn_b}{dt} = -\dot{\gamma}_{e,d} n_b + \dot{\gamma}_{e,a} n_a = 0. \tag{3.13}$$

Since one excitation transition leads to the absorption of one incident photon with the energy $\hbar_{\mathrm{P}}\omega_{ph,i}$ from the pumping field, the local absorbed power per unit volume is given by

$$\dot{s}_{ph,a} = \hbar_{\mathrm{P}}\omega_{ph,i}\dot{\gamma}_{e,a}n_a = \hbar_{\mathrm{P}}\omega_{ph,i}B_{e,a}n_a e_{ph,i}. \tag{3.14}$$

By definition, the absorption coefficient $\sigma_{ph,i}$ is given by

$$\sigma_{ph,i} = \frac{\dot{s}_{ph,a}}{I_{ph,i}} = \frac{\dot{s}_{ph,a}}{u_{ph,i}e_{ph,i}}, \tag{3.15}$$

where $I_{ph,i}$ and $u_{ph,i}$ are the intensity and speed of the pumping light. Substituting Eq. (3.14) into Eq. (3.15), we can write the absorption coefficient, a macroscopic quantity, in terms of atomistic scale quantities as

$$\sigma_{ph,i} = \frac{\hbar_{\mathrm{P}}\omega_{ph,i}B_{e,a}n_a}{u_{ph,i}}. \tag{3.16}$$

This indicates that the absorption coefficient $\sigma_{ph,i}$ is proportional to the excitation coefficient $B_{e,a}$, and the number density of absorbers n_a, as expected. The total absorbed power is then given by

$$Q_{ph,a} = \int_{V_s} \dot{s}_{ph,a}dV_s = \hbar_{\mathrm{P}}\omega_{ph,i}\int_{V_s} \dot{\gamma}_{e,a}n_a dV_s. \tag{3.17}$$

The absorptance $\alpha_{ph,i}$ can then be calculated using

$$\alpha_{ph,i} = \frac{Q_{ph,a}}{Q_{ph,i}}. \tag{3.18}$$

Similarly, one radiative decay transition leads to the emission of a photon with a mean energy $\hbar_{\mathrm{P}}\bar{\omega}_{ph,e}$. The total emitted power is thus given by

$$Q_{ph,f} = \hbar_{\mathrm{P}}\bar{\omega}_{ph,e}\int_{V_s} \dot{\gamma}_{e,r}n_b dV_s. \tag{3.19}$$

Substituting Eqs. (3.2) and (3.13) into Eq. (3.19), we are able to write the emitted power in terms of the absorbed power as

$$\begin{aligned} Q_{ph,f} &= \hbar_{\mathrm{P}}\bar{\omega}_{ph,e}\eta_{e-ph}\int_{V_s} B_{e,a}n_a e_{ph,i}dV_s \\ &= \frac{\bar{\omega}_{ph,e}}{\omega_{ph,i}}\eta_{e-ph}Q_{ph,a}. \end{aligned} \tag{3.20}$$

The net cooling power $\dot{S}_{ph\text{-}e\text{-}p}$ is then calculated as the difference between the absorbed and emitted radiation, i.e.,

$$\begin{aligned} \dot{S}_{ph\text{-}e\text{-}p} &= Q_{ph,a} - Q_{ph,f} \\ &= \left(1 - \frac{\bar{\omega}_{ph,e}}{\omega_{ph,i}}\eta_{e-ph}\right) Q_{ph,a} \\ &= \left(1 - \frac{\lambda_{ph,i}}{\bar{\lambda}_{ph,e}}\eta_{e-ph}\right) \hbar_{\mathrm{P}}\omega_{ph,i}B_{e,a}n_a \int_{V_s} e_{ph,i}dV_s, \end{aligned} \tag{3.21}$$

where we have assumed that in the solid phase the dopant concentration is spatially homogeneous (n_a is a constant). This definition indicates that a negative value of $\dot{S}_{ph\text{-}e\text{-}p}$ represents cooling. As a result, only those $\lambda_{ph,i}$ larger than $\bar{\lambda}_{ph,e}$ may result in cooling, and this range is defined as the cooling regime. Also, the quantum efficiency η_{e-ph} must be larger than $\bar{\lambda}_{ph,e}/\lambda_{ph,i}$, which is satisfied in cooling experiments on bulk crystals. Note that we have assumed that the quantum efficiency of nanopowders is the same as that of bulk materials. There are reports of decreased quantum efficiency in nanocrystals, due to surface defects, adsorbed gas molecules, or other quenching centers [66].

The off-resonance absorption in laser cooling experiments is generally very small, and the system can thus be safely assumed to be far from saturation, i.e., the electronic population of the ground state is much larger than that of the excited state. As such,

the ground state population can be approximated as the dopant concentration, i.e.,

$$n_a = n_d. \tag{3.22}$$

By defining a total pumping field energy inside the medium as

$$E_{pump} = \int_{V_s} e_{ph,i} dV_s, \tag{3.23}$$

the net cooling power becomes

$$\dot{S}_{ph\text{-}e\text{-}p} = \left(1 - \frac{\bar{\omega}_{ph,e}}{\omega_{ph,i}} \eta_{e-ph}\right) \hbar_{\mathrm{P}} \omega_{ph,i} B_{e,a} n_d E_{pump}. \tag{3.24}$$

3.3 A Fermi golden rule calculation of the excitation rate

As the pumping wavelength is tuned to the red side of the resonance, the probability of a purely electronic transition between electronic sublevels, a first order process, becomes smaller. On the other hand, the phonon-assisted transition, a second-order process, starts to contribute significantly to absorption. As a result, the absorption turns out to be a combination of the first- and second-order transitions. Since a much longer pumping wavelength than the resonance is used in laser cooling, the total transition is believed to be dominated by the second-order process. Therefore, only the second-order process will be analyzed here for the purpose of understanding the role of phonons in laser cooling.

In the second order process, the ion in its ground state absorbs a photon from the irradiation and simultaneously a phonon from the lattice, and goes up to the excited

state. The probability per unit time of such a process can be evaluated using the perturbation theory. The Hamiltonian for the physical system considered is given by [22]

$$\mathrm{H} = \mathrm{H}_{ion} + \mathrm{H}_{p} + \mathrm{H}_{ph} + \varphi_{ion-ph} + \varphi_{ion-p}. \tag{3.25}$$

The first term is

$$\mathrm{H}_{ion} = \hbar_{\mathrm{P}}\omega_{e,g} a^{+} a, \tag{3.26}$$

i.e., the Hamiltonian of the ion electronic levels, where $\hbar_{\mathrm{P}}\omega_{e,g}$ is the energy difference between the optically active energy levels of the dopant ion (considered as a two-level ion) and $a^{+}(a)$ is the creation (annihilation) operator of an electronic excitation. The second term is

$$\mathrm{H}_{p} = \sum_{p} \hbar_{\mathrm{P}}\omega_{p} b_{p}^{+} b_{p}, \tag{3.27}$$

i.e., the phonon field Hamiltonian, where ω_{p} is the phonon frequency and $b_{p}^{+}(b_{p})$ is the creation (annihilation) operator of a phonon in mode p. The third term is

$$\mathrm{H}_{ph} = \hbar_{\mathrm{P}}\omega_{ph,i} c^{+} c, \tag{3.28}$$

i.e., the electromagnetic laser field Hamiltonian, where $\omega_{ph,i}$ is the pumping frequency and $c_{p}^{+}(c_{p})$ is the creation (annihilation) operator of a photon. The fourth term is

$$\begin{aligned} \varphi_{ion-ph} &= -\boldsymbol{e}_{\alpha} \cdot \boldsymbol{\mu}_{e} \left(\frac{\hbar_{\mathrm{P}}\omega_{ph,i}}{2\epsilon_{\mathrm{o}} V_{s}} \right)^{1/2} (a^{+} + a)(c^{+} + c) \\ &= C_{ph}(a^{+} + a)(c^{+} + c), \\ C_{ph} &= -\boldsymbol{e}_{\alpha} \cdot \boldsymbol{\mu}_{e} \left(\frac{\hbar_{\mathrm{P}}\omega_{ph,i}}{2\epsilon_{\mathrm{o}} V_{s}} \right)^{1/2}, \end{aligned} \tag{3.29}$$

i.e., the ion-photon interaction Hamiltonian, where as mentioned before, $\boldsymbol{e}_\alpha$ is the polarization factor of the photon, $\boldsymbol{\mu}_e$ is the dipole moment of the electronic transition, ϵ_o is the vacuum permittivity, and V_s is the interacting volume. Note that the term $[\hbar_\mathrm{P}\omega_{ph,i}/(2\epsilon_\mathrm{o}V_s)]^{1/2}$ is the electric field per photon. The fifth term is

$$\begin{aligned} \varphi_{ion-p} &= a_{i-p}\left(\frac{\hbar_\mathrm{P}\omega_p}{2\rho u_p^2}\right)^{1/2} a^+a(b_p - b_p^+) \\ &= C_p a^+a(b_p - b_p^+), \\ C_p &= a_{i-p}\left(\frac{\hbar_\mathrm{P}\omega_p}{2\rho u_p^2}\right)^{1/2}, \end{aligned} \tag{3.30}$$

i.e., the ion-phonon interaction Hamiltonian, where a_{i-p} is the ion-phonon coupling constant and is purely imaginary, u_p is the speed of sound, and ρ is the mass density.

The transition rate $\dot{\gamma}_{e,a}$ is given by the Fermi golden rule [22]

$$\dot{\gamma}_{e,a} = \sum_f \dot{\gamma}_{e,i\text{-}f} = \frac{2\pi}{\hbar_\mathrm{P}} \sum_f |M_{fi}|^2 \delta_\mathrm{D}(E_f - E_i), \tag{3.31}$$

where E_i and E_f are the initial and final energies of the system. The M_{fi} matrix can be expanded as the following series [22]

$$\begin{aligned} M_{fi} = \langle f|\varphi_{int}|i\rangle + \sum_m \frac{\langle f|\varphi_{int}|m\rangle\langle m|\varphi_{int}|i\rangle}{E_{e,i}^T - E_{e,m}^T} + \\ \sum_{m,n} \frac{\langle f|\varphi_{int}|m\rangle\langle m|\varphi_{int}|n\rangle\langle n|\varphi_{int}|i\rangle}{(E_{e,i}^T - E_{e,m}^T)(E_{e,i}^T - E_{e,n}^T)} + ..., \end{aligned} \tag{3.32}$$

with $\varphi_{int} = \varphi_{ion-ph} + \varphi_{ion-p}$. The summations on m and n include all the intermediate phonon and photon states.

We will calculate the transition probability $\dot{\gamma}_e$ between the initial $|i\rangle = |\psi_i, f_{ph} + 1, f_p + 1\rangle$ and final $|f\rangle = |\psi_f, f_{ph}, f_p\rangle$ states of the system, where the first ket element, ψ_i, refers to the ion state, the second one, f_{ph}, to the photon number in the interacting

volume V_s, and the third one, f_p, to the phonon distribution function. This type of processes only appears in the second order perturbation expansion of the M_{fi} matrix, which is [67, 68]

$$\begin{aligned} M_{fi,2nd} &= \sum_m \frac{\langle f|\varphi_{int}|m\rangle\langle m|\varphi_{int}|i\rangle}{E^T_{e,i} - E^T_{e,m}} \\ &= \sum_m \Bigg[\frac{\langle \psi_f, f_{ph}, f_p|\varphi_{ion\text{-}ph}|\psi_m, f_{ph}+1, f_p\rangle \times}{E_i - (E_m - \hbar_{\rm P}\omega_p)} \\ &\quad \langle \psi_m, f_{ph}+1, f_p|\varphi_{ion\text{-}p}|\psi_i, f_{ph}+1, f_p+1\rangle \\ &+ \frac{\langle \psi_f, f_{ph}, f_p|\varphi_{ion\text{-}p}|\psi_m, f_{ph}, f_p+1\rangle \times}{E_i - (E_m - \hbar_{\rm P}\omega_{ph})} \\ &\quad \langle \psi_m, f_{ph}, f_p+1|\varphi_{ion\text{-}ph}|\psi_i, f_{ph}+1, f_p+1\rangle \Bigg]. \end{aligned} \tag{3.33}$$

The sum runs over all possible intermediate states of the system. Substituting the expressions for the interaction Hamiltonians into Eq.(3.33), we have

$$\begin{aligned} M_{fi,2nd} &\simeq \sum_m \frac{\langle \psi_f, f_{ph}, f_p|C_{ph}(a^+ + a)(c^+ + c)|\psi_m, f_{ph}+1, f_p\rangle \times}{E_i - (E_m - \hbar_{\rm P}\omega_p)} \\ &\quad \langle \psi_m, f_{ph}+1, f_p|a_{i\text{-}p}C_p a^+ a(b_p - b_p^+)|\psi_i, f_{ph}+1, f_p+1\rangle \\ &= \sum_m \frac{\langle \psi_f, f_{ph}, f_p|C_{ph}(a^+ + a)(c^+ + c)|\psi_m, f_{ph}+1, f_p\rangle \times}{E_i - (E_m - \hbar_{\rm P}\omega_p)} \\ &\quad \langle \psi_m, f_{ph}+1, f_p|C_p a^+ a(b_p - b_p^+)|\psi_i, f_{ph}+1, f_p+1\rangle \\ &= \sum_m \frac{\langle \psi_f, f_{ph}, f_p|C_{ph}(a^+ + a) f_{ph}^{1/2}|\psi_m, f_{ph}, f_p\rangle \times}{E_i - (E_m - \hbar_{\rm P}\omega_p)} \\ &\quad \langle \psi_m, f_{ph}+1, f_p|C_p a^+ a f_p^{1/2}|\psi_i, f_{ph}+1, f_p\rangle \\ &= \sum_m C_{ph} f_{ph}^{1/2} C_p f_p^{1/2} \frac{\langle \psi_f|(a^+ + a)|\psi_m\rangle\langle \psi_m|a^+ a|\psi_i\rangle}{E_i - (E_m - \hbar_{\rm P}\omega_p)}, \end{aligned} \tag{3.34}$$

where, the second term in Eq.(3.33) has been neglected since the photon energy is much greater than the phonon energy [68].

Since the phonon energy $\hbar_{\rm P}\omega_p$ is much smaller than the energy gap, it cannot by itself induce an electronic transition. In the perturbation theory, the intermediate

wave function ψ_m is then approximated as unperturbed, i.e., $\psi_m = \psi_i$, and $E_m = E_i$. Therefore Eq. (3.34) becomes

$$\begin{aligned} M_{fi,2nd} &= \sum_p C_{ph} f_{ph}^{1/2} C_p f_p^{1/2} \frac{\langle \psi_f | (a^+ + a) | \psi_i \rangle \langle \psi_i | a^+ a | \psi_i \rangle}{E_i - (E_i - \hbar_{\rm P}\omega_p)} \\ &= \sum_p C_{ph} f_{ph}^{1/2} C_p f_p^{1/2} \frac{\langle \psi_f | (a^+ + a) | \psi_i \rangle \langle \psi_i | a^+ a | \psi_i \rangle}{E_i - (E_i - \hbar_{\rm P}\omega_p)} \\ &= \sum_p C_{ph} f_{ph}^{1/2} C_p f_p^{1/2} \frac{1}{\hbar_{\rm P}\omega_p}. \end{aligned} \tag{3.35}$$

Substituting Eq. (3.35) into Eq. (3.31), we have

$$\dot{\gamma}_{e,a} = \sum_f \dot{\gamma}_{e,i\text{-}f} = \frac{2\pi}{\hbar_{\rm P}} \sum_p (\frac{C_{ph}|C_p|}{\hbar_{\rm P}\omega_p})^2 f_{ph} f_p \delta(\hbar_{\rm P}\omega_{ph,i} + \hbar_{\rm P}\omega_p - \hbar_{\rm P}\omega_{e,g}). \tag{3.36}$$

In order to perform the summation on the phonon modes in Eq. (3.36), we must introduce the phonon DOS $D_p(E_p)$, where E_p is the phonon energy given by $E_p = \hbar_{\rm P}\omega_{e,g} - \hbar_{\rm P}\omega_{ph,i}$. In terms of this distribution function, the transition rate, Eq. (3.36), becomes

$$\begin{aligned} \dot{\gamma}_{e,a} &= \frac{2\pi}{\hbar_{\rm P}} C_{ph}^2 f_{ph} \frac{|a_{i\text{-}p}|^2}{2\rho u_p^2} \int_{E_{min}}^{E_{max}} dE_p D_p(E_p) \frac{f_p^{\rm o}(E_p)}{E_p} \delta(\hbar_{\rm P}\omega_{ph,i} + E_p - \hbar_{\rm P}\omega_{e,g}) \\ &= \frac{2\pi}{\hbar_{\rm P}} C_{ph}^2 f_{ph} \frac{|a_{i\text{-}p}|^2}{2\rho u_p^2} \frac{D_p(E_p) f_p^{\rm o}(E_p)}{E_p}. \end{aligned} \tag{3.37}$$

This result implies that the excitation spectra can be associated with the phonon spectra, as observed in [69]. We here have used the equilibrium distribution functions for phonons. To compare with Eq. (3.10), we rewrite Eq. (3.37) as

$$\begin{aligned} \dot{\gamma}_{e,a} &= \frac{2\pi}{\hbar_{\rm P}} \frac{(\boldsymbol{e}_\alpha \cdot \boldsymbol{\mu}_e)^2}{2\varepsilon_{\rm o}} \frac{|a_{i\text{-}p}|^2}{2\rho u_p^2} \frac{D_p(E_p) f_p^{\rm o}(E_p)}{E_p} \hbar_{\rm P}\omega_{ph,i} \frac{f_{ph}}{V_s} \\ &= \frac{2\pi}{\hbar_{\rm P}} \frac{(\boldsymbol{e}_\alpha \cdot \boldsymbol{\mu}_e)^2}{2\varepsilon_{\rm o}} \frac{|a_{i\text{-}p}|^2}{2\rho u_p^2} \frac{D_p(E_p) f_p^{\rm o}(E_p)}{E_p} e_{ph,i}. \end{aligned} \tag{3.38}$$

This expression is found to be consistent with Eq. (3.10), as expected. Therefore, we

are able to extract the excitation coefficient $B_{e,a}$ from Eq. (3.38), as

$$B_{e,a} = \frac{2\pi}{\hbar_{\mathrm{P}}} \frac{(\boldsymbol{e}_\alpha \cdot \boldsymbol{\mu}_e)^2}{2\varepsilon_{\mathrm{o}}} \frac{|a_{i\text{-}p}|^2}{2\rho u_p^2} \frac{D_p(E_p) f_p^{\mathrm{o}}(E_p)}{E_p}. \tag{3.39}$$

Using the relations $\omega = 2\pi c_{\mathrm{o}}/\lambda$ and $E_p = \hbar_{\mathrm{P}}\omega_{e,g} - \hbar_{\mathrm{P}}\omega_{ph,i}$, the above expression for $B_{e,a}$ can be written as a function of $\lambda_{ph,i}$ as

$$B_{e,a} = \frac{2\pi}{\hbar_{\mathrm{P}}} \frac{(\boldsymbol{e}_\alpha \cdot \boldsymbol{\mu}_e)^2}{2\varepsilon_{\mathrm{o}}} \frac{|a_{i\text{-}p}|^2}{2\rho u_p^2} \frac{D_p(\hbar_{\mathrm{P}}\frac{2\pi c_{\mathrm{o}}}{\lambda_{e,g}} - \hbar_{\mathrm{P}}\frac{2\pi c_{\mathrm{o}}}{\lambda_{ph,i}}) f_p^{\mathrm{o}}(\hbar_{\mathrm{P}}\frac{2\pi c_{\mathrm{o}}}{\lambda_{e,g}} - \hbar_{\mathrm{P}}\frac{2\pi c_{\mathrm{o}}}{\lambda_{ph,i}})}{\hbar_{\mathrm{P}}\frac{2\pi c_{\mathrm{o}}}{\lambda_{e,g}} - \hbar_{\mathrm{P}}\frac{2\pi c_{\mathrm{o}}}{\lambda_{ph,i}}}. \tag{3.40}$$

The total cooling power, expressed in the atomic level quantities, is

$$\dot{S}_{ph\text{-}e\text{-}p} = 2\pi \left(1 - \frac{\bar{\omega}_{ph,e}}{\omega_{ph,i}}\eta_{e-ph}\right) \omega_{ph,i} \frac{(\boldsymbol{e}_\alpha \cdot \boldsymbol{\mu}_e)^2}{2\varepsilon_{\mathrm{o}}} \frac{|a_{i\text{-}p}|^2}{2\rho u_p^2} \frac{D_p(E_p) f_p^{\mathrm{o}}(E_p)}{E_p} n_d E_{pump}. \tag{3.41}$$

3.4 Discussions and summary

In Eq. (3.41) the factors affecting laser cooling power are shown. Thus, to enhance the cooling power using the same incident energy, increases in the carrier couplings and populations are needed. The couplings include the photon-electron coupling and the electron-phonon coupling, and the populations include the the dopant concentration n_d, and the total pumping field energy inside the nanopowder medium E_{pump}. Despite the complicated presentation of the Fermi golden rule, this understanding turns out straightforward if one recognize that laser cooling relies on the off-resonance absorption, which is a photon-induced, phonon-assisted, electronic transition. In the following sections, we will explore in great detail how to understand and enhance these limiting factors.

Chapter 4

Ab initio calculations of photon-electron and electron-vibration couplings

4.1 Introduction

In the last chapter we have used the Fermi golden rule to decouple various limiting factors for laser cooling of solids. The absorption rate is ultimately expressed as Eq. (3.38). Based on this expression, one finds that the cooling performance is limited by the populations of the three carriers and their couplings. An understanding to link the photon-electron and ion-phonon coupling mechanisms to the atomic structure, especially in the quantitative level, is lacking in spite of their fundamental importance.

In the sections followed, using an $Ti[(H_2O)_6]^{3+}$ complex as the modal system, the roles played by the electron-photon and electron-phonon couplings in laser cooling of

solids will be discussed, and an ab initio approach to calculate these coupling rates using their atomic structure will be developed. The electron-photon and electron-phonon coupling rates are attempted using ab initio calculations. The electron-photon coupling is routed in the transition dipole moment which connects the ground and excited states. The wavefunctions are calculated and the transition dipole moment is determined using its definition solely. The vibrational frequencies and energy minima are calculated for normal modes, using the small-displacement approach. These are used along with the electronic wavefunctions, in the Fermi golden rule, to derive the nonradiative decay rates. Finally the roles of electron-photon and electron-vibration couplings in laser cooling materials selection will be discussed.

4.2 Ab initio calculations of the ground and excited states

4.2.1 Ground state geometry optimization

The calculation is performed using Gaussian 03 Package [70], with the B3LYP method and the 6-311+G* basis set. The Ti^{3+} ion has a single unpaired electron, which gives a spin multiplicity of 2 for the complex. To avoid convergence problems of the self consistent function (SCF), a quadratic convergent (QC) procedure has been applied. No symmetry restriction was prescribed at the start of the calculation, and the optimized geometry converges to the D_{3d} all vertical symmetry, as shown in Fig. 4.1. This symmetry is lower than the O_h point group and higher than C_i.

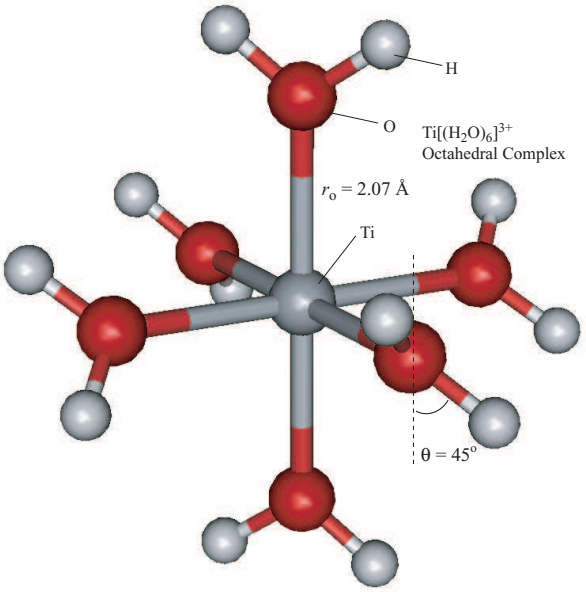

Figure 4.1: The optimized geometry of the ground state $Ti[(H_2O)_6]^{3+}$ (hydrated titanium) complex.

The calculated Ti-O bond length is 2.07 Å, which agrees well with the experimental value 2.03 Å [71] and previously reported ground-state calculations on this complex [72, 73].

4.2.2 Excited state calculations

Excited state calculations have previously been performed on the $Ti[(H_2O)_6]^{3+}$ complex using a multi-reference single- and double-excitation CI (MR-SD-CI) method [72]. Here we use the time-dependent density functional theory (TDDFT), which is regarded as the most accurate method for excited states, to calculate the energy levels for the complex at the ground state equilibrium geometry. For a free-standing Ti^{3+} ion, it has 5 degenerate d levels, with the orbitals shown in Fig. 4.2. As the

ion is put into an octahedral crystal field of the six surrounding oxygen atoms, the levels are split into two groups, three levels for the ground state and two levels for the excited state. The Jahn-Teller effect further splits the ground state into two multiplets, with an energy gap of 6,046 cm^{-1}. The Jahn-Teller theorem states that any complex occupying an energy level with electronic degeneracy is unstable against a distortion that removes that degeneracy in first order. The vibronic coupling of ions in solids can cause a local distortion of the lattice in which the atoms move in the direction of normal-mode displacement to lift the electronic degeneracy. A new equilibrium position is achieved in which the local symmetry is lower than the point-group symmetry of the crystal. Here for the $Ti[(H_2O)_6]^{3+}$ complex the symmetry is lowered from the O_h to D_{3d}. The evolution of the energy levels is shown in Fig. 4.3.

4.3 Electron-photon coupling and the radiative decay rate

A photon can be absorbed by an ion if the coupling factor $\boldsymbol{e}_\alpha \cdot \boldsymbol{\mu}_e$ is nonzero (i.e., they are not orthogonal), where $\boldsymbol{e}_\alpha$ is the polarization vector of the electromagnetic field, and $\boldsymbol{\mu}_e$ is the effective transition dipole moment of the ion. The transition dipole moment is defined as a quantum mechanical spatial integral of the classical dipole moment $e_e\boldsymbol{r}$, i.e.,

$$\boldsymbol{\mu}_e = \int \psi_f^* e_e \boldsymbol{r} \psi_i d^3 r, \tag{4.1}$$

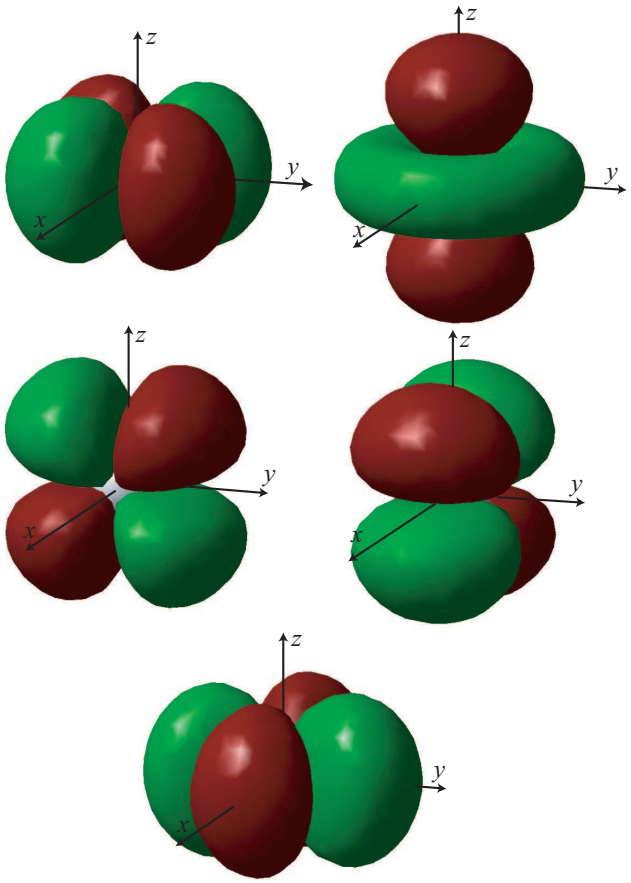

Figure 4.2: The 3d orbitals of a single Ti^{3+} ion.

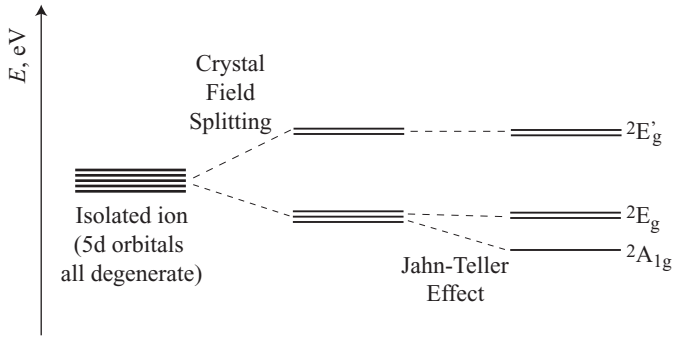

Figure 4.3: Calculated energy levels of the $Ti[(H_2O)_6]^{3+}$ complex at the ground state equilibrium geometry. The Ti-O bond length is $r_o = 2.07$ Å. The energy multiplets due to the crystal field and the Jahn-Teller effect are shown.

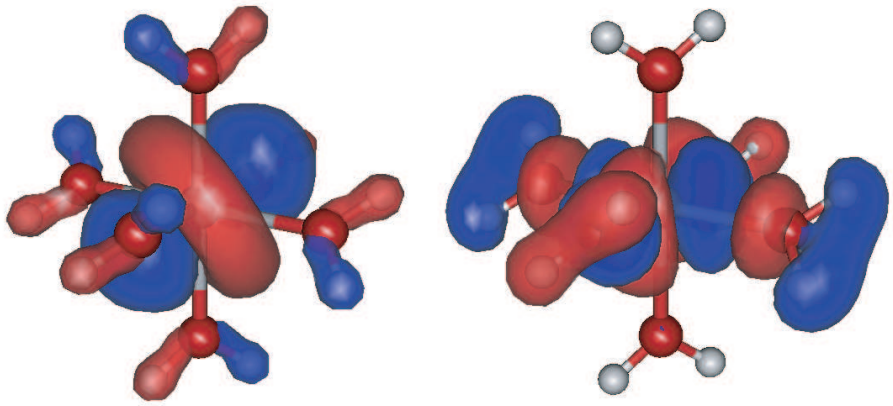

(a) (b)

Figure 4.4: Calculated wavefunctions of the ground and excited states.

where, e_e is the electron charge, $\boldsymbol{r}$ is the position vector, and ψ_i and ψ_f are the ground and excited state wave functions. These wavefunctions are calculated with Gaussian and are shown in Fig. 4.4. The ab initio calculations showed that the energies of the orbitals below the HOMO (highest occupied molecular orbital) are approximately the same for the ground and the excited electronic states, so that the differences of the state energies can be discussed with these singly occupied molecular orbital (SOMO) energies. Based on the theory of local combination of atomic orbitals (LCAO) [74], the ground state is mainly composed of the $3d_{z^2}$ orbital, and the excited state is dominated by the $3d_{x^2-y^2}$ orbital. The transition dipole moment is then calculated using Eq. (4.7), which gives 0.002 Debye (1.859×10^{-32} C·m).

A variety of parameters are used to describe the light-electron interaction, such as the Einstein A and B coefficients, the radiative lifetime τ_r, the oscillator strength, the absorption cross section, etc. These parameters are all governed by a fundamental

atomistic scale quantity: the transition dipole moment. For example, the Einstein A coefficient (equivalent to the radiative decay rate $\dot{\gamma}_r$) and the radiative lifetime τ_r are related to the transition moment by [75]

$$A = \dot{\gamma}_r = \frac{\omega_{e,g}^3}{3\pi\epsilon_o\hbar c^3}|\boldsymbol{\mu}_e|^2 \tag{4.2}$$

$$\tau_r = \frac{1}{\dot{\gamma}_r} = \frac{3\pi\epsilon_o\hbar c^3}{\omega_{e,g}^3}\frac{1}{|\boldsymbol{\mu}_e|^2}, \tag{4.3}$$

where ϵ_o is the electric permitivity in vacuum, and $\hbar$ is the Planck constant divided by 2π. The calculated radiative lifetime for the complex at equilibrium configuration is 12 ms, much longer than the experimental value for Ti:sapphire laser system, which is only 3 μs [76, 77]. This discrepancy might be due to the the defects and impurities in a real material, which significantly modify the symmetry properties around the ion.

4.4 Electron-vibration coupling

The atoms in a solid are never completely at rest. The thermal vibrations of the atoms modulate the local crystal field at the site of an optically active ion. This modulation can have several types of effects on the optical properties of the doped ion. For example, it can modulate the position of the electronic energy levels, leading to a broadening and shifting in peak position of the spectral transition. Also it can cause transitions to occur between electronic energy levels accompanied by the absorption or emission of vibrational energy but with or without the emission or absorption of photons.

4.4.1 Normal mode analysis for vibrations

The coupling of an electron to a specific vibrational mode is essentially the change of the electronic property in response to the lattice displacement along that vibrational mode. The normal vibrational modes of the $Ti[(H_2O)6]^{3+}$ complex can be conveniently calculated with Gaussian, after the geometry is optimized. Among all calculated modes, we only consider those which are also observed for the octahedral TiO_6 core. The modes due to the hydrogen atoms only do not contribute significantly to the electron-phonon coupling, since these modes are screened by the more inner oxygen atoms. The vibrational normal modes and frequencies are shown in Fig. 4.5.

4.4.2 Configuration coordinate diagram

Configuration coordinate diagram is often used to describe transitions between electronic transitions coupled to vibrations. It depicts the variation in the electronic energy levels with respect to the displacement of the normal vibrational coordinate away from its equilibrium position. Here since the vibration modes due to hydrogen atoms have very little effect on the energy level of the Ti^{3+} ion, we only concern the vibration of the octahedral TiO_6 core. For these modes the hydrogen atoms move rigidly with the oxygen atoms.

The configuration coordinate diagram is obtained by calculating the energy levels with respect to the normal coordinate of a specific vibrational mode. Shown in Fig. 4.6 is the configuration coordinate diagram corresponding to the A_{1g} normal mode. Five levels resulted from the 3d orbitals are shown. As discussed in Fig. 4.3, we

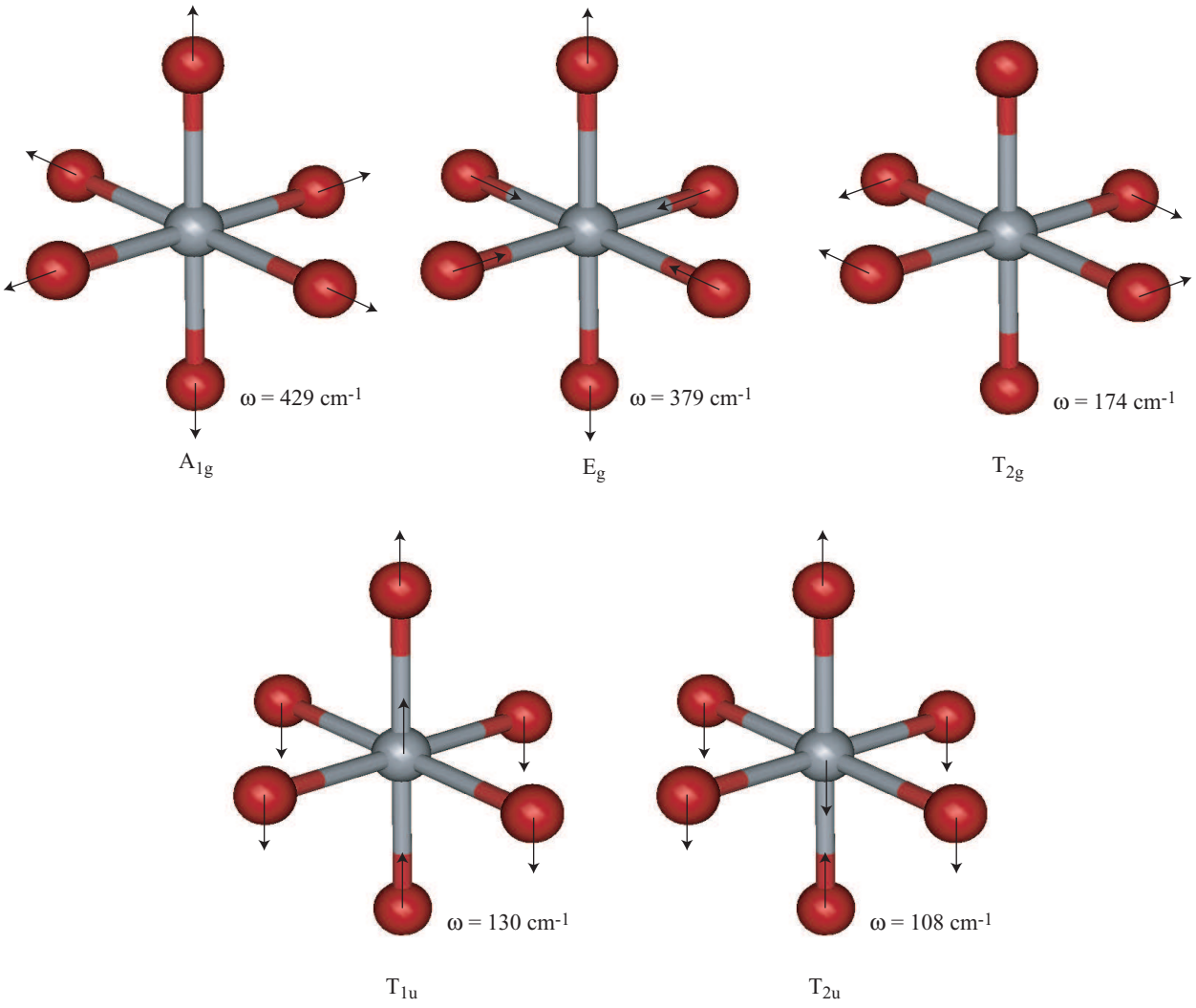

Figure 4.5: The vibrational normal modes along with the frequencies of the $Ti[(H_2O)_6]^{3+}$ complex.

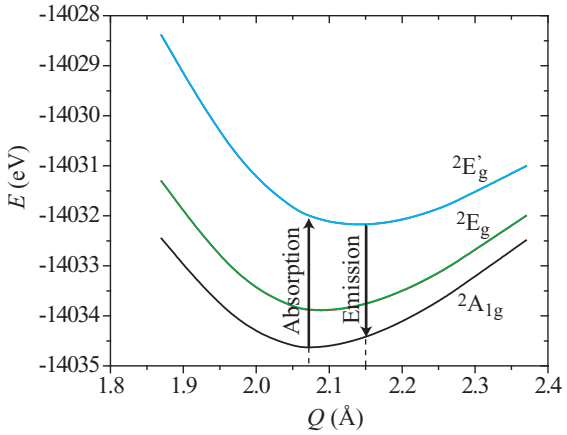

Figure 4.6: Configuration coordinate diagram corresponding to the A_{1g} normal mode.

have the ground state $^2A_{1g}$, the first excited state ^2E_g which is composed of two nearly degenerate levels, and the second excited state $^2E'_g$ which is also composed of two nearly degenerate levels. The transition between the $^2A_{1g}$ and $^2E'_g$ levels is very important in lasers and luminescent applications, and therefore we will only concern these two states in the following sections. As shown in the figure, the potential energy minimum for the excited state is shifted to the right to that of the ground state, as expected. This shift leads to the well-known Stokes shift in the emission wavelength. For the excited state, the electron is normally farther away from its nuclei than the ground state, repelling the surrounding oxygen atoms. As the result, the equilibrium Ti-O bond length for the excited state becomes longer than the ground state, which in turn leads to a smaller force constant and vibrational frequency - the curvature for the excited state is flatter than that for ground state. To take into account the modifications of both normal coordinates and frequencies between the electronic

states, we can express them in general as follows:

$$Q' = Q + d \tag{4.4}$$

$$\omega'_s = \omega_s(1 - \rho), \tag{4.5}$$

where d is the shift of the energy minimum, and ρ is the percentage of the frequency shift. As will be seen later, only these normal modes which have modifications in either normal coordinates or frequencies between the electronic states concerned, can contribute to the radiationless transition probability. The Huang-Rhys coupling factor S was found to be written as

$$S_s = \frac{M\omega_s d^2}{2\hbar}, \tag{4.6}$$

where M is the mass of the vibrating atom, the O atom here.

4.4.3 Nonradiative transition rates

For electron-vibration coupling, only those normal modes which have modifications in either normal coordinates or frequencies between the electronic states concerned, can contribute to the nonradiative transition probability.

In the Born-Oppenheimer approximation, the system wavefunction ψ is presented as [68]

$$\psi_{i,\nu}(r, Q) = \phi_i(r, Q)\theta_{i,\nu}(Q). \tag{4.7}$$

where $\theta_{i,\nu}(Q)$ is the vibrational wavefunction at a nuclei normal coordinate Q, and $\phi_i(r, Q)$ is the electronic wavefunction for a fixed position of the nuclei. This implies

that the motion of the electron is very rapid compared to the nuclei motion. The Hamiltonian H for the entire system can be chosen as:

$$H = T(Q) + H_i(r) + H_l^{ep}(Q), \tag{4.8}$$

where T is the kinetic-energy operator of all nuclear motions, $H_i(r)$ is the electronic-energy operator for electronic states, and $H_l^{ep}(Q)$ is the electron-lattice interaction potential. In the adiabatic approximation, $\phi_i(r, Q)$ and $\theta_{i,\nu}(Q)$ are solutions of the following Schrödinger equations:

$$[H_i(r) + H_l^{ep}(Q)]\phi_i(r, Q) \;=\; U_i(Q)\phi_i(r, Q) \tag{4.9}$$

$$[T(Q) + U_i(Q)]\theta_{i,\nu}(Q) \;=\; E_{i,\nu}(Q)\theta_{i,\nu}(Q), \tag{4.10}$$

where $U_i(Q)$ is the adiabatic potential of the electronic state at the instataneous positions Q, and ν signifies the over-all vibrational state of the nuclei. Although $\psi_{i,\nu}$ is a good approximation for stationary states, it is not stationary in the exact sense, and the whole system oscillates to and fro among various good quantum states of almost the same energy. This should be interpreted as the transition from one electronic state to another, accompanied by a transition in the quantum states of nuclear motion. The perturbation Hamiltonian H' for the nonradiative transition process is given by [68, 78]

$$H'\psi_{i,\nu}(r, Q) = -\frac{\hbar^2}{2M}\sum_s \frac{\partial\phi_i(r, Q)}{\partial Q_s}\frac{\partial\theta_{i,\nu}}{\partial Q_s} - \frac{\hbar^2}{2M}\sum_s \frac{\partial^2\phi_i(r, Q)}{\partial Q_s^2}\theta_{i,\nu}. \tag{4.11}$$

The nonradiative transition rate $\dot{\gamma}$ is given by the Fermi Golden Rule,

$$\dot{\gamma}_{nr} = \frac{2\pi}{\hbar}\sum_{\nu,\nu'} p_{i\nu}|\langle f\nu'|H'|i\nu\rangle|^2\delta_{\mathrm{D}}(E_{f,\nu'} - E_{i\nu}), \tag{4.12}$$

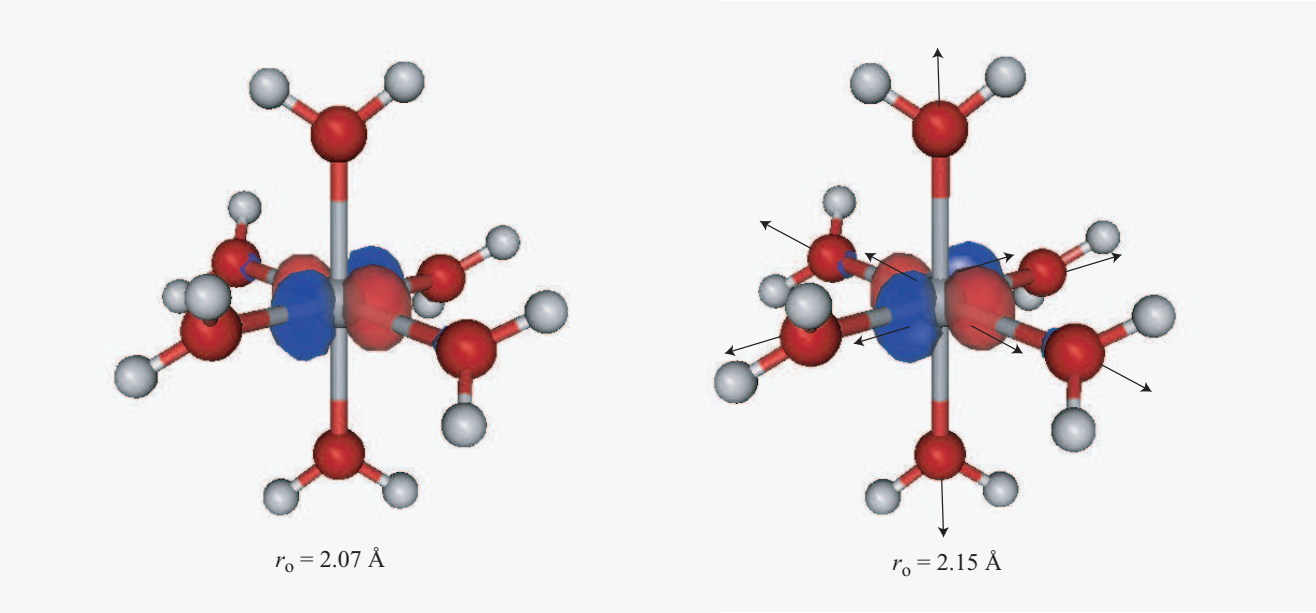

Figure 4.7: The modulation of the excited state wavefunction with respect to the A_{1g} vibrational mode.

where $p_{i\nu}$ is the distribution function for the Boltzmann population of initial vibrational levels and a δ function is used for the density of final states to ensure conservation of energy. Using the electronic and vibrational wavefunctions in Eq. (4.12), we have

$$\dot{\gamma}_{nr} = \frac{2\pi}{\hbar} \sum_{\nu,\nu'} p_{i\nu} |(-\frac{\hbar^2}{M}) \sum_s \langle \phi_f | \frac{\partial \phi_i}{\partial Q_s} \rangle \langle \theta_{f\nu'} | \frac{\partial \theta_{i\nu}}{\partial Q_s} \rangle|^2 \delta_{\mathrm{D}}(E_{f\nu'} - E_{i\nu}). \tag{4.13}$$

Here the electronic part of the matrix element can be defined as

$$R_s(fi) = -\frac{\hbar^2}{M} \langle \phi_f | \frac{\partial \phi_i}{\partial Q_s} \rangle. \tag{4.14}$$

The derivative represents how sensitive the electronic wavefunction is with respect to the displacement along a particular vibrational mode. This is shown in Fig. 4.7.

Equation (4.13) has been evaluated by Lin [78] by replacing the δ function with an integral, and the final result of the transition probability of the nonradiative decay

is

$$\dot{\gamma}_{nr} = \frac{\pi\omega_s}{2\omega_s\hbar^3}|R_s(fi)|^2 \exp[-S_s \coth\frac{\hbar\omega_s}{2kT}][(\coth\frac{\hbar\omega}{2kT}+1)\exp(-i\phi' P_i^+) I_{P_i^+}(S\mathrm{csch}\frac{\hbar\omega}{2kT}) + (\coth\frac{\hbar\omega}{2kT}-1)\exp(-i\phi' P_i^-) I_{P_i^-}(S\mathrm{csch}\frac{\hbar\omega}{2kT})], \tag{4.15}$$

where $I_{P_i^+}$ is the P_i^+th order Bessel function, and P_i^+ and P_i^- are defined as follows:

$$P_i^+ = \frac{1}{\omega}[-\omega_{ab} - \omega_s + \frac{\rho\omega}{2}\coth\frac{\hbar\omega}{2kT}], \tag{4.16}$$

$$P_i^- = \frac{1}{\omega}[-\omega_{ab} + \omega_s + \frac{\rho\omega}{2}\coth\frac{\hbar\omega}{2kT}], \tag{4.17}$$

where ω_{ab} is the energy gap of the ground and excited states.

Using Eq. (4.15), the nonradiative decay rate is calculated as a function of temperature, and is shown in Fig. 4.8(a). The total decay rate is the summation of the radiative and nonradiative rates, as

$$\dot{\gamma}_d = \dot{\gamma}_r + \dot{\gamma}_{nr}, \tag{4.18}$$

and the lifetime is given by

$$\tau_d = \frac{1}{\dot{\gamma}_d}. \tag{4.19}$$

The calculated lifetime in this way is shown in Fig. 4.8(b). As seen, at low temperatures, the nonradiative decay rate is negligibly small compared to the radiative decay rate, so that the lifetime remains almost a constant. As the temperature increases, more phonons are activated and involved in the decay process, and the nonradiative decay rate is increasing rapidly. At around 250 K, the nonradiative decay rate becomes comparable or even larger than the radiative decay rate, and the lifetime drops

significantly with temperature. At high temperatures, the decay process is dominated by the nonradiative decay. The predicted lifetime is compared to that of the Ti:sapphire laser material, which also has an octahedra crystal field around the Ti_{3+} ion. The measured Ti:sapphire lifetime at low temperatures is much shorter than that predicted for $Ti[(H_2O)_6]^{3+}$, because it was not measured at the zero-phonon line, and in real materials defects and impurities may modify the symmetry properties around the Ti ion significantly. At high temperatures, the nonradiative decay rates follow a similar trend. Exact agreement is not expected since the phonon modes for our cluster is different from those in the Ti:sapphire solids.

4.5 Discussions and summary

Laser cooling cycle is realized in five steps: electron-phonon coupling, phonon-assisted absorption, thermalization in the excited state, electronic decay, and thermalization in the ground state. These steps are shown in Fig. 4.9.

In the above sections the kinetics of laser cooling cycle has been presented, by calculating the time scales for each step, as shown in Fig. 4.10. Four characteristic times are marked in the figure, which are the absorption time, thermalization time at the excited state, lifetime, and the thermalization time at the ground state. The absorption time is the longest in the entire cycle, indicating that the absorption is the bottleneck process that limits the laser cooling performance.

The above theoretical framework can be used to guide the selection of laser cooling materials. Based on Eq. (3.38), both the electron-photon and the electron-phonon

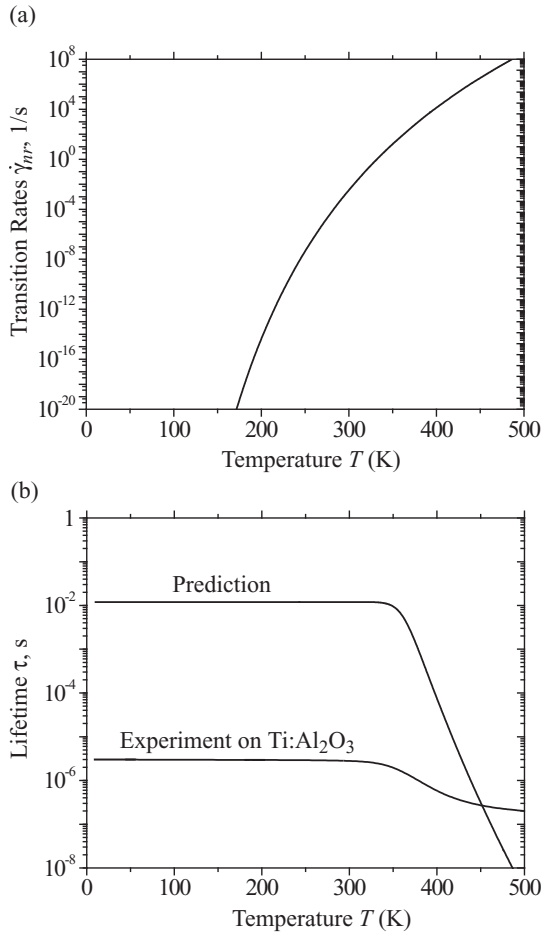

Figure 4.8: (a) The total transition rate with respect to temperature. (b) The lifetime with respect to temperature.

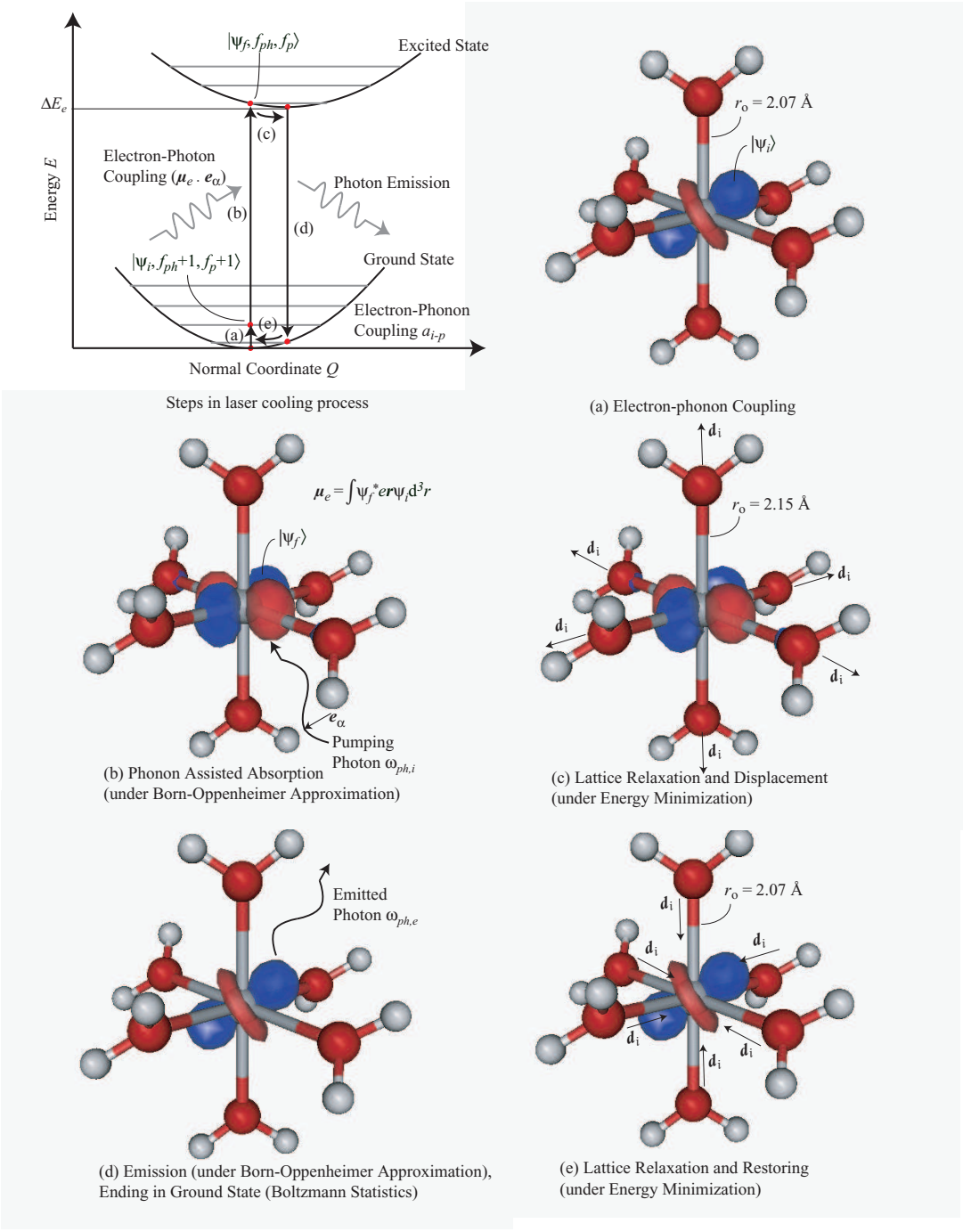

Figure 4.9: (a) The energy diagram, (b)-(e) five steps in the photon-electron-phonon couplings in the laser cooling cycle.

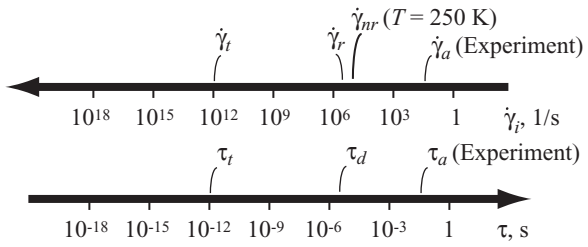

Figure 4.10: Time scales of each step for laser cooling of solids. The phonon-assisted absorption process is the slowest, and is regarded as the bottleneck of laser cooling of solids.

coupling strengths need to be enhanced, to enhance the absorption rate. A negative side effect of the electron-phonon coupling is the nonradiative decay, which leads to heating in the system. However, the operation temperature of laser cooling is no more than the room temperature (300K), and for this temperature range the nonradiative decay rate is negligibly small. Therefore the electron-phonon coupling can be enhanced without deteriorating the radiative decay process. To enhance the photon-electron coupling, the dopant ion and the host should be selected so that the transition dipole moment is large. To enhance the electron-phonon coupling, the electronic wavefunction should be sensitive to vibrations modes, and the modification of vibrational modes before and after transition should be significant. For example, transition metal ions has its valence electrons directly exposed to the crystal field, unlike rare-earth ions for which the valence electrons are shielded by outer electrons, and as a result, transition-metal doped system has a much larger electron-phonon coupling. The ab initio approach developed in this work can be used to guide the selection of laser cooling materials.

Chapter 5

Photon localization and electromagnetic field enhancement in laser irradiated nanopowders

5.1 Introduction

In the expression of the cooling power given by Eq. (3.41), one of the limiting factors is the total pumping energy E_{pump}. To enhance this parameter using nanopowders, the unique radiative transport properties in random porous media need to be understand.

Radiative transport in random porous media has long been an important problem in science and engineering [79, 80, 81]. As a laser beam is irradiated on a non-absorbing random porous medium in which the particle size is much larger than the laser wavelength, the transmissivity reveals a diffusive behavior, i.e., decays inversely

with the medium thickness [82]. Recently, however, it has been found that as the particle size decreases to the order of the laser wavelength, the diffusion breaks down and the transmission coefficient decays exponentially with the medium thickness, due to the constructive interference among the multiply scattered waves [83, 84]. This phenomenon, termed "photon localization", is the counterpart of electron localization suggested by Anderson [85], and has been investigated theoretically and experimentally in one- [86, 87, 88, 89, 90, 91], two- [92, 93, 94, 95, 96, 97, 98] and three- [99, 100, 101, 102] dimensional structures. With the onset of localization, the electromagnetic (EM) waves may not propagate through, but are confined in a finite spatial region, forming a "random resonator". This property has initiated intense research interest in random lasers [103, 61, 104, 105, 106, 107, 108, 109, 110], in which the "random resonator" may replace the resonator in conventional lasers, and remarkably simplify the device.

The interference effects on the radiative transport must be properly addressed in order to understand photon localization. This can be done using the direct simulation, in which Maxwell's equations are solved for the porous medium, and the boundary conditions are matched at the interfaces between particles and pores. Because the geometries of the interfaces are generally complicated, the direct simulation is computationally expensive, except for simple geometries. For example, it has been performed using the transfer matrix method for one-dimensional multilayer [86], and using the FDTD (finite-difference time-domain) or the transfer matrix method [92, 93] for simple two-dimensional random systems. Photon localization is predicted in both dimensions by showing that the calculated transmissivities decay exponentially with

the medium thickness. However, this "transmission" approach does not show explicitly the role played by interference in the onset of localization. Recently, local field amplitudes, rather than transmissivities, have been calculated for one-dimensional random media, and the internal field is found to be orders higher than the incident field [111]. This large field enhancement is exactly a signature of interference, and has a lot of implications.

Traditionally, the effective medium approximations have been used to treat the radiative transport in random porous media, because the direct simulation mentioned above is usually computationally too heavy to be practical. The equation of radiative transfer (ERT) is the most widely used effective medium treatment [112]. The scattering and absorption properties are derived from the spectral radiative behavior of a single isolated particle (Mie scattering) using large and small particle size approximations. The effective properties are then obtained based on the porosity and particle size distribution. Inclusions of the inter-particle interactions (dependent scattering) have also been made [80]. The ERT is then solved using some approximations (e.g. two-flux approximation) to obtain the local radiative intensity. The Maxwell-Garnett approximation is another effective medium approximation for the determination of the effective, bulk dielectric properties of inhomogeneous materials [113]. In this approach the field induced in a uniform host by a single spherical or ellipsoidal inclusion is calculated exactly, and the field's distortion by the electrostatic interaction between the inclusions is treated approximately [114]. The effective permittivity is then obtained, and Maxwell's equations are solved for the local radiative intensity. Because the effective medium approximations require the use of effective properties obtained

by volumetric averaging, they do not allow for coherent interference effects, and are not expected to predict photon localization and field enhancement.

In this chapter, we will discuss how to use the unique photon transport properties of nanopowders to enhance E_{pump}, the total pumping energy inside the medium. Shown in Fig. 5.1 are different regimes of photon scattering in nanopowders [8]. When the photon mean free path l_m is much larger than the laser wavelength, photons may experience a single scattering event and the transport is diffusive [84]. As l_m decreases, photons begin to undergo multiple scattering events. When l_m is comparable to or smaller than the laser wavelength, recurrent scattering takes place, i.e., photons return to the original place after being scattered many times. In this case, photons don't propagate through the medium, but are confined in a small spatial region, forming a cavity. This phenomenon, termed photon localization, is the counterpart of the electron localization suggested by Anderson [85]. The electromagnetic field of the localized light, as shown in Figure 5.1(d), can be orders of magnitude higher than the incident field [115]. Note that the onset of photon localization is generally questionable when the medium becomes dissipative, since one cannot distinguish whether the attenuation of intensity is caused by strong scattering or by strong absorption. However, for doped nanopowders considered in this analysis, the medium is only slightly dissipative (a very low absorption coefficient). As such, the medium is mainly a strongly scattering medium rather than an absorbing medium, and the attenuation of intensity is dominated by photon localization [115]. This has been confirmed in many random laser experiments on ion-doped powder media [116, 117]. As a result of the photon localization, the photon absorption can be enhanced considerably, due to

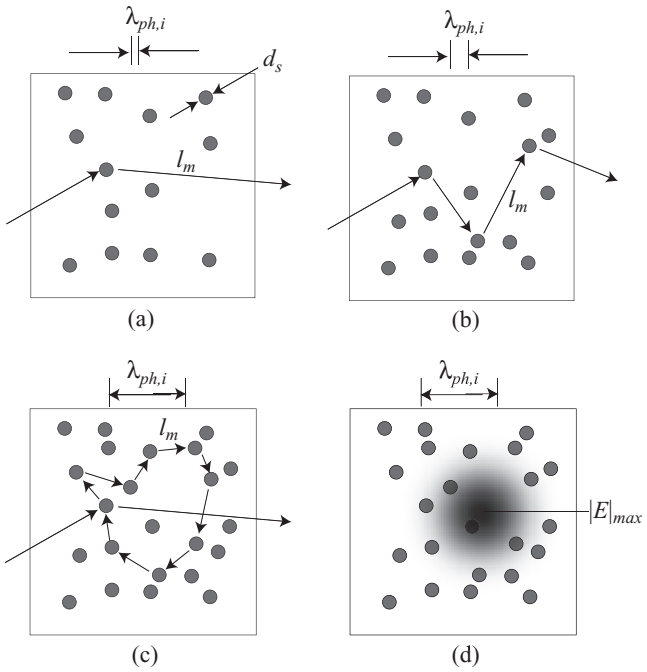

Figure 5.1: (a) Single, (b) multiple, and (c) recurrent photon scattering trajectories in a system of random scatterers, and (d) a rendering of the electromagnetic field distribution for case (c), i.e., as photon localization takes place [8].

this high photon density (or alternatively, electromagnetic field energy density $e_{ph,i}$).

5.2 Photon localization

Absorption occurs when the incident field couples to the dipole moment of the atom. This atom-field interaction is strongest as the incident light is tuned on the resonance of the electronic transition, which is the case in this analysis. Generally the index of extinction is used to describe the absorbing ability of a material. To treat the absorption as a volumetric behavior, the local field amplitude needs to be determined first.

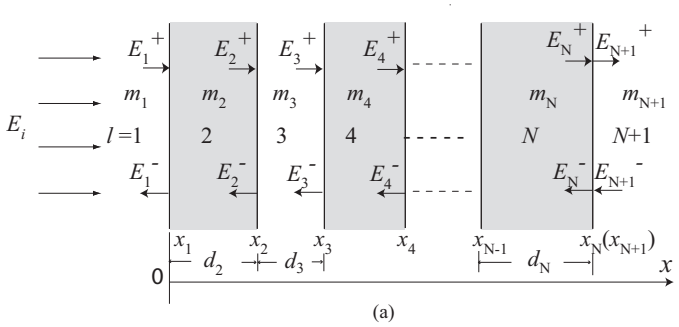

Figure 5.2: Model random nanoparticles, consisting of parallel solid and fluid layers with random thicknesses. The porosity is prescribed.

The simplest model of random nanoparticles consists of parallel solid layers with random thickness, as shown in Fig. 5.2. Regions $l = 1$ and $N + 1$ are semi-infinite media of air. This multilayer medium has $N/2$ (N is an even number here) solid layers and $N/2 - 1$ air layers. The coordinates $x_1, x_2, ..., x_N$ are chosen such that the thickness of each layer is random, but obeys a trapezoidal distribution. This multilayer medium has a finite dimension in the direction of the electromagnetic wave propagation x, and an infinite length in the plane normal to x. The dielectric solid material has a complex refractive index $m_{s,\omega}(= n_{s,\omega} + i\kappa_{s,\omega})$ which depends on the electromagnetic wave frequency. In this section, all the quantities and parameters are at the incident angular frequency ω_0, and thus the subscript ω_0 is omitted for convenience. The air has a refractive index $m_f(= n_f = 1)$.

The general theory starts with Helmholtz's equation

$$\frac{\partial^2 E(x)}{\partial x^2} + k_o^2 m_l^2 E(x) = 0, \tag{5.1}$$

where k_o is the vacuum wave vector, and m is the local complex index of refraction at the incident frequency. This is the electromagnetic wave equation in a source-free

medium, and is equivalent to Maxwell's equations in the multilayer system. For the medium shown in Fig. 5.2, the solution of Eq. (5.1) at a particular location x in the l-th layer is given by

$$E(x) = E_l^+ e^{ik_l(x-x_l)} + E_l^- e^{-ik_l(x-x_l)},\ l = 1, 2, ..., N+1, \tag{5.2}$$

where x_{N+1} takes the value of x_N, since there are only N interfaces and $k_l = m_l\omega_0/c_o$ is the wave vector, where c_o is the speed of light in vacuum. The field in the medium is divided into two components, the forward (transmitted) component E_l^+ and the backward (reflected) component E_l^-. The boundary conditions require that the tangential electric and magnetic fields be continuous across each interface. The relationship between the amplitudes of the l-th and $(l+1)$-th interfaces are given in the matrix form [118]

$$\begin{pmatrix} E_l^+ \\ E_l^- \end{pmatrix} = D_l^{-1} D_{l+1} P_{l+1} \begin{pmatrix} E_{l+1}^+ \\ E_{l+1}^- \end{pmatrix},\ l = 1, 2, ..., N, \tag{5.3}$$

where

$$D_l = \begin{pmatrix} 1 & 1 \\ m_l & -m_l \end{pmatrix},\ l = 1, 2, ..., N+1, \tag{5.4}$$

and D_l^{-1} is the inverse of D_l, and

$$P_l = \begin{pmatrix} e^{-ik_l(x_l - x_{l-1})} & 0 \\ 0 & e^{ik_l(x_l - x_{l-1})} \end{pmatrix},\ l = 2, 3, ..., N+1. \tag{5.5}$$

Hence

$$\begin{pmatrix} E_j^+ \\ E_j^- \end{pmatrix} = \begin{pmatrix} M_{11}^{(j)} & M_{12}^{(j)} \\ M_{21}^{(j)} & M_{22}^{(j)} \end{pmatrix} \begin{pmatrix} E_{N+1}^+ \\ E_{N+1}^- \end{pmatrix},\ j = 1, 2, ..., N, \tag{5.6}$$

where

$$\begin{pmatrix} M_{11}^{(j)} & M_{12}^{(j)} \\ M_{21}^{(j)} & M_{22}^{(j)} \end{pmatrix} = \prod_{l=j}^{N} D_l^{-1} D_{l+1} P_{l+1}, \ j = 1, 2, ..., N. \tag{5.7}$$

For a wave incident from medium 1, we have $E_{N+1}^{-} = 0$. Therefore,

$$\frac{E_j^+}{E_1^+} = \frac{M_{11}^{(j)}}{M_{11}^{(1)}} \tag{5.8}$$

and

$$\frac{E_j^-}{E_1^+} = \frac{M_{21}^{(j)}}{M_{11}^{(1)}}. \tag{5.9}$$

The use of Eqs. (5.8) and (5.9) in Eq. (5.2) yields the field everywhere. The magnetic field is given by [119]

$$\mathbf{H}(x) = \frac{1}{i\omega_0 \mu} \nabla \times \mathbf{E}(x), \tag{5.10}$$

where μ is the magnetic permeability.

The transmissivity is given by

$$T = \frac{|E_{N+1}^-|^2}{|E_i|^2}. \tag{5.11}$$

We calculated the transmissivity for a model multilayer with 50 layers in which the layer thicknesses d_s follows a uniform distribution between $\langle d_s \rangle \pm d_s = 1000 \pm 800$ nm, and with the porosity $\epsilon = 0.35$, $n_s = 1.8$ and $\kappa_s = 0$ (n_s and κ_s are for doped yttria compacts off resonance [111]). To generate such a multilayer, we have infinite number of possibilities, each of which is called a "realization". The non-absorbing material is used to remove the possibility of causing exponential decay by absorption. To investigate the transmissivity as a function of the sample thickness, we add one layer to the sample at one time and thus obtain a series of transmissivities. The dots

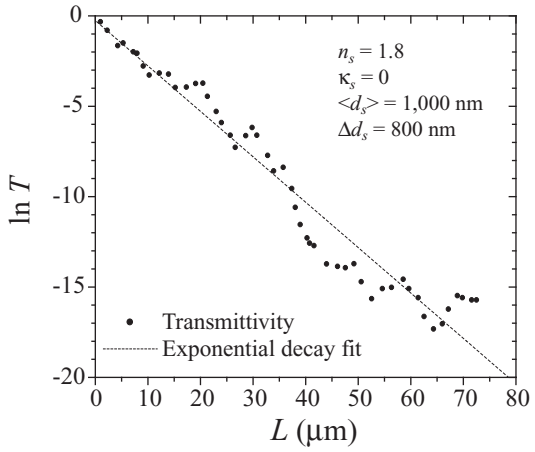

Figure 5.3: Variation of the transmissivity as a function of the medium thickness. The dots are the transmissivities obtained by adding layers to the medium, one at a time, and the dashed line is an exponential decay fit.

shown in Fig. 5.3 represent these transmissivities for one typical realization when there are 1, 2, ..., 50 layers. These dots are fitted well using an exponential decay line, indicating that localization is onset. The localization length of this realization can be obtained from the slope of the fitted line,

$$l_{loc} = -\frac{\mathrm{d}L}{\mathrm{d}(\ln T)}. \tag{5.12}$$

There are infinite possible realizations for this model multilayer, and localization behavior is observed in all realizations that we have tried. This supports the statement that random systems in one-dimensional always exhibit localization [86]. The localization length of this model multilayer is obtained by averaging the localization lengths of numerous realizations.

The effects of the refractive index contrast and the degree of randomness on localization length are investigated, and the results are shown in Fig. 5.4. As expected,

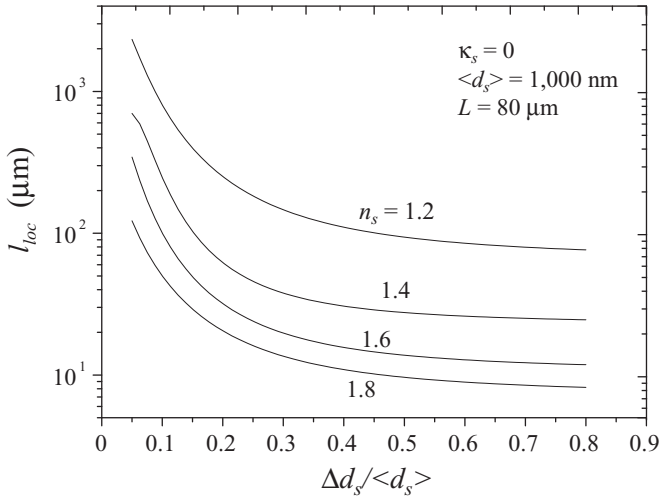

Figure 5.4: Effects of the refractive index contrast and the degree of randomness, on the localization length.

higher refractive index contrast and higher degree of randomness lead to smaller localization lengths, or, stronger localization.

5.3 Field enhancement

The results in the previous section have confirmed the occurrence of photon localization. But what causes localization remained unclear for some time. Now it is commonly believed to be due to the constructive interference among the multiply scattered waves. However, the transmissivity profile in Fig. 5.3 does not show any explicit signature of interference. Recently, the local field amplitude, rather than the transmissivity, was investigated for random multilayer, and strong field enhancement was observed [111]. This provides an exact signature of strong, constructive wave interference.

5.3.1 One-dimensional multilayer

The local electric field is determined in a model multilayer with 50 layers, and subject to a same irradiation as in the previous section. There are infinite possible realizations for this model multilayer, and the field results for one of them are shown in Fig. 5.5(a), where the dimensionless electric field is defined as, $|E|^* = |E|/|E_i|$.

From Fig. 5.5(a), it is evident that there is field enhancement, i.e., there are peaks in the field inside the medium that can be a few orders of magnitude larger than the incident field, for this realization. Thus, the energy density of the electric field can be two or even more orders of magnitude larger than the incident value. In periodic multilayer, the electric field is also periodic, resulting in no isolated peaks inside the media (even if the field in this case can also be higher than the incident field). The physical basis of field enhancement is electromagnetic wave interference. In the random multilayer system, the waves will multiply transmit and reflect at all interfaces, and interfere with each other. At some sites for some realizations, the interference is so ideally constructive that it results in an extremely large field. Thus the large field enhancement is directly attributed to randomness, and cannot be observed in homogeneous or periodic media. Note that the coherence condition that the medium size is smaller than the coherence length must be satisfied to observe the field enhancement. The coherence length is $\lambda^2/\Delta\lambda$ for a central wavelength λ and a spectrum width $\Delta\lambda$ [120]. In this study we assume a monochromatic wave, thus satisfying the coherence condition ($\Delta\lambda$ is 0 and the coherence length is infinite). The coherence length of many lasers is several kilometers, satisfying the coherence

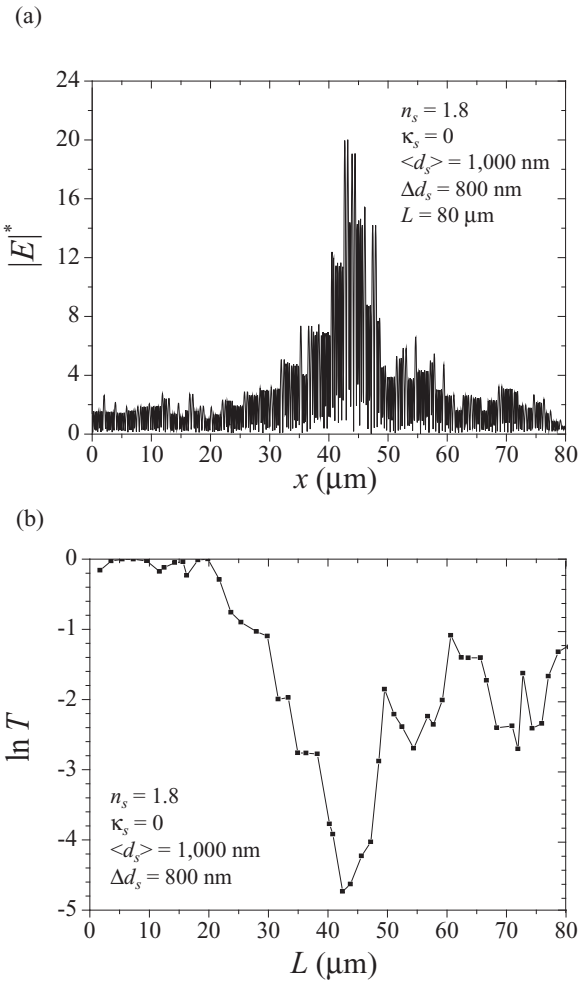

Figure 5.5: (a) Local field distribution in a random multilayer, with field enhancement shown. (b) Variation of the transmissivity as a function of the medium thickness, in the same multilayer.

condition. It's interesting to see how the transmissivity evolves layer by layer in such a realization that allows for field enhancement. This is shown in Fig. 5.5(b). Different from the case in Fig. 5.3, in which the transmissivity reveals a good exponential decay behavior, the variation of transmissivity with sample thickness in Fig. 5.5(b) has a large fluctuation, but localization is still considered to happen, since diffusion obviously breaks down. It is anti-intuitional that just after field enhancement is onset, there is a region in which the transmissivity increases, rather than decreases, with the sample thickness. Also, the final transmissivity is much larger than that in Fig. 5.3. However, this is straightforward if one recognizes that more photons have to travel through and interfere with each other to establish a large local field. Although realizations allowing field enhancement generally have larger transmissivity, the field is more trapped in a wavelength sized region, forming a "random resonator". This property is very attractive to laser science since it may replace the resonator in conventional lasers. Experimentally, laser actions in random gain media have been observed [61].

5.3.2 Two-dimensional geometry

The two-dimensional random porous medium used in this study is shown sketchily in Fig. 5.6(a). The solids are arranged as an array of infinitely long (in the y direction) dielectric cylinders with random radii and locations. We again examine the wave propagation subject to incidence of a planar electromagnetic wave upon this structure, traveling in the x-direction. Maxwell's equations in two-dimensional random media

have been solved using FDTD or the transfer matrix method [92, 93], but the degree of randomness has been limited by the mesh size, and thus the media could not be systematically randomized. In this study, the cylinder radii and locations are entirely random (the only limitation is that the cylinders should not overlap). A code which is based on the finite element method, High Frequency Structure Simulator (HFSS), is used []. A finite computation domain is chosen, resulting in six surfaces or boundaries. The two x-z boundaries are taken as being periodic to simulate the infinite length in the y direction. The two x-y boundaries are also taken as being periodic. The y-z planes are set to be the incident boundary at $x = 0$ and the radiation boundary at $x = L$.

We choose a computation domain of $5 \times 1 \times 5$ μm^3. Again, the local electric field in this region is determined for a normal incident electromagnetic wave of wavelength $\lambda = 1000$ nm, for a two-dimensional random medium composed of 20 long cylinders with a random diameter $\langle d_s \rangle \pm \Delta d_s = 1000 \pm 400$ nm, and with $n_s = 1.8$ and $\kappa_s = 0$ in air. The results are shown in Fig. 5.6(b), using contours of constant dimensionless electric field. Similar to the one-dimensional case, there are sites of field enhancement within the random porous medium that can be a few orders higher of magnitude than the incident field.

5.3.3 Factors that influence occurrence of field enhancement

The electric field distributions described above are examples of individual realizations with large field enhancements. Determining the structural characteristics

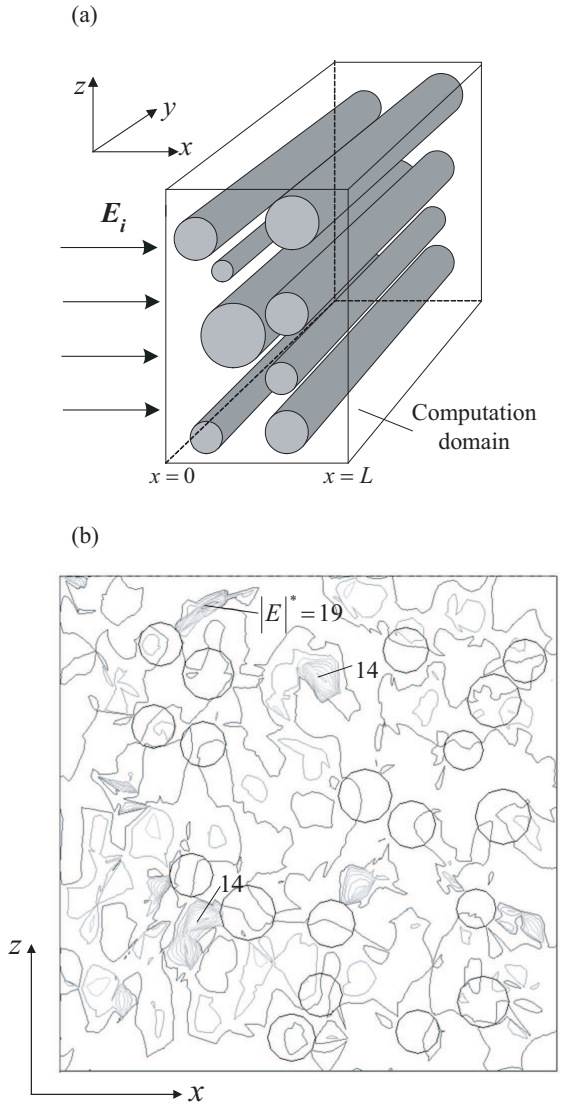

Figure 5.6: (a) The two-dimensional geometry composed of infinitely long cylinders. (b) The two-dimensional distribution of the dimensionless field magnitude $|E|^*$ for a realization, the circles are the sections of the cylinders. The porosity is 0.85.

related to the maximum field enhancement is not attempted. However, statistical averaging over numerous realizations can help in understanding the conditions under which large field enhancements are more probable. For the one-dimensional multi-layer, we compute $N_t = 19,200,000$ local-field values $|E|^*$, from $N_r = 6,000$ different realizations, each of which gives $N_n = 3,200$ field values. From these, we compute the probability density function $f(|E|^*)$. This is found by first dividing all of the field values (from 0 to $|E|^*_{max}$) into a number of (say N_b) bins (intervals), and then determining the number of field values in each bin. Finally the probability density f_i for the i-th bin is found from

$$f_i = \frac{M_i}{N_t W_b} = \frac{M_i N_b}{N_t |E|^*_{max}}, \tag{5.13}$$

where M_i is the number of occurrences in the i-th bin and $W_b = |E|^*_{max}/N_b$ is the bin width. In our 6,000 realizations, $|E|^*_{max}$ is 20.1.

The results are shown in Figs. 5.7(a) to (d), for several values of the refractive index (n_s, κ_s), average layer size ($\langle d_s \rangle / \lambda$), and the degree of randomness ($\Delta d_s / \langle d_s \rangle$). As shown in Figs. 5.7(a), (b) and (d), the higher the values of n_s, κ_s and $\Delta d_s / \langle d_s \rangle$, the higher the probability of an occurrence of small $|E|^*$, i.e., there is less probability for field enhancement ($|E|^* > 1$). At the same time, as indicated in Figs. 5.7(a) and (d), the higher the values of n_s and $\Delta d_s / \langle d_s \rangle$, the higher the probability of occurrence of large field enhancement. As shown in Fig. 5.7(c), the average size parameter does not affect the field significantly. It should be noted that $|E|^*_{max}$ is not shown here because of its extremely small probability.

The locations of the field enhancement are determined using the same samplings

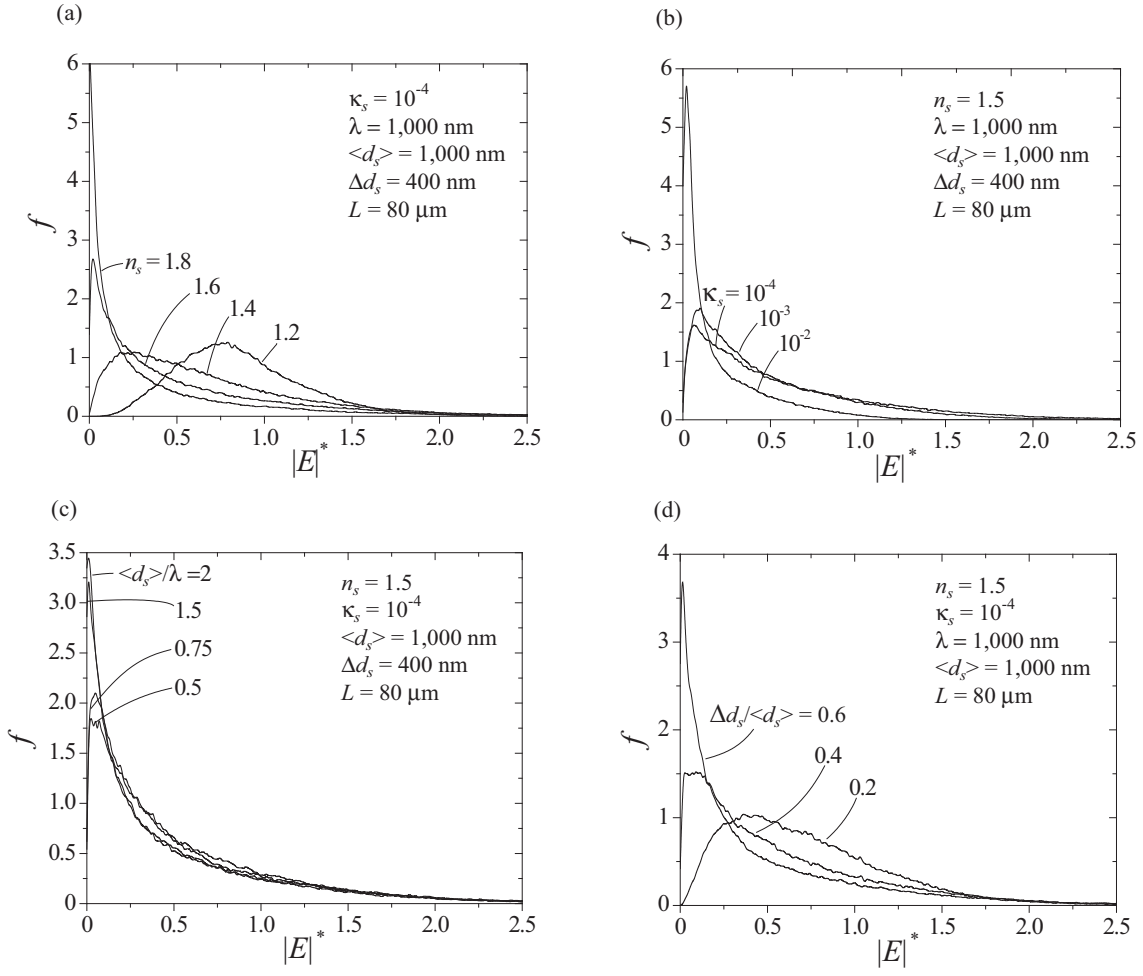

Figure 5.7: Probability density function for $|E|^*$ within a random porous medium, showing the effects of solid (a) refractive index, (b) extinction index, (c) size parameter, and (d) size distribution. The porosity is 0.35.

mentioned above, i.e., the $N_r = 6,000$ realizations, each of which gives $N_n = 3,200$ field values at the same set of 3,200 sampling locations. Then for each location x, there are N_r different field values $|E|^*$, some of which (say N_e) are enhanced ($|E|^* > 1$). The probability $p(x)$ of having field enhancement ($|E|^* > 1$) at a site x is found by dividing the number of the occurrences of field enhancement N_e by N_r. This probability is plotted for each of the 3,200 sites, as shown in Fig. 5.8. The field at sites closer to the incident surface is always more probable to be enhanced. Also, the higher the values of n_s, κ_s, $\langle d_s \rangle / \lambda$ and $\Delta d_s / \langle d_s \rangle$, the less is the probability of field enhancement.

5.4 Absorption enhancement in dissipative media

Non-absorbing medium is used to investigate localization in Section 5.2 to show that the exponential decay of transmissivity is caused indeed by recurrent scattering, rather than absorption. However, real media always have some absorption. It has been shown that photon localization still happens in weakly dissipative media [86]. In this section, our interest is put on the local absorption and heat generation in the medium. Again consider the multilayer in Fig. 5.2, the local intensity is given by the time average of the Poynting vector $\mathbf{S}$ as

$$I(x) = |\overline{\mathbf{S}}(x)| = \frac{1}{2}|\mathrm{Re}[\mathbf{E}(x) \times \mathbf{H}^*(x)]|. \tag{5.14}$$

where $\mathbf{H}(x)$ is the magnetic field. According to the energy conservation law, the power loss per unit volume (or the volumetric heat generation rate) is defined by the

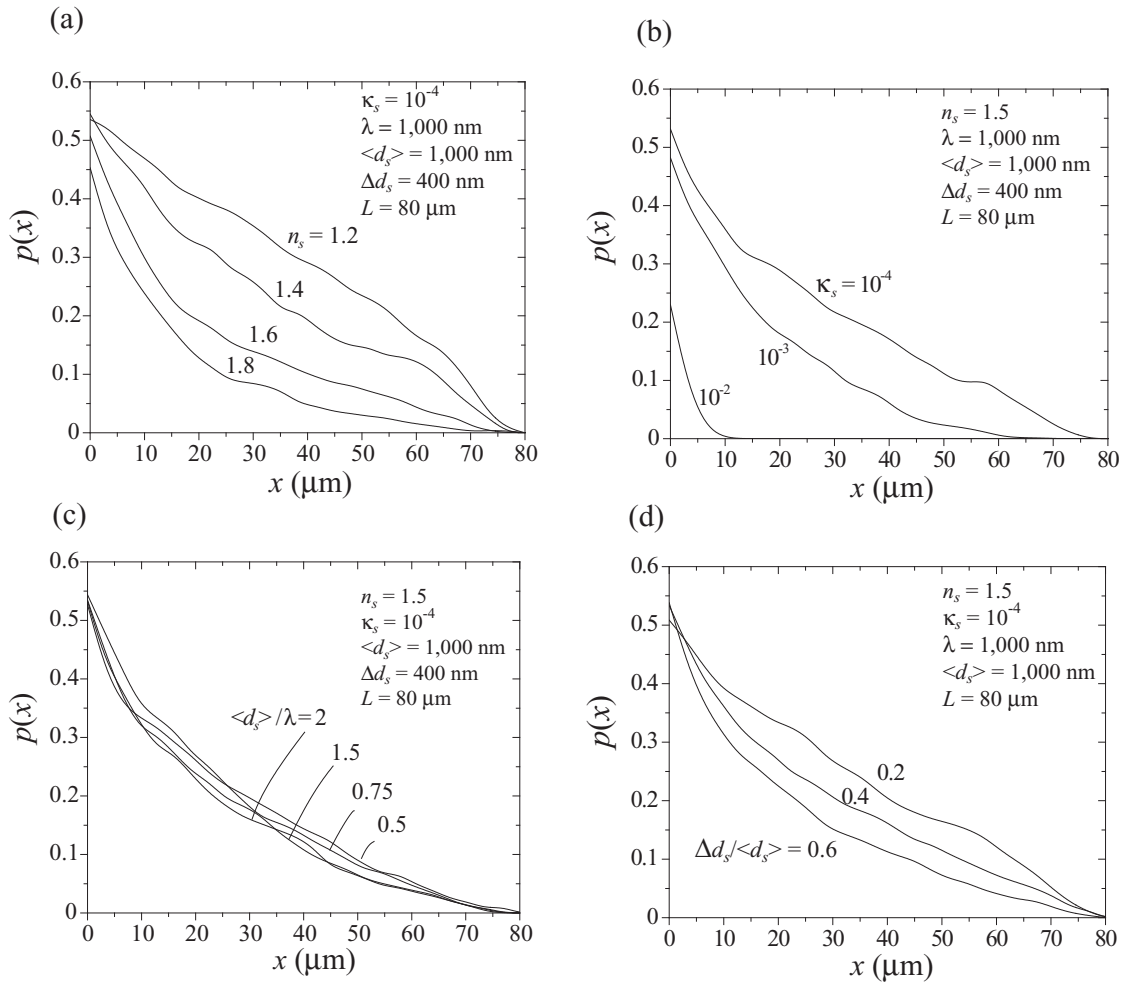

Figure 5.8: Probability of field enhancement as a function of locations. Effects of solid (a) refraction index, (b) extinction index, (c) size parameter, and (d) size distribution. The porosity is 0.35.

spatially decay rate of the intensity

$$\dot{s} = -\frac{\mathrm{d}I}{\mathrm{d}x}, \tag{5.15}$$

and the extinction coefficient σ_{ex} is defined as the ratio of heat generation rate $\dot{s}$ to the local intensity I

$$\sigma_{ex} = \frac{\dot{s}}{I} = -\frac{1}{I}\frac{\mathrm{d}I}{\mathrm{d}x}. \tag{5.16}$$

From electromagnetic wave theory, the power loss per unit volume for this lossy dielectric medium is [121]

$$\dot{s} = \frac{1}{2}\sigma|E|^2 = \frac{1}{2}\omega\epsilon''|E|^2, \tag{5.17}$$

where σ is the electric conductivity, ω is the angular frequency, and ϵ'' is the imaginary part of the dielectric constant ϵ, which is related to the complex refractive index m through

$$\epsilon = \epsilon' - i\epsilon'' = \epsilon_o m^2, \tag{5.18}$$

where ϵ_o is the free-space permittivity. Then Eq. 5.17 becomes:

$$\dot{s}_0(x) = \frac{2\pi n_l \kappa_l}{\lambda}\left(\frac{\epsilon_o}{\mu_o}\right)^{\frac{1}{2}}|E(x)|^2, \tag{5.19}$$

where μ_o are the free space permeability. Eq. (5.15) and (5.19) give the same result, while Eq. (5.19) shows that $\dot{s}$ is explicitly proportional to the square of the electric field.

The local electric field is again determined subject to a normal incident electromagnetic wave of wavelength $\lambda = 1,000$ nm, in a one-dimensional random multilayer with 50 solid layers whose thicknesses d_s follows a uniform distribution between

$\langle d_s \rangle \pm \Delta d_s = 1000 \pm 800$ nm, and with the porosity $\varepsilon = 0.35$, $n_s = 1.8$ and $\kappa_s = 10^{-5}$ (n_s and κ_s are for doped yttria compacts on resonance [111]). There are infinite possible realizations for this model composite, and the field results for one of them are shown in Figs. 5.9(a) to (d), where the dimensionless parameters are defined as, $|E|^* = |E|/|E_i|$, $I^* = I/I_i$ and $\dot{s}^* = s\langle d_s \rangle / I_i$.

From Fig. 5.9(a), it is evident that field enhancement is still possible in weakly absorbing multilayer system, suggesting that scattering is dominant over absorption. The distribution of the intensity, which decays with a random rate, is shown in Fig. 5.9(b). As shown in Fig. 5.9(c), the volumetric heat generation rate due to absorption has a similar distribution as that of the electric field, because $\dot{s}$ is proportional to the square of the field, according to Eq. (5.19). The peak of $\dot{s}$ inside the medium indicates that a local melting may happen at that site. The distribution of the local extinction coefficient σ_{ex} is presented in Fig. 5.9(d). The maximum of σ_{ex} does not necessarily coincide with the maximum of $\dot{s}$, because σ_{ex} is the ratio of $\dot{s}$ and the local intensity.

The pumping energy E_{pump} inside the nanopowder medium is then calculated using Eq. (3.23), and compared to that for the bulk crystal with the same apparent volume (note however that the volume of the solid phase for nanopowder is smaller than that for the bulk crystal), as shown in Fig. 5.10. Note also that for a model composite given the porosity ε and the particle size distribution, there are an infinite number of realizations, and hence, the ensemble average of a sufficient number of realizations is taken in calculations, and used for that model composite. The ratio of the total pumping energy, with respect to porosity ε for different particle mean diameter $\langle d_s \rangle$, is shown in Fig. 5.10. For high porosities, the ratio may be as large

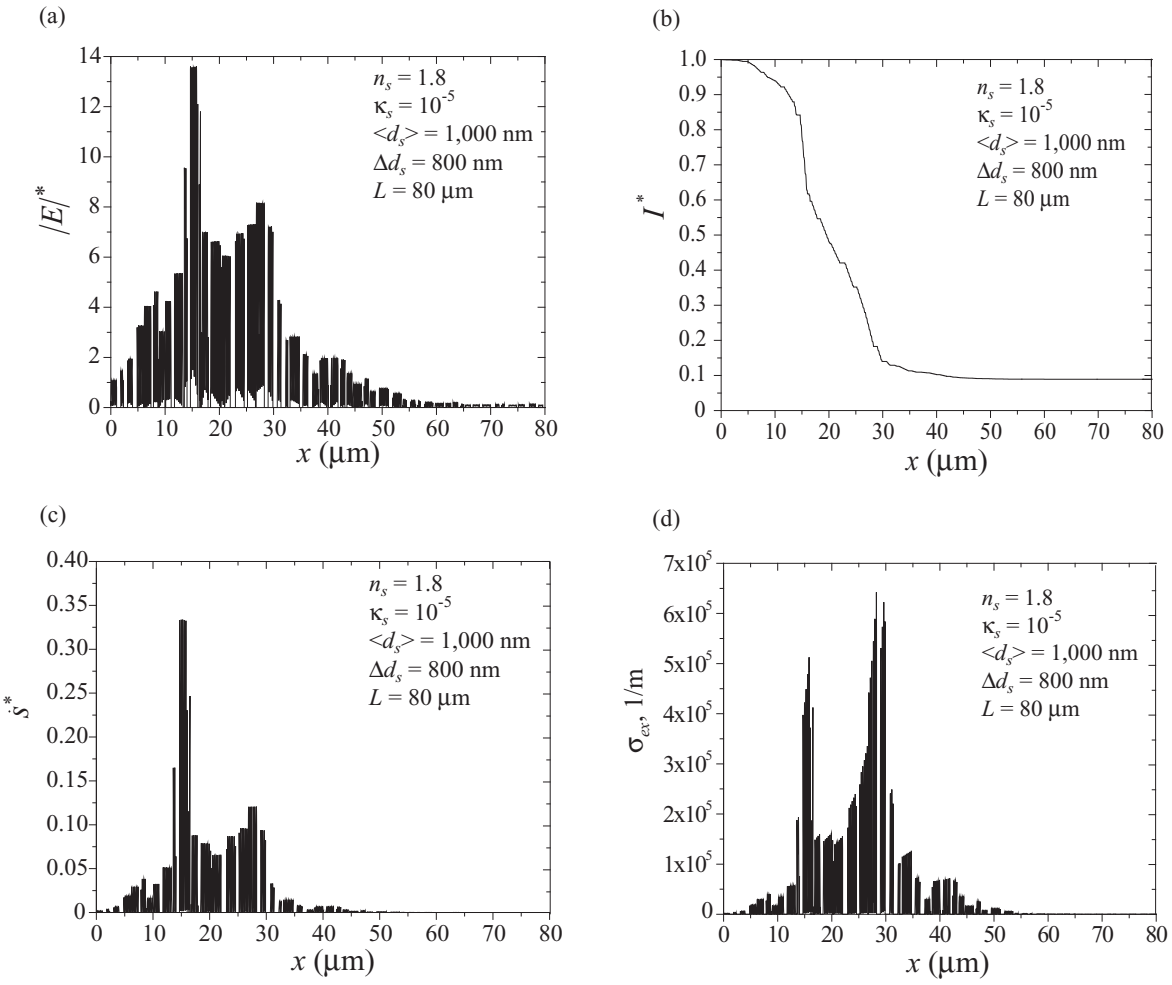

Figure 5.9: Distributions of the dimensionless (a) electric field, (b) intensity, (c) volumetric heat generation rate, and (d) extinction coefficient, for a weakly absorbing multilayer. The porosity is 0.35.

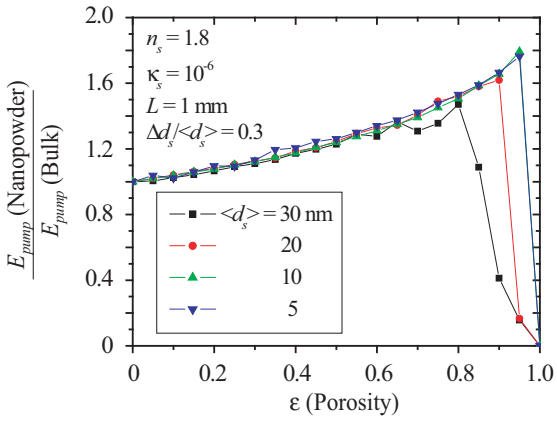

Figure 5.10: Variation of the scaled pumping energy inside the medium (nanopowder to the bulk crystal), with respect to porosity. The total pumping energy of nanopowder can be enhanced by 50%-70%, at high porosities.

as 1.5 to 1.7, indicating an enhancement of the total pumping energy E_{pump} by 50% to 70%. Fig. 5.10 also provide the guidelines for the optimum porosity and mean particle size.

It should be noted that the multiple scattering can also enhance the fluorescence reabsorption, which is a negative side effect. The 50% enhancement in the total pumping energy implies that the incident photons travel a 50% longer pathlength due to the multiple scattering, and it is reasonable to assume that L_{ave}, the average distance that a photon travels to escape from the medium, is also enhanced by 50% compared to that of the bulk. Then the escape efficiency η_e becomes

$$\eta_e = \exp(-\sigma_{ph,r} L_{ave}) = 0.993. \tag{5.20}$$

This is very close to 0.995 for the bulk medium. Also, if the intrinsic quantum

efficiency η_{e-ph} is 0.99, then the external quantum efficiency becomes

$$\tilde{\eta}_{e-ph} = 0.98993. \tag{5.21}$$

This is almost the same as that (0.98995) for the bulk medium. Therefore, the reabsorption effect of photon localization in nanopowder medium can be neglected.

5.5 Electromagnetic statistical (EMS) approach

For a nanopowder medium, if the particle average size and porosity, and the spread in the particle size are given, an infinite realizations of one-dimensional random multilayer (and associated filed distributions) are possible. The probability for occurrence of a given realization is rather low, but the statistical average of the intensity distributions of a sufficient number of realizations represents the intensity expectation distribution in the medium reasonably. This approach, here called the electromagnetic statistical (EMS) approach, is explained in Fig. 5.11. A model multilayer with 250 layers is considered, and 6,000 realizations are used. Note that we use a longer sample than before, in order to show more effectively the variation of local intensity with location. For each realization, we calculate the local intensity using the same method developed in the previous section, and record the intensity values at 3,200 sampling sites. Then for each of the 3,200 sites, we determine its expectation intensity by averaging the field values of that site of 6,000 realizations. To be clearer, the results of only two (compared to 3,200) typical realizations, each of which is calculated similarly with the intensity distribution in Fig. 8(b), are shown in Fig. 5.11. The results are presented in Fig. 5.12, for weakly and strongly absorbing materials,

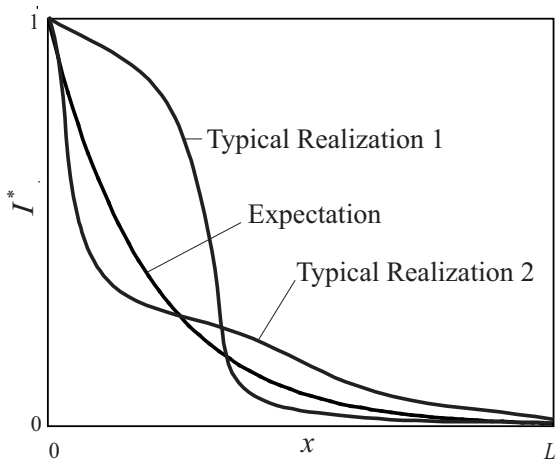

Figure 5.11: Distributions of the dimensionless (a) electric field, (b) intensity, (c) volumetric heat generation rate, and (d) extinction coefficient, for a weakly absorbing multilayer. The porosity is 0.35.

respectively. The expectation intensities decay exponentially in the direction of wave propagation.

5.6 Predictions of equation of radiative transfer (ERT)

5.6.1 Formulation and solution procedure

The radiation transport within the same composite described in previous sections can also be treated using the ERT. In this treatment, the scattering properties of a single particle are derived first, using small and large particle size approximations. The effective scattering properties are then determined for a cluster of particles, based on the porosity and particle size distribution. Finally the ERT is solved using proper

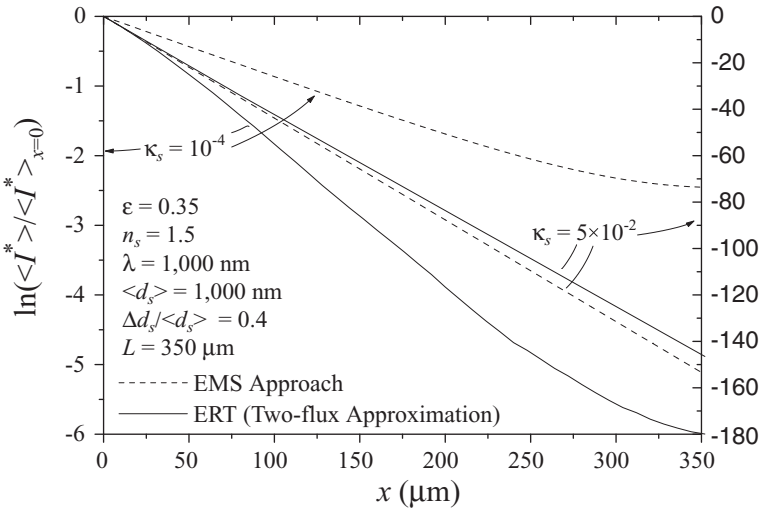

Figure 5.12: Comparison of the intensity distributions obtained by the EMS and ERT, for a one-dimensional multilayer porous medium, as $\kappa_s = 10^{-4}$ and $\kappa_s = 5 \times 10^{-2}$, respectively.

approximations, such as the two-flux model.

For a one-dimensional multilayer system, a layer serves as a single scatterer. For the normal incidence of a planar radiation upon a planar particle, as shown in Fig. 5.13, the scattering is by reflection. Using the transfer matrix method, the incident, transmitted and reflected fields are related through

$$\begin{pmatrix} E_i \\ E_r \end{pmatrix} = D_1^{-1} D_2 P_2 D_2^{-1} D_3 \begin{pmatrix} E_t \\ 0 \end{pmatrix} \tag{5.22}$$

Thus, E_r and E_t are derived in terms of E_i, and the transmission coefficient is a function of the layer thickness d_s, for a given m_f and m_s, i.e.,

$$T_r(d_s) = \frac{I_t}{I_i} = \frac{|E_t|^2}{|E_i|^2} \tag{5.23}$$

The extinction coefficient of the single particle is defined as

$$\sigma_{ex}(d_s) = \frac{-\ln T_r(d_s)}{d_s}. \tag{5.24}$$

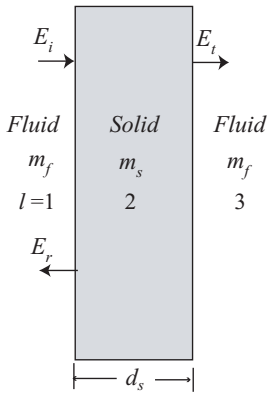

Figure 5.13: Transmission and reflection in a single solid layer.

For a random multilayer medium with porosity ε, where the layer thickness d_s follows a uniform distribution in the range of $\langle d_s \rangle \pm \Delta d_s$, the effective extinction coefficient becomes

$$\langle \sigma_{ex} \rangle = \frac{\int_{\langle d_s \rangle - \Delta d_s}^{\langle d_s \rangle + \Delta d_s} -\ln T_r(d_s) \mathrm{d}d_s}{\int_{\langle d_s \rangle - \Delta d_s}^{\langle d_s \rangle + \Delta d_s} d_s \mathrm{d}d_s} (1 - \varepsilon). \tag{5.25}$$

The effective absorption coefficient is

$$\langle \sigma_a \rangle = \frac{4\pi\kappa_s}{\lambda_0}(1 - \varepsilon). \tag{5.26}$$

The effective scattering coefficient is found from

$$\langle \sigma_s \rangle = \langle \sigma_{ex} \rangle - \langle \sigma_a \rangle. \tag{5.27}$$

Since scattering occurs only in the backward direction, the scattering phase function is a delta function, i.e.,

$$\Phi(\theta) = \delta(\theta - \pi), \ \int_{-1}^{1} \Phi(\theta) \mathrm{d}\cos\theta = 2. \tag{5.28}$$

Then the ERT becomes []

$$\cos\theta \frac{\mathrm{d}I(x,\theta)}{\mathrm{d}x} = -(\langle \sigma_s \rangle + \langle \sigma_a \rangle) I(x,\theta) + \frac{\langle \sigma_s \rangle}{2} \left[\int_0^1 I(x,\theta_i) \Phi(\theta_i - \theta) \mathrm{d}\cos\theta_i + \int_0^1 I(x,\theta_i) \Phi(\theta_i - \theta) \mathrm{d}\,\mathrm{co} \right.$$

For a normal irradiation on a one-dimensional geometry, the radiative intensity has only two components, namely, forward and backward. Thus the two-flux approximation can be used to solve Eq. 5.29. By taking $\theta = 0$, and defining $I(x, 0) = I^+$, and $I(x, \pi) = I^-$, Eq. 5.29 gives for the forward intensity

$$\frac{\mathrm{d}I^+}{\mathrm{d}x} = -(\langle\sigma_s\rangle + \langle\sigma_a\rangle)I^+ + \langle\sigma_s\rangle[(1-B)I^+ + BI^-], \tag{5.30}$$

where

$$B = \frac{1}{2}\int_{-1}^{0} \Phi(\theta_i)\mathrm{d}\cos\theta_i = 1. \tag{5.31}$$

Equation 5.30 can then be simplified to

$$\frac{\mathrm{d}I^+}{\mathrm{d}x} = -(\langle\sigma_s\rangle + \langle\sigma_a\rangle)I^+ + \langle\sigma_s\rangle I^-. \tag{5.32}$$

Similarly, by taking $\theta = \pi$, Eq. 5.29 gives for the backward intensity

$$-\frac{\mathrm{d}I^-}{\mathrm{d}x} = -(\langle\sigma_s\rangle + \langle\sigma_a\rangle)I^- + \langle\sigma_s\rangle I^+. \tag{5.33}$$

The boundary conditions for Eqs. 5.32 and 5.33 are

$$I^+(0) = 1,\ I^-(L) = 0. \tag{5.34}$$

5.6.2 Photon diffusion in non-absorbing random media

Being an effective medium, particle-based transport equation, we expect ERT not to be capable of predicting photon localization, this is shown here. Again, a non-absorbing medium is used to remove the possibility of causing exponential decay by absorption. Equations 5.32 and 5.33 are thus simplified to

$$\begin{cases} \frac{\mathrm{d}I^+}{\mathrm{d}x} = -\langle\sigma_s\rangle I^+ + \langle\sigma_s\rangle I^- \\ -\frac{\mathrm{d}I^+}{\mathrm{d}x} = -\langle\sigma_s\rangle I^- + \langle\sigma_s\rangle I^+ \end{cases} \tag{5.35}$$

The solution subject to boundary conditions given by Eq. 5.34, is

$$\begin{cases} I^+(x) = \frac{1+\langle\sigma_s\rangle(L-x)}{1+\langle\sigma_s\rangle L} \\ I^-(x) = \frac{\langle\sigma_s\rangle(L-x)}{1+\langle\sigma_s\rangle L} \end{cases} \tag{5.36}$$

Then the transmissivity is found from

$$T(L) = I^+(L) = \frac{1}{1+\langle\sigma_s\rangle L}. \tag{5.37}$$

In random porous media, $\langle\sigma_s\rangle L$ is generally much larger than 1, and $T(L)$ has an inverse dependence on it, i.e., $T(L) = 1/[\langle\sigma_s\rangle L]$, which is characteristic of classical diffusion [99] with a mean free path $l_m = 1/\langle\sigma_s\rangle$. Thus, photon localization cannot be predicted by ERT, since the medium is averaged to obtain the effective scattering and absorption properties, where wave interference effects are not allowed.

5.6.3 Absorption in dissipative random media

For a dissipative medium, the solution of Eqs. (5.32) and (5.33) is

$$I^+(x) = \frac{(1+\beta^2)\sinh[\gamma(L-x)] + 2\beta\cosh[\gamma(L-x)]}{(1+\beta^2)\sinh(\gamma L) + 2\beta\cosh(\gamma L)} \tag{5.38}$$

$$I^-(x) = \frac{(1-\beta^2)\sinh[\gamma(L-x)]}{(1+\beta^2)\sinh(\gamma L) + 2\beta\cosh(\gamma L)} \tag{5.39}$$

where

$$\beta = [\langle\sigma_a\rangle/(\langle\sigma_a\rangle + 2\langle\sigma_s\rangle)]^{1/2} \tag{5.40}$$

and

$$\gamma = [\langle\sigma_a\rangle(\langle\sigma_a\rangle + 2\langle\sigma_s\rangle)]^{1/2} \tag{5.41}$$

The local intensity is the difference between the forward and backward intensities

$$I(x) = I^{+}(x) - I^{-}(x). \tag{5.42}$$

The predicted distributions of the normalized local intensity using ERT are shown in Fig. 5.12, for $\kappa_s = 10^{-4}$ and 5×10^{-2} respectively. The volumetric heat generation rate is

$$\dot{s}(x) = -\frac{\mathrm{d}I(x)}{\mathrm{d}x}. \tag{5.43}$$

5.7 Comparison of ERT, EMS and EM Treatments: Competition between Localization and Absorption

The intensity obtained using ERT are compared with the expectation values from the EMS (discussed in Section 5.5). Both results decay exponentially, but with same or different rates. This is determined by the nature of the two treatments. In the EMS treatment, the first step is to calculate the electric field exactly for each realization, where the detailed geometric features are kept, and wave interference (dependent scattering) is allowed. The second step is to average the intensities among many realizations, where the dependent effect is still retained. In the ERT treatment, the first step is to average the medium to obtain the effective scattering and absorption properties, where the wave interference is not allowed. The second step is to calculate the intensity in this effective medium. Consequently, the results of ERT are for

independent scattering and do not allow for photon localization. To quantitatively analyze this difference between the two treatments, we calculate the localization and absorption length for the two model composites, shown in Fig. 5.12. The localization lengths is calculated in the absence of absorption using the method in Section 5.2, and the absorption length (penetration depth in EM theory) is calculated by $l_a = \lambda_0/[4\pi\kappa_s(1-\varepsilon)]$. For the weakly absorbing solid ($\kappa_s = 10^{-4}$), the localization and absorption lengths are 23.4 μm and 1224.3 μm, respectively, indicating that localization is dominant over absorption. The two treatments differ significantly, since ERT does not allow for predicting localization. As the solid becomes more absorbing, the absorption becomes more important and localization becomes less important, and the two results are closer. For a highly absorbing material ($\kappa_s = 5 \times 10^{-2}$), the localization and absorption lengths are 23.4 μm and 2.4 μm, respectively, indicating that absorption is dominant over localization. The two treatments agree. This result indicates that although in both the ERT and EMS the intensity decays exponentially, the magnitudes do not generally agree, except for highly absorbing media. By introducing corrections to the scattering and absorption coefficients, based on the geometric and optical parameters, ERT may predict results similar to EMS. However, this scaling function must be complicatedly related to many parameters, such as the particle size distribution and the complex refractive index, and is not attempted here.

From the intensity profile (as shown in Fig. 5.12), the extinction coefficients are determined for the EMS and ERT treatments using Eq. (5.16), and are compared to the extinction coefficient for one typical realization obtained using the EM theory. The results are shown in Fig. 5.14. As can be seen, the effective medium approximations

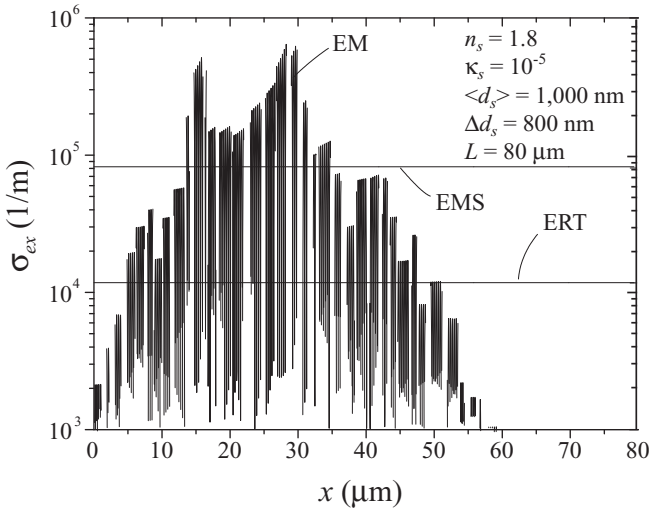

Figure 5.14: Comparison of the extinction coefficients predicted by EM, EMS, and ERT.

(EMS and ERT) give constant extinction coefficients through the medium, while the direct simulation (EM theory) gives spatially dependent extinction coefficients. At some sites, the local extinction coefficients can be up to a few orders higher of magnitude than the average extinction coefficients predicted by the effective medium approximations. Thus, only the direct simulation (EM theory) is capable of predicting the space dependent, enhanced absorption.

5.8 Discussions and summary

Electromagnetic wave interference plays a fundamental role in wave propagation and localization in random porous media. To allow for interference effects, a direct simulation (EM) has been used to solve the Maxwell's equations. Photon localization, rather than the classical diffusion, is observed in a random multilayer. The local field calculations predict field enhancement up to a few orders of magnitude higher

than the incident field. The field enhancement is caused by the ideally constructive interference at some sites for some realizations. The probability of enhanced $|E|^*$ and the locations of this enhancement are influenced by the solid complex refractive index and the particle size distribution. As a result of the spatially dependent, locally enhanced field, the spatially dependent absorption enhancement is also observed. Based on the EM theory, a new effective medium treatment, EMS, offers a reasonable distribution of the expectation intensity because it allows for the interference effects. In comparison, the traditional effective medium approximations (ERT here) require the use of effective properties obtained by volumetric averaging, and do not directly allow for the interference effects. Consequently, they are unable to predict the strong, local field enhancement and photon localization. For high porosities, the pumping energy may be as large as 1.5 to 1.7 times of that for bulk materials, indicating an enhancement of the total pumping energy E_{pump} by 50% to 70%.

Chapter 6

Optimizing the size effect of phonon spectra

6.1 Introduction

To analyze photon-electron-phonon interactions, the phonon DOS needs to be known. In the expression of the cooling power given by Fermi golden rule (Eq. 3.41), the phonon density of states (DOS) is a parameter that can be engineered to achieve optimum cooling performance. In laser cooling experiments, as the frequency is tuned to the red side of the resonance, only phonons with the energy $\omega_{e,g} - \omega_{ph,i}$ can be absorbed, and the absorption probability is dependent on the phonon density of states and the distribution function. The Debye DOS is often assumed for bulk materials [122]. It shows a parabolic distribution which results from an assumption of an isotropic medium with no dispersion, or effects of optical phonons. The phonon DOS of nanostructures may, however, deviates from that for bulk crystals, due to

quantum size effects [123]. Since the phonon density of states is not available for Y_2O_3, it will be calculated and then optimized using size effects.

6.2 Calculation of the phonon density of states

The phonon DOS may be calculated using lattice dynamics calculations or molecular dynamics simulations [124]. In lattice dynamics calculations, the dynamical matrix is diagonalized, and the vibrational eigenvalues and eigenvectors determined. This approach actually calculates the harmonic modes, e.g., at 0 K. In molecular dynamics, the velocity autocorrelation function is calculated for each species and the partial phonon DOS is then obtained by taking the Fourier transforms of this autocorrelation function. The results of these two approaches have been found to agree with one another at low temperatures [124], as expected. However, at high temperature the first method is not suitable since it is harmonic. Also, the direct diagonalization of the dynamical matrix becomes impractical when the system size is more than a few thousand atoms [125, 126]. Therefore, the phonon DOS $D(\omega)$ is calculated using molecular dynamics simulations in this work.

6.3 Structures for bulk crystals and nanopowders

The X-ray diffraction [127] and neutron diffraction [128] experiments have shown that Y_2O_3 has a face-centered cubic structure, which is retained in nanocrystals [129]. Eight metal ions are in the positions $(1/4, 1/4, 1/4)$; the remaining twenty four occupy

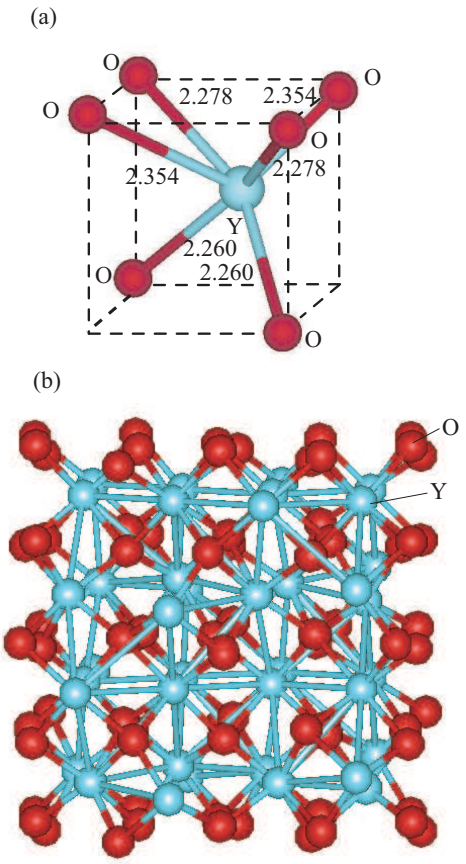

Figure 6.1: Crystal structure of Y_2O_3. (a) The oxygen ions are arranged in distorted octahedra around the Yttrium ions. The listed measured equilibrium bond lengths are in Å. (b) The structure of a cubic unit cell.

the sites $(u, 0, 1/4)$. The forty-eight oxygen ions are in general positions (x, y, z), arranged in distorted octahedra around the metal ions, the metal-oxygen bonding distances being unequal. The values of u, x, y, z are listed in [127, 128]. The crystal structure is shown in Fig. 6.1

The nanopowder is generated by cutting a sphere out of a much larger bulk crystal, as shown in Figure 6.2. Note that the center of the sphere can be randomly selected, we have many possible configurations given the diameter.

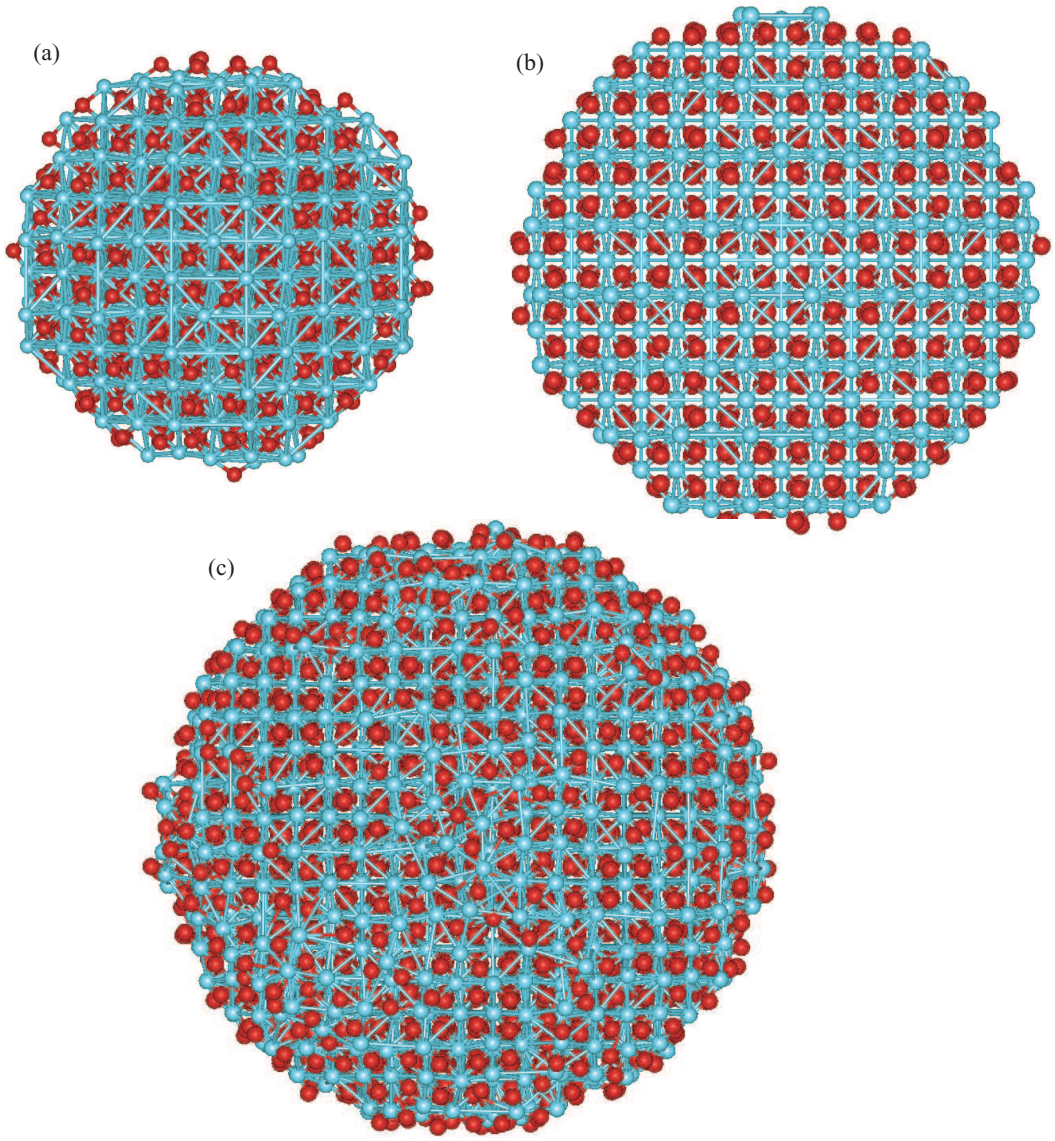

Figure 6.2: The structure of the spherical Y_2O_3 nanoparticle (cluster) used in the molecular dynamics simulations. The boundary is free and the particle structure is relaxed. (a) $d_s = 3$ nm, (b) $d_s = 4$ nm, and (c) $d_s = 5$ nm.

6.4 Molecular dynamics simulation procedure

In a molecular dynamics simulation, the phase-space trajectory of a system of particles is predicted by solving the Newton equations. The required inputs are an atomic structure and a suitable interatomic potential, which can be obtained from experiments and/or *ab initio* calculations [130].

The interatomic potential can be assumed to be in the form

$$\varphi(r_{ij}) = \frac{q_i q_j}{r_{ij}} + A_{ij} \exp\left(-\frac{r_{ij}}{r_{\mathrm{o},ij}}\right) + \frac{C_{ij}}{r_{ij}^6}, \tag{6.1}$$

where $\varphi(r_{ij})$ is the interaction energy of atoms i and j, which consists of a Coulomb term and a covalent (short range) contribution, cast into the usual Buckingham form [131]. Here q_i is an effective charge of the ith atom, r_{ij} is the interatomic distance between atoms i and j, A_{ij}, ($r_{\mathrm{o},ij}$ and C_{ij} are parameters for covalent interactions. For ionic materials, this Buckingham interatomic potential model has been shown to perform well. The parameters in Eq. (6.1), obtained from [132, 133], are listed in Table 6.1. This potential set has been verified to reproduce the bulk properties (lattice constant, lattice position, bulk modulus, elastic constant, etc) well [134].

To determine the DOS of the bulk crystal, molecular dynamics simulations are carried out in a cubic computation domain which contains $2 \times 2 \times 2 = 8$ unit cells containing $N = 640$ atoms (256 Y and 384 O). The MD code, which was developed by McGaughey and Kaviany [135] to model the thermal conductivity, has been used. Periodic boundary conditions are applied in all directions. For the nanopowder, the computation domain is a sphere of diameter d_s, which is cut from a much larger bulk crystal, as shown in Figure 6.2. It should be noted that a nanopowder generated in

Table 6.1: Parameters used in the Buckingham potential

Atomic charges: $q_{\mathrm{Y}} = 3$, $q_{\mathrm{O}} = -2$

Atom-Atom	A_{ij}, eV	$r_{\mathrm{o},ij}$, Å	C_{ij}, eV-Å	References
Y-Y	0	1	0	[133]
Y-O	1345.6	0.3491	0	[132, 133]
O-O	22799	0.149	27.93	[132, 133]

this way may not be neutral in charge, thus some atoms at the surface may need to be removed accordingly, to eliminate any net charge of the nanopowder. Also, since the center of the sphere can be randomly selected, we have many possible configurations given the diameter. As such, a number of spherical particles with different configurations are considered in this study, and their behaviors are compared. The free boundary condition is used.

For both bulk and nano crystals, an initialization period of 5×10^4 time steps is used, with the time step being 1.6 fs. The system is run in the NVT (constant mass, volume and temperature) ensemble. To set the temperature for the NVT ensemble, the potential energy of the system is monitored every time step. When it reaches a value within $10^{-4}\%$ of the desired value, the ensemble is switched to NVE (constant mass, volume and energy), and the system is run until the total number of time steps is 1.5×10^5.

6.5 Simulation results and analysis

6.5.1 Decomposition of the velocity-velocity autocorrelation function to surface and internal modes

Typically, the normalized velocity-velocity autocorrelation function is determined for each species in the system. Here we have yttrium and oxygen atoms, and the autocorrelation function for the specie α (α = Y, O) is

$$\Gamma_\alpha(t) = \left\langle \sum_{i_\alpha=1}^{N_\alpha} \mathbf{u}_{i_\alpha}(t)\mathbf{u}_{i_\alpha}(0) \right\rangle / \left\langle \sum_{i_\alpha=1}^{N_\alpha} \mathbf{u}_{i_\alpha}(0)\mathbf{u}_{i_\alpha}(0) \right\rangle, \ \alpha = \mathrm{Y}, \mathrm{O}, \tag{6.2}$$

where N_α is the number of atoms of species α, $\mathbf{u}_{i_\alpha}$ is the velocity of atom i_α and $\langle\rangle$ is an ensemble average.

For nanocrystals, the internal and surface atoms vibrate differently. The crystal structure of the internal region is similar to that of bulk crystals, which implies that the internal atoms behave as if they were in a bulk crystal. On the other hand, the surface structure deviates much from the bulk structure since surface atoms lose their outer neighboring atoms, leading to different bond lengths, bond angles, etc. It is straightforward to consider the internal and surface regions separately, although the exact boundary between these regions cannot be well defined. In our practice, the spherical shell with a thickness 3 Å is taken as the surface region, and the more inside region is considered as internal region. All atoms are hence decomposed into four categories: surface yttrium atoms, internal yttrium atoms, surface oxygen atoms, and internal oxygen atoms. The number and population fraction for these four categories are shown in Table 8.1, for nanoparticles with increasing size. As expected, the surface

Table 6.2: Number and fraction of atoms for nanocrystals with various sizes

	Surface Y		Internal Y		Surface O		Internal O	
	$N_{\alpha\beta}$	%	$N_{\alpha\beta}$	%	$N_{\alpha\beta}$	%	$N_{\alpha\beta}$	%
$D = 3$ nm	182	19.4	198	21.1	265	28.3	293	31.2
$D = 4$ nm	349	15.7	512	23.0	543	24.4	825	37.0
$D = 5$ nm	564	12.9	1203	27.4	839	19.1	1782	40.6
$D = 6$ nm	825	10.9	2212	30.0	1225	16.1	3340	43.9

region takes a smaller portion as the particle becomes larger, and the limit is that the surface effects can be neglected as the system is sufficiently large to recover the bulk phase.

The autocorrelation function for specie α (α = yttrium, oxygen), region β (β = surface, internal) is given by

$$\Gamma_{\alpha\beta}(t) = \left\langle \sum_{i_{\alpha\beta}=1}^{N_{\alpha\beta}} \mathbf{u}_{i_{\alpha\beta}}(t)\mathbf{u}_{i_{\alpha\beta}}(0) \right\rangle \Big/ \left\langle \sum_{i_{\alpha\beta}=1}^{N_{\alpha\beta}} \mathbf{u}_{i_{\alpha\beta}}(0)\mathbf{u}_{i_{\alpha\beta}}(0) \right\rangle, \quad \alpha = \text{yttrium, oxygen. } \beta = \text{surface, internal} \tag{6.3}$$

where the double subscript $\alpha\beta$ denotes atoms of species α and in region β, then $N_{\alpha\beta}$ is the number of atoms of species α and in region β, $\mathbf{u}_{i_{\alpha\beta}}$ is the velocity of atom $i_{\alpha\beta}$ and $\langle\rangle$ is an ensemble average.

The velocity-velocity autocorrelation functions are calculated for these four categories of atoms, and are shown in Fig. 6.3. The vibrational frequencies of yttrium atoms are considerably lower than those for oxygen atoms, because the atomic mass for yttrium atom is much larger. However, no evident difference is observed between

the surface and internal regions for the same species, and it will be resolved in the phonon density of states in the next section.

6.5.2 Results of the phonon density of states for nanoparticles

The frequency spectrum of the normalized velocity autocorrelation function gives the partial phonon DOS $D_{p,\alpha\beta}(\omega)$, as

$$D_{p,\alpha\beta}(\omega) = \int_0^\tau \Gamma_{\alpha\beta}(t)\cos(\omega t)dt. \tag{6.4}$$

Generally, the partial phonon density of states calculated in this way can only give the shape of the spectrum, while the absolute values are meaningless. Recognizing that a system with $N_{\alpha\beta}$ atoms has $3N_{\alpha\beta}$ modes, where 3 is the number of degrees of freedom, we can scale $D_{p,\alpha\beta}(\omega)$,

$$D_{p,\alpha\beta,N_{\alpha\beta}} = c_1 D_{p,\alpha\beta}, \tag{6.5}$$

where c_1 is a constant such that

$$\int_0^\infty D_{p,\alpha\beta,N_{\alpha\beta}}(\omega)\mathrm{d}\omega = 3N_{\alpha\beta}. \tag{6.6}$$

Then these partial phonon DOSs are addable, and the total phonon density of states of a system is just the summation of the partial phonon DOS:

$$D_p(\omega) = \sum_\alpha \sum_\beta D_{p,\alpha\beta,N_{\alpha\beta}}. \tag{6.7}$$

It is evident that $D_{p,\alpha\beta,N_{\alpha\beta}}$ is dependent on $N_{\alpha\beta}$, the size of the system. To compare the spectra shape for systems with different number of atoms, it is necessary

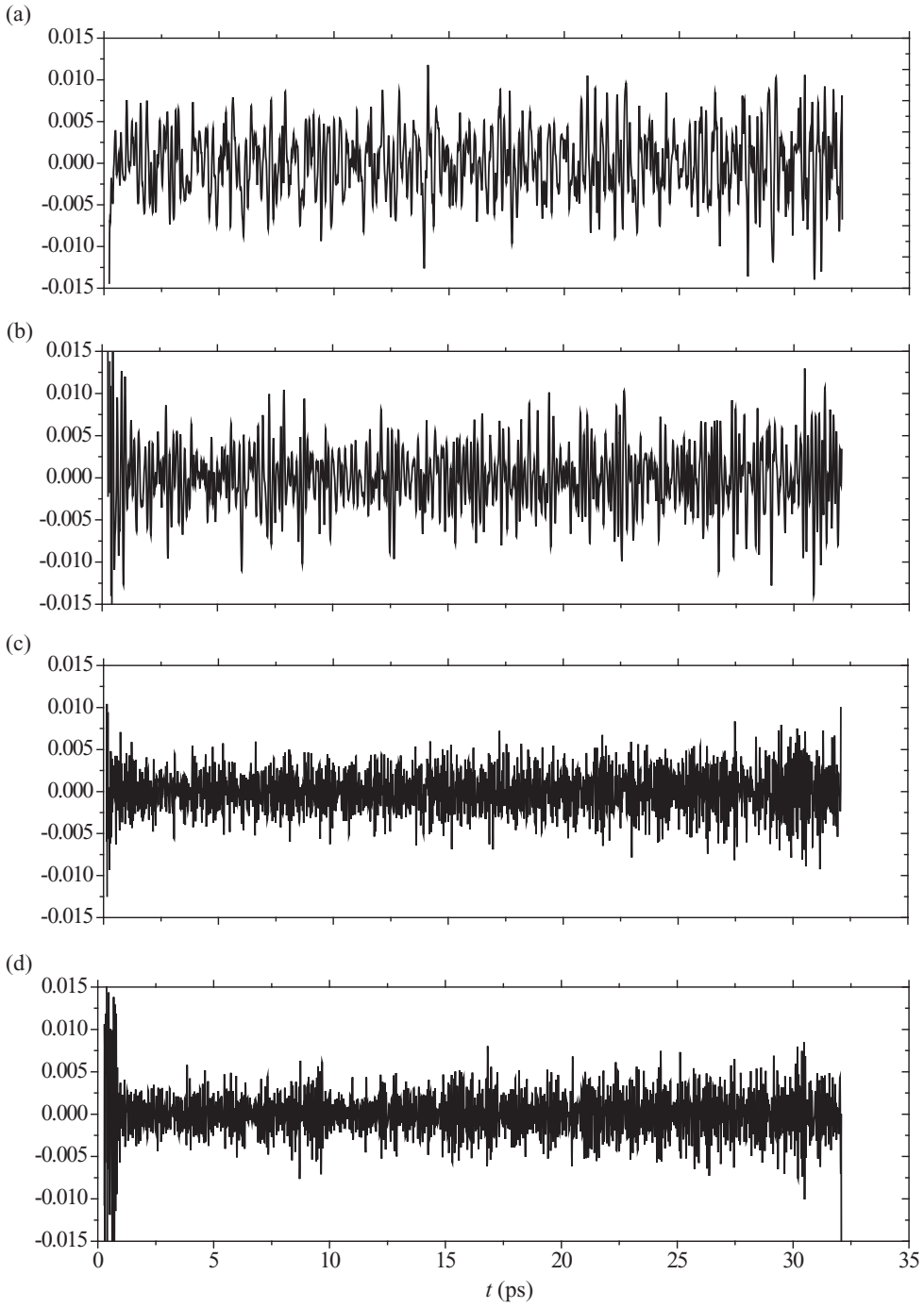

Figure 6.3: Velocity-velocity autocorrelation functions for (a) surface yttrium atoms, (b) internal yttrium atoms, (c) surface oxygen atoms, and (d) internal oxygen atoms.

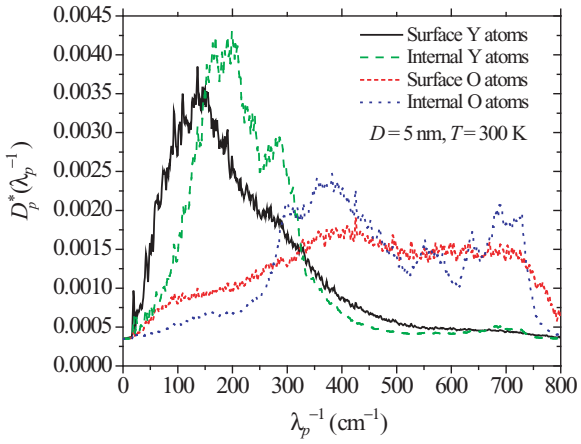

Figure 6.4: Normalized partial phonon density of states of the surface Y atoms, internal Y atoms, surface O atoms, and internal O atoms.

to define a normalized partial phonon density of states, as

$$D^*_{p,\alpha\beta} = \frac{D_{p,\alpha\beta,N_{\alpha\beta}}}{3N_{\alpha\beta}}. \tag{6.8}$$

Therefore $D^*_{p,\alpha\beta}(\omega)$ satisfies the condition

$$\int_0^\infty D^*_{p,\alpha\beta}(\omega)d\omega = 1, \tag{6.9}$$

and therefore it is called a normalized partial phonon DOS. The normalized partial phonon DOS $D^*_{p,\alpha\beta}(\omega)$ are calculated for a Y_2O_3 nanoparticle with $D = 5$ nm, and the results are shown in Fig. 6.4. As indicated by the velocity-velocity autocorrelation function, oxygen atoms have more high-frequency modes than yttrium atoms, due to their lighter mass. For yttrium species, the surface region has more modes in high and low frequency tails, while the internal region has more modes in the intermediate frequency range. Similar behavior is observed for oxygen species.

These normalized partial phonon DOS can be used as building blocks for higher level partial DOS. For example, the normalized partial DOS for the species α is given

by

$$D^*_{p,\alpha} = \sum_{\beta} \frac{c_{\alpha\beta}}{c_\alpha} D^*_{p,\alpha\beta}, \tag{6.10}$$

where c_α is the population weight for species α, given by

$$c_\alpha = \sum_{\beta} c_{\alpha\beta}. \tag{6.11}$$

Similarly, the normalized partial DOS for the region β is given by

$$D^*_{p,\beta} = \sum_{\alpha} \frac{c_{\alpha\beta}}{c_\beta} D^*_{p,\alpha\beta}, \tag{6.12}$$

where c_β is the population weight for region β, given by

$$c_\beta = \sum_{\alpha} c_{\alpha\beta}. \tag{6.13}$$

The total phonon DOS is obtained by summing over the partial DOS weighted with the population, i.e.,

$$D^*_p = \sum_{\alpha} \sum_{\beta} c_{\alpha\beta} D^*_{p,\alpha\beta}. \tag{6.14}$$

The normalized partial phonon DOS $D^*_{p,\beta}(\omega)$ for the surface and internal regions are calculated for the same nanocrystal, and the results are shown in Fig. 6.5. Also shown are the total phonon DOS for the nanocrystal and for the bulk material. It can be seen that the phonon DOS of nanocrystals is distinct from that of the bulk crystal, in its broadened peaks, and extended tails at low and high frequencies. The bulk crystal has sharp, well-defined peaks (or modes) related to the rigorous periodic structure, while these peaks are broadened in the nanocrystal, due to the loss to some extent of this periodicity. The high frequency tail in the nanocrystal phonon DOS

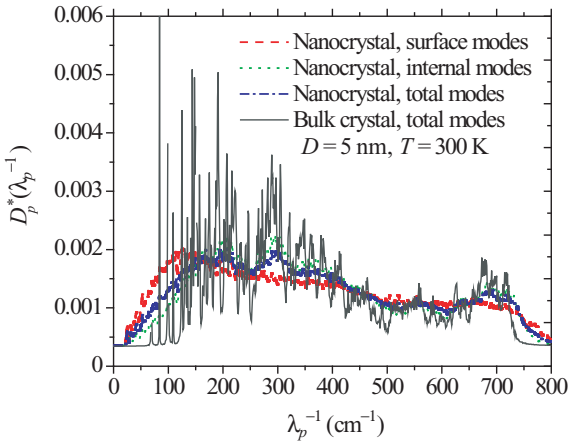

Figure 6.5: Comparison of the phonon DOS of the bulk crystal and nanocrystal for Y_2O_3. The nanocrystal DOS possesses extended low- and high-frequency tails.

is believed to result from the surface atoms. Due to the loss of the attraction from their outer neighbors, these atoms have contracted bonds with their inner neighbors, compared to the bulk crystal. This leads to a "harder" surface and the increased vibrational frequencies.

6.6 Enhancement of excitation coefficient using nanopowders

Using the resonance wavelength ($\lambda_{e,g} = 980$ nm) for Yb^{3+}: Y_2O_3 along with the phonon DOS determined in section **??**, the variations of the normalized (against the resonance) transition coefficient $B^*_{e,a} = B_{e,a}(\lambda_{ph,i})/B_{e,a}(\lambda_{ph,i} = 980$ nm), as a function of the pumping wavelength $\lambda_{ph,i}$, are shown in Fig. 6.6(a), for bulk and nano crystals. Note that a singularity exists for $B_{e,a}(\lambda_{ph,i})$ right on resonance $\lambda_{ph,i} = 980$ nm, so we use the limit $B_{e,a}(\lambda_{ph,i} = 980$ nm$) = B_{e,a}(\lambda_{ph,i} \rightarrow 980$ nm$)$. The transition coefficients

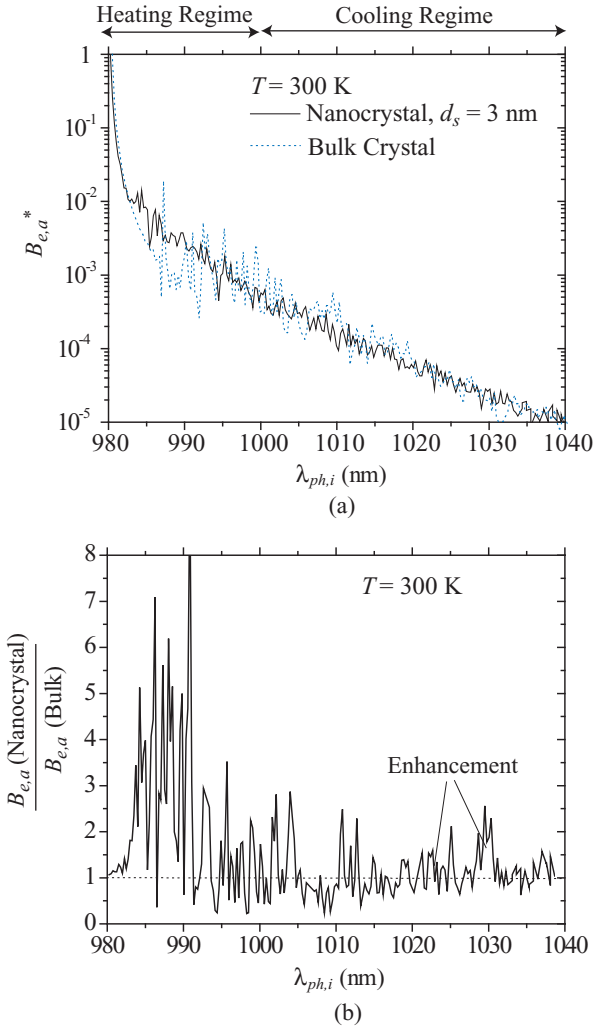

Figure 6.6: (a) Variations of the normalized (against the resonance) electronic transition coefficient $B^*_{e,a} = B_{e,a}(\lambda_{ph,i})/B_{e,a}(\lambda_{ph,i} = 980 \text{ nm})$ with respect to the laser pumping wavelength, for the bulk and the nanoparticle crystals, for Yb^{3+}: Y_2O_3. (b) The ratio of the transition coefficients for the nanocrystal and the bulk crystal.

show an exponential decay with the increasing wavelength. Shown in Fig. 6.6(b) is the ratio of the transition rates for nano- and bulk crystals. The transition rates may be enhanced (the area above the dotted line) or reduced (the area below the dotted line), depending on the pumping wavelength used. However, in the practical cooling range ($\lambda_{ph,i}$ = 1,020 to 1,030 nm) used in most experiments, more enhancement is observed than reduction.

6.7 Discussions and summary

Here we have suggested modification of the phonon DOS due to the finite-small size of the nanocrystals. For the bulk materials, the phonon DOS can also be engineered using different host materials. We note that this would also alter the ion-phonon coupling.

Next we will discuss the last carrier considered in this study: ion (or electron).

Chapter 7

Optimum ion dopant concentration

7.1 Introduction

A higher value of n_d, the dopant concentration, is desirable in laser cooling experiments, since more absorbers are available, which will compensate for the low absorption cross section. However, the negative side effect is that the excitation energy may hop around neighboring ions until it finds a quenching center to decay nonradiatively, as ions are closer to each other. This energy transfer mechanism leads to a drop in the quantum efficiency η_{e-ph}, and is an effect called the concentration quenching. Hence, an optimum dopant concentration, corresponding to a balance between the increase in n_d and the decrease in η_{e-ph}, should exist. However, due to the prior lack of a theory to describe this optimum concentration, arbitrary concentrations of 1 wt.% (corresponding to 2.42×10^{20} cm^{-3}) and 2 wt.% have been used in most of the existing experiments. In this section we suggest a criterion for determining the optimum concentration.

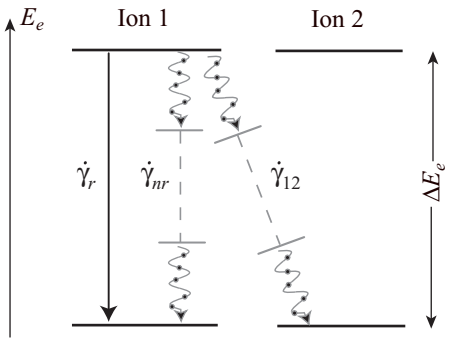

Figure 7.1: Energy transfer scheme for the self-generated multiphonon assisted process $\dot{\gamma}_{12}$ between neighboring ions. The wavy lines indicate nonradiative transitions, $\dot{\gamma}_r$ and $\dot{\gamma}_{nr}$ are isolated ion radiative and nonradiative decay rates.

7.2 Optimum dopant concentration in laser cooling of solids

In highly pure Yb^{3+}-doped crystals, which are preferred in laser cooling experiments, nonradiative processes should be rather weak, and they essentially come from the self-generated quenching processes [136, 137]. In such an event, one excited ion transfers its excitation energy to its identical neighbor, then to the lattice phonon modes, through a multiphonon relaxation process, as shown in Fig. 7.1. The neighbor ion ends up at its ground state. As the dopant concentration increases, the radiative decay rate remains unchanged, while the nonradiative decay rate increases due to the increase of the self quenching rate $\dot{\gamma}_{12}$, and as a result, the total decay rate is increased. This mechanism results in a decrease in both the lifetime of the excited state and the quantum efficiency.

Based on the energy transfer theory, the excited state lifetime as a function of

dopant concentration is [136]

$$\tau(n_d) = \frac{\tau(n_d = 0)}{1 + 1.45(n_d/n_{d,c}) \exp[-\beta(E_p, T)\Delta E_e/4]}, \tag{7.1}$$

where $\tau(n_d = 0)$ is the lifetime at extremely low concentration, $n_{d,c}$ is defined as a critical concentration intrinsically dependent on the ion-host coupling, E_p is the phonon energy, ΔE_e is the energy gap between the two levels, and $\beta(E_p, T)$ is an energy transfer coefficient as a function of phonon energy and temperature. Here for Yb^{3+}: Y_2O_3, $\beta(E_p, T)$ is given by the following expression [136]

$$\beta(E_p, T) = \frac{\ln[4.077/(1 + f^{\mathrm{o}}_{p,e})]}{\hbar_{\mathrm{P}}\omega_{p,e}}, \tag{7.2}$$

where $\omega_{p,e}$ is the effective phonon frequency involved in the self quenching process, and $f^{\mathrm{o}}_{p,e}$ is the equilibrium distribution function of phonon (the Bose-Einstein distribution), given by

$$f^{\mathrm{o}}_{p,e} = \frac{1}{\exp(\hbar_{\mathrm{P}}\omega_{p,e}/k_{\mathrm{B}}T) - 1}. \tag{7.3}$$

Note that here we made an assumption of involving only one effective phonon mode $\omega_{p,e}$ in the self quenching process. This approximation has proven very useful in understanding the multiphonon radiationless energy transfer processes of many rare-earth-doped solids, especially for systems involving weak coupling like Yb^{3+}: Y_2O_3 considered here. However, it must be noted that the frequency spectrum of phonons for any solid has a significant amount of structure in its DOS, and they may all contribute to the electron-phonon coupling. For physical systems involving strong coupling, the specific structure of the phonon spectra must be taken into account [68].

Equation (7.1) predicts that the lifetime decreases as the dopant concentration increases. Since the lifetime is the reciprocal of the transition rate, One can rewrite Eq. (7.1) as

$$\dot{\gamma}_{e,d}(n_d) = \dot{\gamma}_{e,d}(n_d = 0)\{1 + 1.45(n_d/n_{d,c}) \exp[\beta(E_p, T)\Delta E_e/4]\}, \tag{7.4}$$

where, based on the process shown in Fig. 7.1, we have

$$\dot{\gamma}_{e,d}(n_d = 0) = \dot{\gamma}_r + \dot{\gamma}_{nr}, \tag{7.5}$$

and

$$\dot{\gamma}_{e,d}(n_d) = \dot{\gamma}_r + \dot{\gamma}_{nr} + \dot{\gamma}_{12}. \tag{7.6}$$

It is predicted in Eq. (7.4) that an increase in n_d results in the increase in the total decay rate $\dot{\gamma}_{e,d}$, compared to that for an isolated ion, due to the presence of the self-generated, non-radiative decay rate $\dot{\gamma}_{12}$.

For an isolated Yb^{3+} ion in Y_2O_3 host, the nonradiative decay rate $\dot{\gamma}_{nr}$ is negligible compared to the radiative decay rate $\dot{\gamma}_r$, below the room temperature (< 300 K). Thus we can make an approximation

$$\frac{\dot{\gamma}_r}{\dot{\gamma}_r + \dot{\gamma}_{nr}} \simeq 1. \tag{7.7}$$

This indicates that the total decay rate at low concentration is taken as the radiaitve decay rate, and all nonradiative decay events come from the energy transfer processes.

Using Eqs. (7.4)-(7.7), the quantum efficiency η_{e-ph} can be written as a function of the concentration as

$$\eta_{e-ph} = \frac{\dot{\gamma}_r}{\dot{\gamma}_{e,d}(n_d)} = \frac{\gamma_r}{\dot{\gamma}_r + \dot{\gamma}_{nr}} \frac{\dot{\gamma}_r + \dot{\gamma}_{nr}}{\dot{\gamma}_{e,d}(n_d)}$$

$$= \quad \{1 + 1.45(n_d/n_{d,c}) \exp[-\beta(E_p, T)\Delta E_e/4]\}^{-1}. \tag{7.8}$$

It is predicted in this relation that the quantum efficiency decreases as the dopant concentration and temperature increase, as expected. The temperature effect is due to that more phonons are excited and participate in the nonradiative processes. The total cooling power given by Eq. (3.21) is now written as a function of the concentration, i.e.,

$$\dot{S}_{ph\text{-}e\text{-}p} = \left\{1 - \frac{\bar{\omega}_{ph,e}}{\omega_{ph,i}}[1 + 1.45\frac{n_d}{n_{d,c}} \exp(-\beta\Delta E_e/4)]^{-1}\right\} \hbar_{\mathrm{P}}\omega_{ph,i}\dot{\gamma}_{e,a}n_d \int_V e_{ph,i}dV. \tag{7.9}$$

The maximum cooling power is reached when

$$\frac{\partial \dot{S}_{ph\text{-}e\text{-}p}}{\partial n_d} = 0, \tag{7.10}$$

which yields the optimum concentration

$$n^*_{d,o} = \frac{n_{d,o}}{n_{d,c}} = A\frac{(1-B)^{1/2}}{1-(1-B)^{1/2}}, \tag{7.11}$$

where A and B are

$$A = \frac{1}{1.45} \exp[\beta(E_p, T)\Delta E_e/4], \;\; B = \frac{\lambda_{ph,e}}{\bar{\lambda}_{ph,i}}. \tag{7.12}$$

It is evident in Eq. (7.11) that the critical concentration $n_{d,c}$ is the only parameter that needs to be specified before the optimum concentration can be determined. Note that $n_{d,c}$ is an intrinsic property depending on the ion-dopant pair and the temperature, and may be calculated using quantum mechanics. Here, we use a more practical approach, namely, fitting Eq. (7.1) or Eq. (7.8) to experiments, as reported in [136].

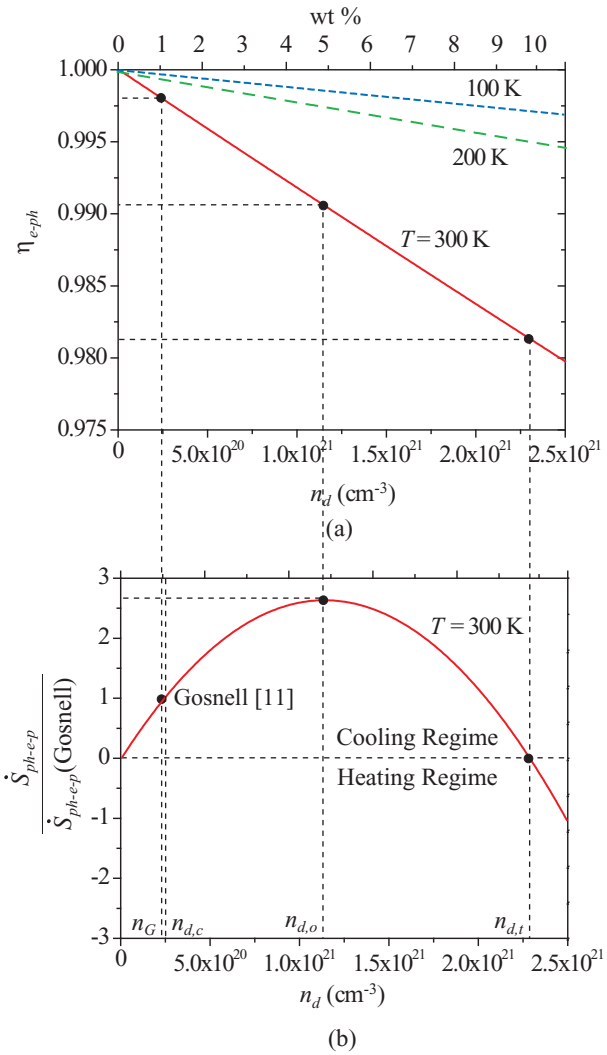

Figure 7.2: (a) Variation of the quantum efficiency as a function of dopant concentration. (b) Variation of the normalized cooling power as a function of dopant concentration. The Gosnell $n_{d,G}$, critical $n_{d,c}$, optimum $n_{d,o}$, and transition $n_{d,t}$ dopant concentrations are shown.

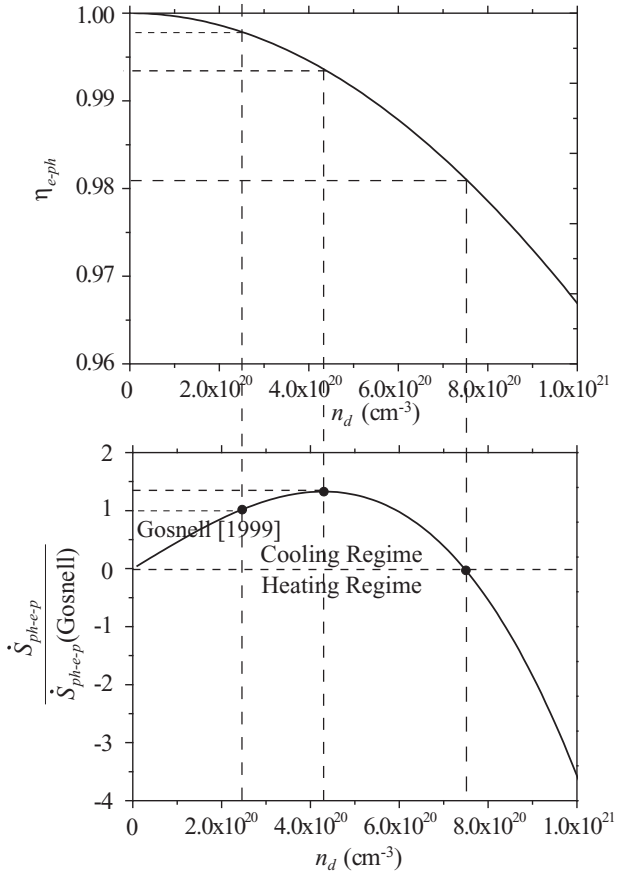

Figure 7.3: (a) Variation of the quantum efficiency as a function of dopant concentration, under the power law assumption. (b) Variation of the normalized cooling power as a function of dopant concentration, under the power law assumption.

In an experiment [2], a Yb^{3+} doped ZBLANP fibre was cooled by 65 K from the room temperature, with a concentration $n_d = 2.42 \times 10^{20}$ cm^{-3}, and a measured quantum efficiency $\eta_{e-ph} = 0.998$. Using Eq. (7.8), the critical concentration is readily calculated to be $n_{d,c} = 2.51 \times 10^{20}$ cm^{-3}. Then, by using Eq. (7.8), the variations of the quantum efficiency is plotted as a function of the concentration, for three temperatures, as shown in Fig. 7.2(a). The results show that the quantum efficiency η_{e-ph} decreases monotonically with the dopant concentration and temperature. By using Eq. (7.9), the variation of the normalized cooling power is plotted as a function of the concentration in Fig. 7.2(b). The results show that the cooling power first increases and then decreases, as n_d increases. At an optimum concentration $n_{d,o} = 1.13 \times 10^{21}$ cm^{-3}, which is three times higher than that used by Gosnell [2], the maximum cooling power is achieved and is 2.6 times that obtained in that investigation [2]. Note that if the concentration becomes higher than a transition value $n_{d,t}$, which is 2.05×10^{21} cm^{-3}, the cooling effect is eliminated (See Fig. 7.2(b)). This is expected, due to the resulting low quantum efficiency.

To examine the dependence of the optimum concentration on temperature, we use Eq. (7.11) and the results are shown in Fig. 7.4. Since the quantum efficiency increases as the temperature decreases, we expect the optimum concentration to also increase. This is true, as shown in Fig. 7.4, if we assume that the mean emission wavelength $\lambda_{ph,e}$ is not dependent on temperature. However, in reality the mean emission wavelength $\bar{\lambda}_{ph,e}$ increases as the temperature decreases, since the electrons in the excited state are more likely to reside in the lowest sublevels, resulting in emission photons with lower energy and longer wavelength. Lei et al performed an experimental

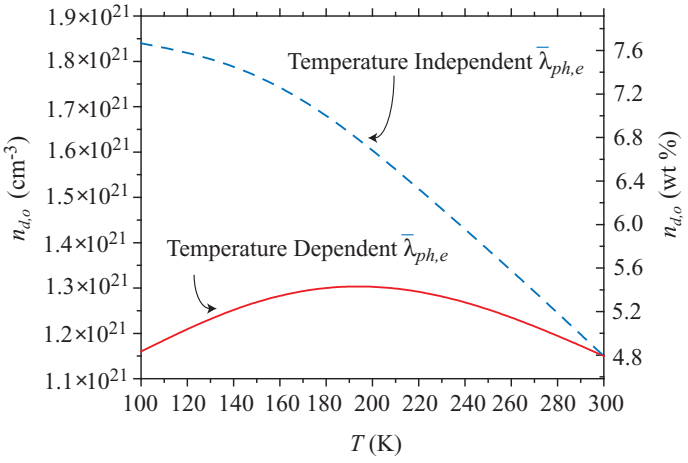

Figure 7.4: Variation of the optimum concentration as a function of temperature, for temperature independent and dependent $\bar{\lambda}_{ph,e}$.

study on the relation between $\bar{\lambda}_{ph,e}$ and T [138], and their data are fitted by us using an empirical relation, which reads $\bar{\lambda}_{ph,e} = 1003+(996-1003)/(300-100)*(T-100)$ nm. Taking into account this dependence, the variation of the optimum concentration with temperature is shown in Fig. 7.11. Interestingly, it first increases, but then decreases, as the temperature decreases. The reason is that, at very low temperatures, the mean emission wavelength increases, leading to a reduction of the cooling ability per ion. As a result, the cooling effect is more likely to be destroyed by the nonradiative decays which can be caused by large concentrations. This variation of the optimum concentration with the temperature reflects the competition and balance between the quantum efficiency and the mean emission wavelength.

7.3 Discussions and summary

We note that even though this optimum concentration analysis is performed explicitly for nanocrystals, it is also applicable to bulk materials. A recent spectroscopic experiment [139] on a bulk material indicates that the optimum concentration may be around 4-5%, validating our prediction.

Chapter 8

Conclusions, future work, and outlook

8.1 Laser cooling enhancement: achieving cryogenic temperature

We have investigated the enhanced laser cooling of nanopowders, using the optimization of the dopant concentration, the photon localization, and the phonon DOS size effect. Taking a closer look at these three mechanisms, we notice that they all facilitate to increase the carrier number in the interacting volume: optimization of the dopant concentration for higher electron number, photon localization for higher photon number, and phonon DOS size effect for higher phonon number in the desired range. This seems to be straightforward since the excitation is a photon induced, phonon assisted, electronic absorption. Thinking of an interaction of only one pho-

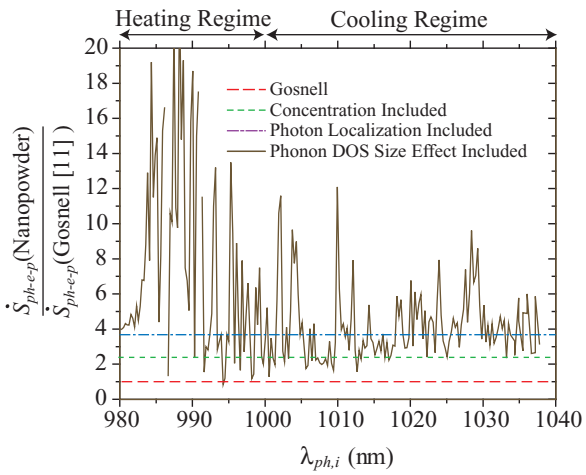

Figure 8.1: Enhancement of laser cooling power by (i) optimization of the dopant concentration, (ii) photon localization, and (iii) phonon DOS size effect. The base line is the experiment of Gosnell [2]. The cooling and heating regimes are shown.

ton, one phonon, and one electron (ion) as the base system, to increase the number of each type of carrier would independently enhance the excitation events proportionally. This is an important yet intuitive finding that more carriers are needed to be put in the same interacting volume, to enhance their interactions. The enhancement effects due to each carrier are summarized in Fig. 8.1.

The optimum dopant concentration is pursued using the energy transfer theory. Although it is well known that an optimum concentration for maximum cooling performance should exist (since high concentration would result in a low quantum efficiency), a quantitative analysis had been lacking. Here, we apply the energy transfer theory and obtain an analytical expression for the optimum concentration. For high purity doped solids, the concentration quenching is identified as a self-generated multiphonon decay process, allowing to establish a relation between the quantum efficiency and the concentration. The results show that the optimum concentration

gives a 150% enhancement in cooling power, as shown in Fig. 8.1. This enhancement mechanism applies to both the bulk and the nanoparticle crystals doped with Yb^{3+}.

The cooling performance in nanocrystals may also be enhanced compared to that of bulk crystals, due to photon localization. Calculations based on the Maxwell equations show that as the particle size decreases to the order of the pumping wavelength, photons are localized in the interior of the powder media due to recurrent scattering. As a result, the total pumping energy (or the photon density) is enhanced, leading to an enhanced absorptivity. This mechanism is expected to have a 50% enhancement on the cooling power for nanopowders, compared to the bulk crystals, as shown in Fig. 8.1. It is shown that the reabsorption is negligible.

The phonon DOS size effect is also considered. The phonon DOS of nanoparticle crystal is determined using molecular dynamics simulations and the Fourier transform of the velocity autocorrelation function. The DOS of nanocrystals possesses the extended, small tails at low and high frequencies. Treating the cooling process as a phonon-assisted transition, a second order quantum mechanical calculation is performed to predict the transition rates. As shown in Fig. 8.1, this mechanism may enhance or reduce the cooling performance, depending on the pumping wavelength used. In the practical cooling range (λ_i = 1,020 to 1,030 nm), more enhancement is shown than reduction. If the broadening of the absorption spectra is taken into account, we can conclude that the phonon size effect would generally enhance the cooling performance.

Considering all these three mechanisms, the cooling power is predicted to be enhanced by about 275% in nanocrystalline powders.

Based on the above results, we now estimate the enhanced cooling performance in the sample that we plan to use in our experiment. The sample is a 1 mm long, 170 μm diameter cylinder composed of nanopowders, subject to laser irradiation from one end, as shown in Fig. 3.1. The only external load is the thermal radiation from surroundings. Since the external radiative resistance is much larger than the internal conductive resistance, the sample can be assumed to be at a uniform temperature T, and the steady-state, integral-volume energy equation is

$$\dot{S}_{ph\text{-}e\text{-}p} + Q_{r,b} = 0, \tag{8.1}$$

where the thermal radiation load $Q_{r,b}$ is given by

$$Q_{r,b} = \left(\frac{1}{2}\pi D^2 + \pi DL\right) \epsilon_r \sigma_{\mathrm{SB}} (T_\infty^4 - T^4). \tag{8.2}$$

Gosnell cooled a Yb^{3+}-doped solid 65 K below the room temperature [2]. Here we keep all the conditions the same as in [2], but only change the bulk sample into a nanopowder composite. The key parameters used in [2] and in the current estimation are listed in Table 8.1, quantities with a star means they are scaled to Gosnell's values. Note that $\bar{\lambda}_e$ is assumed the same since the blue shift of luminescence in nanocrystals is small [140]. The resulting n_d, $D_p(E_p)$, $N_{ph,i}$ and ΔT in nanopowders are enhanced by about 300%, 50%, 50%, and 200%, respectively. Note that the temperature dependence of the quantities in Eq. (3.21) has been included. The results imply the possibility to cool the element down to 127 K starting from the room temperature, creating as large as a 173 K temperature difference! This will be sufficient for many cryogenic applications, and will be an important step towards achieving even lower temperatures.

Table 8.1: Parameters used in this study of laser cooling enhancement

Parameters	Existing Literature [2]	This Study
$Q_{r,i}$ (W)	2.2	2.2
n_d (cm^{-3})	2.42×10^{20}	1.13×10^{21}
$D_p^*(E_p)$	1	1.5
$N_{ph,i}^*$	1	1.5
ΔT (K)	65	173

8.2 Original contributions of this work

A number of significant contributions have been made in this work:

• *The application of the Fermi golden rule to laser cooling of solids.* The Fermi golden rule is used as the primary theoretical tool to treat laser cooling of solids. This is inspired by a careful examination of the cooling physics, recognizing that laser cooling is a photon-induced, phonon-assisted, electronic transition. The Fermi golden rule approach allows one for identifying the limiting factors for such a complex process as laser cooling of solids. Here the carrier couplings and populations are determined as the two kinds of limiting factors, and these quantities further include the photon-electron coupling, electron-phonon coupling, ion-dopant concentration, phonon density of states, and the photon population. The Fermi golden rule theory of laser cooling of solids opens the door for the optimum selection of material and structure for this application.

• *Ab initio calculations of the photon-electron and electron-phonon coupling rates.*

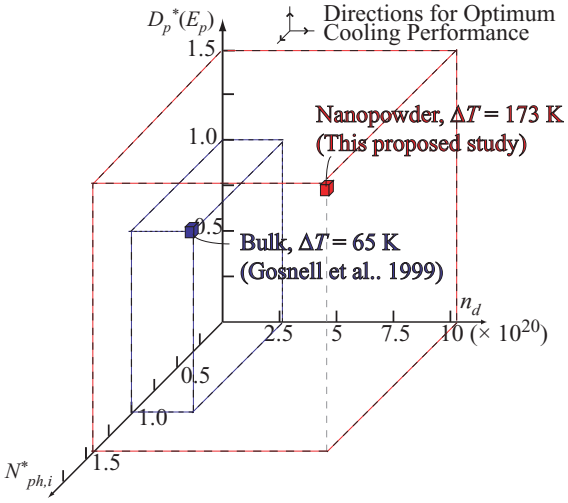

Figure 8.2: Comparison of n_d, $D_p(E_p)$, $N_{ph,i}$, and the resulting ΔT, for bulk material [2], and nanopowders. The proposed nanopowder aims at increasing each parameter further.

An ab initio approach is developed to determine the photon-electron and electron-phonon couplings rates, and it is a first of this kind on ion-doped materials. Using the first-principle wavefunctions, the electric transition dipole moment between the ground and excited states is calculated, and is found to be highly dependent on the symmetry properties of the molecular structure. The electron-phonon coupling is caused by the modification of the electronic wavefunction in response to the nuclei motions, and by the modifications of the vibrational modes before and after the transition. This theory is used to calculate the nonradiative decay rate, which is strongly dependent on the temperature. This approach provides a theoretical tool for optimal selections of laser cooling materials, including both dopants and hosts.

- *Optimization of carrier populations using nanopowder size effects.* The carrier populations are optimized from the perspective of nanostructures, in particular, nanopowders. The concept of the optimum dopant concentration is established and

determined using the energy transfer theory for concentration quenching, and is found to be larger than the currently used value. Using molecular dynamics simulations, the phonon density of states (DOS) of the nanopowder is found to have broadened modes, and extended tails at low and high frequencies. It is advantageous over bulk materials because more phonon modes are available in the desired range. The pumping field energy is calculated by solving the Maxwell equations in random nanopowders. Photons are multiply scattered and do not propagate through the medium, and large field enhancement is observed. This leads to the trapping of more photons in nanopowder media, compared to bulk materials, implying more efficient absorption and cooling performance. Owning to these enhancement effects, a thermal modelling shows that nanopowders are expected to be cooled to cryogenic temperature range. Our work is the first analysis of laser cooling in nanostructures, and the first attempt to advance laser cooling of solids to the cryogenic temperature range.

8.3 Future work

There are a few directions that this work can be extended.

• Extension of the ab initio calculations to ion-doped periodic solids. Due to the limitations of the state-of-the-art ab initio computation techniques, the ab initio calculations of the photon-electron and electron-phonon couplings are restricted to ion-doped clusters. With the advance in the ab initio techniques, they are expected to be capable of calculating the excited states of ion-doped lattice.

• Optimization and design of phonon density of states. Core-shell potential model

can be used, and compared to those of the rigid ion model presented in this work. This is based on the suggestion that the ionic polarisability should be taken into account to get an accurate description of the vibrational properties of ionic crystals [141, 142], like Y_2O_3 considered in this study. The polarisability effect may be even more important for nanocrystals, since the surface atoms lose their outer neighbors and the charge distribution is dramatically changed. Also, the size of the nanoparticles considered in this study can be extended to 30 nm, when more powerful computational resources become available.

• Cavity design in one-dimensional systems. The study on field enhancement and photon localization presented in this study can be expanded in a few directions. For one-dimensional systems, the relationship between the field enhancement and the structural characteristics can be explored. With the advance in microelectronics technology, multilayer structures are expected to be fabricated with well-controlled layer thickness in the order of nanometer. This inspired the idea to design and fabricate multilayer structures with desired cavity properties.

• Optimization of the dopant concentration. In the current analysis, we considered the concentration quenching effect on the quantum efficiency. In a real sample, especially when the size is large, the reabsorption effect can also be included, given the geometry of the sample.

• Experiments. The cooling enhancement has partly relied on the size effect of phonon density of states, and the phonon-assisted interaction. To examine and enhance these, the excitation spectra of nanopowders can be measured. The lifetime measurement is needed to understand the concentration quenching and to find the op-

timum concentration. Finally, cooling experiments can be performed on Yb^{3+} doped crystalline Y_2O_3 nanopowders, to verify the predicted cryogenic temperatures. For low temperatures perhaps staging is needed where a single stage becomes inefficient.

Appendix A

Derivation of Fermi Golden Rule

The Fermi (or Fermi-Dirac) golden rule 3.31 allows for calculation of the transition rate between two eigenstates of a quantum system using the time-dependent perturbation theory. It can be derived from the time-dependent perturbation theory (the perturbation Hamiltonian, i.e., the scattering potential, is time dependent), under the assumption that the time of the measurement is much larger than the time needed for the transition.

It is the rate of gain of probability per unit time in the manifold of final eigenstate $|\psi_{\boldsymbol{\kappa}'}\rangle$ which is equal to the rate of loss of probability per unit time from the initial eigenstate $|\psi_{\boldsymbol{\kappa}}\rangle$.

Here we present a brief derivation of the Fermi golden rule. More details can be found in References [143, 144, 31]

A.1 Time-Dependent Perturbation

The general Hamiltonian of interest is of the form

$$\mathrm{H} = \mathrm{H_o} + \varphi_s, \tag{A.1}$$

where $\mathrm{H_o}$ is a time-independent Hamiltonian with known solutions

$$\mathrm{H_o}\psi_{\boldsymbol{\kappa}} = E_e(\boldsymbol{\kappa})\psi_{\boldsymbol{\kappa}} \tag{A.2}$$

$$\Psi^{\mathrm{o}}_{\boldsymbol{\kappa}} = \psi_{\boldsymbol{\kappa}} \exp[\frac{-iE_e(\boldsymbol{\kappa})t}{\hbar}], \tag{A.3}$$

and $E_e(\boldsymbol{\kappa})$ and $\psi_{\boldsymbol{\kappa}}$ are time-independent. The effect of φ_s is to cause time-dependent transitions between the states $\psi_{\boldsymbol{\kappa}}$. The time-dependent Schrödinger equation is

$$i\hbar\frac{\partial\Psi}{\partial t} = \mathrm{H}\Psi. \tag{A.4}$$

The approximation will involve expressing Ψ as an expansion of the time-independent eigenfunctions $\psi_{\boldsymbol{\kappa}} \exp[-iE_e(\boldsymbol{\kappa})t/\hbar]$ of the unperturbed, time-independent system

$$\Psi = \sum_{\boldsymbol{\kappa}} a_{\boldsymbol{\kappa}}(t)\Psi^{\mathrm{o}}_{\boldsymbol{\kappa}} = \sum_{\boldsymbol{\kappa}} a_{\boldsymbol{\kappa}}(t)\psi_{\boldsymbol{\kappa}} \exp[\frac{-iE_e(\boldsymbol{\kappa})t}{\hbar}]. \tag{A.5}$$

The time-dependent problem is solved when the coefficients $a_{\boldsymbol{\kappa}}(t)$ are known.

Substituting Eq. (A.5) into Eq. (A.4), also using Eq. (A.2), we get,

$$\sum_{\boldsymbol{\kappa}} i\hbar\frac{\partial a_{\boldsymbol{\kappa}}(t)}{\partial t}\psi_{\boldsymbol{\kappa}} \exp[\frac{-iE_e(\boldsymbol{\kappa})t}{\hbar}] + \sum_{\boldsymbol{\kappa}} a_{\boldsymbol{\kappa}}(t)E_e(\boldsymbol{\kappa})\psi_{\boldsymbol{\kappa}} \exp[\frac{-iE_e(\boldsymbol{\kappa})t}{\hbar}]$$
$$= \sum_{\boldsymbol{\kappa}} a_{\boldsymbol{\kappa}}(t)(\mathrm{H_o} + \varphi)\psi_{\boldsymbol{\kappa}} \exp[\frac{-iE_e(\boldsymbol{\kappa})t}{\hbar}]. \tag{A.6}$$

Multiplying by $\psi^*_{\boldsymbol{\kappa'}}$ and integrating over space, we have (using orthogonality of eigenfunctions)

$$i\hbar\frac{\partial a_{\boldsymbol{\kappa'}}(t)}{\partial t} \exp[\frac{-iE_e(\boldsymbol{\kappa'})t}{\hbar}] = \sum_{\boldsymbol{\kappa}} a_{\boldsymbol{\kappa}}(t) \exp[\frac{-iE_e(\boldsymbol{\kappa})t}{\hbar}]\langle\psi_{\boldsymbol{\kappa'}}|\varphi_s|\psi_{\boldsymbol{\kappa'}}\rangle. \tag{A.7}$$

The matrix element is defined as

$$M_{\kappa',\kappa} = \langle \psi_{\boldsymbol{\kappa'}} | \varphi | \psi_{\boldsymbol{\kappa}} \rangle \tag{A.8}$$

Equation (A.7) can be rewritten as

$$\frac{\partial a_{\boldsymbol{\kappa'}}(t)}{\partial t} = \frac{1}{i\hbar} \sum_{\boldsymbol{\kappa}} M_{\kappa',\kappa} a_{\boldsymbol{\kappa}}(t) \exp\{\frac{i[E_e(\boldsymbol{\kappa'}) - E_e(\boldsymbol{\kappa})]t}{\hbar}\}. \tag{A.9}$$

To study the time evolution of the problem, we assume that the perturbation φ is absent at time $t < 0$ and turned on at $t = 0$. With this assumption, the system is in a time-independent state up to $t = 0$. We assume that the system is in a single, well-defined state $\psi_{\boldsymbol{\kappa}}$

$$a_{\boldsymbol{\kappa}}(t = 0) = 1 \tag{A.10}$$

$$a_{\boldsymbol{\kappa'}}(t = 0) = 0 \text{ if } \boldsymbol{\kappa'} \neq \boldsymbol{\kappa}. \tag{A.11}$$

Integration of Eq. (A.9) to the first order gives

$$a_{\boldsymbol{\kappa'}}(t) = \frac{1}{i\hbar} \int_0^t M_{\kappa',\kappa} \exp\{\frac{i[E_e(\boldsymbol{\kappa'}) - E_e(\boldsymbol{\kappa})]t}{\hbar}\} \mathrm{d}t, \tag{A.12}$$

which satisfies the initial condition Eq. (A.11).

A.2 Transition Rate

A number of important problems in quantum mechanics involve a perturbation which has time dependence with a harmonic form. Examples include interactions of electrons with electromagnetic radiation (photons), electrons in crystals interacting with phonons, etc. In these cases, the time dependence of the perturbation potential

is

$$\varphi_s = \varphi_{\rm o} \exp(\mp i\omega t), \tag{A.13}$$

which gives the matrix element as

$$M_{\kappa',\kappa} = M^{\rm o}_{\kappa',\kappa} \exp(\mp i\omega t) \quad M^{\rm o}_{\kappa',\kappa} = \langle \psi_{\boldsymbol{\kappa'}} | \varphi_{\rm o} | \psi_{\boldsymbol{\kappa}} \rangle. \tag{A.14}$$

Hence Eq. (A.12) can be integrated as

$$a_{\boldsymbol{\kappa'}}(t) = \frac{1}{i\hbar} M^{\rm o}_{\kappa',\kappa} \frac{\exp\{\frac{i[E_e(\boldsymbol{\kappa'}) - E_e(\boldsymbol{\kappa}) \mp \hbar\omega]t}{\hbar}\} - 1}{\frac{i[E_e(\boldsymbol{\kappa'}) - E_e(\boldsymbol{\kappa}) \mp \hbar\omega]}{\hbar}}. \tag{A.15}$$

For simplicity of derivation, define

$$\omega' = \frac{[E_e(\boldsymbol{\kappa'}) - E_e(\boldsymbol{\kappa}) \mp \hbar\omega]}{\hbar}, \tag{A.16}$$

then Eq. (A.15) can be written as

$$a_{\boldsymbol{\kappa'}}(t) = \frac{1}{i\hbar} M^{\rm o}_{\kappa',\kappa} \exp(\frac{i\omega' t}{2}) \frac{\sin(\omega' t/2)}{\omega' t/2} t. \tag{A.17}$$

The transition rate is given by the transition probability per unit time, i.e.,

$$\dot{\gamma}_e(\boldsymbol{\kappa'}, \boldsymbol{\kappa}) = \lim_{t\to\infty} \frac{|a_{\boldsymbol{\kappa'}}(t)|^2}{t} = \lim_{t\to\infty} \frac{1}{t\hbar^2} |M^{\rm o}_{\kappa',\kappa}|^2 [\frac{\sin(\omega' t/2)}{\omega' t/2}]^2 t^2. \tag{A.18}$$

Note that

$$\int_{-\infty}^{+\infty} \frac{\sin^2 x}{x^2} {\rm d}x = \pi. \tag{A.19}$$

Then we find the following equality

$$\lim_{t\to\infty} [\frac{\sin(\omega' t/2)}{\omega' t/2}]^2 = \pi \delta_{\rm D}(\frac{\omega' t}{2}) = \frac{2\pi}{t} \delta_{\rm D}(\omega'). \tag{A.20}$$

Note that here we have used the relation

$$\delta_{\rm D}(ax) = \frac{1}{a}\delta_{\rm D}(x) \quad a \text{ is a constant.} \tag{A.21}$$

Hence, the transition rate Eq. (A.18) becomes

$$\begin{aligned} \dot{\gamma}_e(\boldsymbol{\kappa'}, \boldsymbol{\kappa}) &= \frac{1}{t\hbar^2}|M^{\rm o}_{\kappa',\kappa}|^2 \frac{2\pi}{t}\delta_{\rm D}\{\frac{[E_e(\boldsymbol{\kappa'}) - E_e(\boldsymbol{\kappa}) \mp \hbar\omega]}{\hbar}\}t^2 \\ &= \frac{2\pi}{\hbar}|M^{\rm o}_{\kappa',\kappa}|^2\delta_{\rm D}[E_e(\boldsymbol{\kappa'}) - E_e(\boldsymbol{\kappa}) \mp \hbar\omega]. \end{aligned} \tag{A.22}$$

This is the Fermi golden rule.

Bibliography

[1] Epstein, R., Buckwald, M., Edwards, B., Gosnell, T., and Mungan, C., 1995. "Observation of laser-induced fluorescent cooling of a solid". *Nature,* **377**, pp. 500–503.

[2] Gosnell, T., 1999. "Laser cooling of a solid by 65 K starting from room temperature". *Opt. Lett.,* **24**, pp. 1041–1043.

[3] Hoyt, C., ed., 2003. *PhD Dissertation: Laser Cooling in Thulium-doped Solids.* University of New Mexico, Albuquerque, NM.

[4] Pires, A., Serra, O., Heer, S., and Gudel, H., 2005. "Low-temperature upconversion spectroscopy of nanosized y_2o_3: Er,yb phosphor". *J. Appl. Phys.,* **98**, p. 063529.

[5] Lamouche, G., and Lavallard, P., 1998. "Low temperature laser cooling with a rare-earth doped glass". *J. Appl. Phys.,* **84**, pp. 509–516.

[6] Gauck, H., Gfroerer, T., Renn, M., Cornell, E., and Bertness, K., 1997. "External radiative quantum efficiency of 96% from a gaas/gainp heterostructure". *Appl. Phys. A,* **64**, pp. 143–147.

[7] Sheik-Bahae, M., 2005. "Laser cooling in semiconductors". *4th Annual Workshop on Laser Cooling of Solids*.

[8] Rand, S., 2003. "Bright storage of light". *Optics & Photonics News,* **May**, pp. 32–37.

[9] Chu, S., 1998. "The manipulation of neutral particles". *Reviews of Modern Physics,* **70**, pp. 685–706.

[10] Phillips, W., 1998. "Laser cooling and trapping of neutral atoms". *Reviews of Modern Physics,* **70**, pp. 721–741.

[11] Cornell, E., and Wieman, C., 2002. "Nobel lecture: Bose-einstein condensation in a dilute gas, the first 70 years and some recent experiments". *Reviews of Modern Physics,* **74**, pp. 875–893.

[12] Ketterle, W., 2002. "Nobel lecture: When atoms behave as waves: Bose-einstein condensation and the atom laser". *Reviews of Modern Physics,* **74**, pp. 1131–1151.

[13] Pringsheim, P., 1929. "Zwei bemerkungen uber den unterschied von lumineszenz und temperaturstrahlung". *Z. Phys.,* **57**, pp. 739–746.

[14] Vavilov, S., 1945. "Some remarks on the Stokes law". *J. Phys. (Moscow),* **9**, pp. 68–73.

[15] Vavilov, S., 1946. "Photoluminescence and thermodynamics". *J. Phys. (Moscow),* **10**, pp. 499–501.

[16] Landau, L., 1946. "On the thermodynamics of photoluminescence". *J. Phys. (Moscow),* **10**, pp. 503–506.

[17] Kushida, T., and Geusic, J., 1968. "Optical refrigeration in nd-doped yttrium aluminium garnet". *Phys. Rev. Lett.,* **21**, pp. 1172–1175.

[18] Djeu, N., and Whitney, W., 1981. "Laser cooling by spontaneous anti-stokes scattering". *Phys. Rev. Lett.,* **46**, pp. 236–239.

[19] Mungan, C., Buchwald, M., Edwards, B., Epstein, R., and Gosnell, T., 1997. "Internal laser cooling of Yb^{3+}-doped glass measured between 100 and 300 k". *Appl. Phys. Lett.,* **71**, pp. 1458–1460.

[20] Luo, X., Eisaman, M., and Gosnell, T., 1998. "Laser cooling of a solid by 21 k staring from room emperature". *Opt. Lett.,* **23**, pp. 639–641.

[21] Edwards, B., Anderson, J., Epstein, R., Mills, G., and Mord, A., 1999. "Demonstration of a solid-state optical cooler: an approach to cryogenic refrigeration". *J. Appl. Phys.,* **86**, pp. 6489–6493.

[22] Fernandez, J., Mendioroz, A., Garcia, A., Balda, R., and Adam, J., 2000. "Anti-Stokes laser-induced internal cooling of Yb^{3+}-doped glasses". *Phys. Rev. B,* **62**, pp. 3213–3217.

[23] Epstein, R., Brown, J., Edwards, B., and Gibbs, A., 2001. "Measurements of optical refrigeration in ytterbium-doped crystals". *J. Appl. Phys.,* **90**, pp. 4815–4819.

[24] Rayner, A., Friese, M., Truscott, A., Heckenberg, N., and H.Rubinsztein-Dunlop, 2001. "Laser cooling of a solid from ambient temperature". *Journal of Modern Optics,* **48**, pp. 103–114.

[25] Hoyt, C., Hasselbeck, M., Sheik-Bahae, M., Epstein, R., Greenfield, S., Thiede, J., Distel, J., and Valencia, J., 2003. "Advances in laser cooling of thulium-doped glass". *J. Opt. Soc. Am. B,* **20**, pp. 1066–1074.

[26] Heeg, B., Stone, M., Khizhnyak, A., Rumbles, G., Mills, G., and Debarber, P., 2004. "Experimental demonstration of intracavity solid-state laser cooling of Yb^{3+}: ZrF_4-BaF_2-LaF_3-AlF_3-NaF glass". *Phys. Rev. A,* **70**, pp. 021401(1–4).

[27] Thiede, J., Distel, J., Greenfield, S., and Epstein, R., 2005. "Cooling to 208 K by optical refrigeration". *Appl. Phys. Lett.,* **86**, p. 154107.

[28] Bowman, S., and Mungan, C., 2000. "New materials for optical cooling". *Appl. Phys. B,* **71**, pp. 807–811.

[29] Mendioroz, A., Fernandez, J., Voda, M., Al-Saleh, M., Balda, R., and Garcia-Adeva, A., 2002. "Anti-stokes laser cooling in yb^{3+}-doped kpb_2cl_5 crystal". *Opt. Lett.,* **27**, pp. 1525–1527.

[30] Sheik-Bahae, M., and Epstein, R., 2004. "Can laser light cool semiconductors?". *Phys. Rev. Lett.,* **368**, p. 247403.

[31] Merzbacher, E., 1998. *Quantum Mechanics*, third ed. John Wiley, New York.

[32] Ruan, X., and Kaviany, M., 2005. "Enhanced nonradiative relaxation and photoluminescence quenching in random, doped nanocrystalline powders". *J. Appl. Phys.,* **97**, pp. 104331–1–8).

[33] Kaviany, M., 2002. *Principles of Heat Transfer.* John Wiley, New York.

[34] Rayner, A., Heckenberg, N., and H.Rubinsztein-Dunlop, 2003. "Condensed-phase optical refrigeration". *J. Opt. Soc. Am. B,* **20**, pp. 1037–1053.

[35] Frey, R., Micheron, F., and Pocholle, J., 2000. "Comparison of peltier and anti-stokes optical coolings". *J. Appl. Phys.,* **87**, pp. 4489–4498.

[36] Bowman, S., 1999. "Laser without internal heat generation". *IEEE Journal of Quantum Electronics,* **35**, pp. 115–121.

[37] Lavi, R., and Jackel, S., 2000. "Thermally boosted pumping of neodymium lasers". *Applied Optics,* **39**, pp. 3093–3098.

[38] Lupei, V., Lupei, A., Pavel, N., Taira, T., Shoji, I., and Ikesue, A., 2001. "Laser emission under resonant pump in the emitting level of concentrated nd:yag ceramics". *Appl. Phys. Lett.,* **79**, pp. 590–592.

[39] Lupei, V., Pavel, N., and Taira, T., 2002. "Highly efficient continuous-wave 946 nm nd:yag laser emission under direct 885 nm pumping". *Appl. Phys. Lett.,* **81**, pp. 2677–2679.

[40] Lupei, V., 2003. "Efficiency enhancement and power scaling of nd lasers". *Optical Materials,* **24**, pp. 353–368.

[41] Li, C., Liu, Q., Gong, M., Chen, G., and Yan, P., 2004. "Modeling of radiation-balanced continuous-wave laser oscillators". *J. Opt. Soc. Am. B,* **21**, pp. 539–542.

[42] Maiman, T., 1960. "Molecular dynamics study of the structures and bbulk moduli of crystals in the system cao-mgo-al_2o_3-sio_2". *Nature,* **187**, pp. 493–494.

[43] Geusic, J., Marcos, H., and Vanuitert, L., 1964. "Laser oscillations in Nd-doped yttrium aluminum yttrium gallium + gadolinium garnets". *Appl. Phys. Lett.,* **4**, pp. 182–184.

[44] Mungan, C., Buchwald, M., Edwards, B., Epstein, R., and Gosnell, T., 1997. "Laser cooling of a solid by 16 k starting from room temperature". *Phys. Rev. Lett.,* **78**, pp. 1030–1033.

[45] Fernandez, J., Mendioroz, A., Garcia, A., Balda, R., Adam, J., and Arriandiaga, M., 2001. "On the origin of anti-stokes laser-induced cooling of yb^{3+}-doped glass". *Optical Materials,* **16**, pp. 173–179.

[46] Heeg, B., Rumbles, G., Khizhnyak, A., and DeBarber, A., 2002. "Comparative intra- versus extra-cavity laser cooling efficiencies". *J. App. Phys.,* **91**, pp. 3356–3362.

[47] Ruan, X., and Kaviany, M., 2006. "Enhanced laser cooling of rare-earth-ion-doped nanocrystalline powders". *Phys. Rev. B,* **73**, pp. 002619–1–15.

[48] Heeg, B., and Rumbles, G., 2003. "Influence of radiative transfer on optical cooling in the condensed phase". *J. App. Phys.,* **93**, pp. 1966–1973.

[49] Heeg, B., Debarber, P., and Rumbles, G., 2005. "Influence of fluorescence reabsorption and trapping on solid-state optical cooling". *Appl. Opt.,* **44**, pp. 3117–3124.

[50] Rivlin, L., and Zadernovsky, A., 1997. "Laser cooling of semiconductors". *Opt. Comm.,* **139**, pp. 219–222.

[51] Finkeiβen, E., Potemski, M., Wyder, P., Vina, L., and Weimann, G., 1999. "Cooling of a semiconductor by luminescence up-conversion". *Appl. Phys. Lett.,* **75**, pp. 1258–1260.

[52] Boltzmann, L., 1995. *Lectures on Gas Theory.* Dover, New York.

[53] Shannon, C., 1948. "A mathematical theory of communication". *Bell System Technical Journal,* **27**, pp. 379–423.

[54] Shannon, C., 1948. "A mathematical theory of communication". *Bell System Technical Journal,* **27**, pp. 623–656.

[55] Bekenstein, J., 2005. "Information in the holographic universe". *Scientific American,* **15**, pp. 74–?

[56] Metcalf, H., and van der Straten, P., 1999. *Laser Cooling and Trapping.* Springer-Verlag, New York.

[57] Mungan, C., 2005. "Radiation thermodynamics with applications to lasing and fluorescent cooling". *Am. J. Phys.,* **73**, pp. 1458–1460.

[58] Loudon, R., 1983. *The Quantum Theory of Light.* Oxford University Press, Oxford.

[59] Landsberg, P., and Tonge, G., 1980. "Thermodynamic energy conversion efficiencies". *J. Appl. Phys.,* **51**, pp. R1–R20.

[60] Essex, C., Kennedy, D., and Berry, R., 2003. "How hot is radiation?". *Am. J. Phys.,* **71**, pp. 969–978.

[61] Cao, H., Zhao, Y., Ho, S., Seelig, E., Wang, Q., and Chang, R., 1999. "Random laser action in semiconductor powder". *Phys. Rev. Lett.,* **82**, pp. 2278–2281.

[62] Noginov, M., 2005. *Solid State Random Lasers.* Springer, New York.

[63] Hehlen, M., Gudel, H., Shu, Q., and Rand, S., 1996. "Cooperative optical bistability in the dimer system $Cs_3Y_2Br_9$:10% Yb^{3+}". *J. Chem. Phys.,* **104**, pp. 1232–1244.

[64] Griffiths, D., 1995. *Introduction to Quantum Mechanics.* Prentice Hall, Upper Saddle River, New Jersey.

[65] Hayt, W., and Buck, J., 2001. *Engineering Electromagnetics.* Mcgraw-Hill, Boston.

[66] Zych, E., 2001. "On the reasons for low luminescence efficiency in combustion-made Lu_2O_3: Tb". *Opt. Mat.,* **16**, pp. 445–452.

[67] DiBartolo, B., 1968. *Optical Interaction in Solids.* John Wiley, New York.

[68] Powell, R., 1998. *Physics of Solid-State Laser Materials.* Spinger-Verlag, New York.

[69] Montoya, E., Agullo-Rueda, F., Manotas, S., Sole, J. G., and Bausa, L., 2001. "Electron-phonon coupling in Yb^{3+}: $LiNbO_3$ laser crystal". *J. Luminescence,* **94-95**, pp. 701–705.

[70] Frisch, M., Trucks, G., Schlegel, H., Scuseria, G., Robb, M., Cheeseman, J., Montgomery, J., Vreven, T., Kudin, K., Burant, J., Millam, J., Iyengar, S., Tomasi, J., Barone, V., Mennucci, B., Cossi, M., Scalmani, G., Rega, N., Petersson, G., Nakatsuji, H., Hada, M., Ehara, M., Toyota, K., Fukuda, R., Hasegawa, J., Ishida, M., Nakajima, T., Honda, Y., Kitao, O., Nakai, H., Klene, M., Li, X., Knox, J., Hratchian, H., Cross, J., Adamo, C., Jaramillo, J., Gomperts, R., Stratmann, R., Yazyev, O., Austin, A., Cammi, R., Pomelli, C., Ochterski, J., Ayala, P., Morokuma, K., Voth, G., Salvador, P., Dannenberg, J., Zakrzewski, V., Dapprich, S., Daniels, A., Strain, M., Farkas, O., Malick, D., Rabuck, A., Raghavachari, K., Foresman, J., Ortiz, J., Cui, Q., Baboul, A., Clifford, S., Cioslowski, J., Stefanov, B., Liu, G., Liashenko, A., Piskorz, P., Komaromi, I., Martin, R., Fox, D., Keith, T., Al-Laham, M., Peng, C., Nanayakkara, A., Challacombe, M., Gill, P., Johnson, B., Chen, W., Wong, M., Gonzalez, C., and Pople, J. A., 2004. *Gaussian 03, Revision C.02.* Gaussian, Inc., Wallingford CT.

[71] Tregenna-Piggott, P., Best, S., O'Brien, M., Knight, K., Forsyth, J., and Pilbrow, J.", 1997.". *J. Am. Chem. Soc.,* **119**, p. 3324.

[72] Tachikawa, H., Ichikawa, T., and Yoshida, H., 1990. "Geometrical structure and electronic states of the hydrated titanium(iii) ion. an ab initio ci study". *J. Am. Chem. Soc.,* **112**, pp. 982–987.

[73] Kallies, B., and Meier, R., 2001. "Electronic structure of 3d $[M(H_2O)_6]^{3+}$ ions from Sc^{III}: A quantum mechanical study based on dft computations and natural bond orbital analyses". *Inorg. Chem,* **40**, pp. 3101–3112.

[74] Gray, H., 1964. *Electrons and Chemical Bonding.* W.A. Benjamin, Inc., New York.

[75] Hilborn, R., 1982. "Einstein coefficients, cross sections, f values, dipole moments, and all that". *Am. J. Phys.,* **50**, pp. 982–986.

[76] Powell, R., Venikouas, G., Xi, L., and Tyminski, J., 1986. "Thermal effects on the optical spectra of al2o3:ti3+". *J. Chem. Phys.,* **84**, pp. 662–665.

[77] Moulton, P., 1986. "Spectroscopic and laser characteristics of Ti:Al_2O_3". *J. Opt. Soc. Am. B,* **3**, pp. 125–133.

[78] Lin, S., 1966. "Rate of interconversion of electronic and vibrational energy". *J. Chem. Phys.,* **44**, pp. 3759–3767.

[79] van de Hulst, H., 1981. *Light Scattering by Small Particles.* Dover Publications Inc., New York.

[80] Kumar, S., and Tien, C., 1990. "Dependent absorption and extinction of radiation by small particles". *Journal of Heat Transfer-Transactions of the ASME,* **112**, pp. 178–185.

[81] Mishchenko, M., Travis, L., and Lacis, A., 2002. *Scattering, Absorption, and Emission of Light by Small Particles*. Cambridge University Press, New York.

[82] Sheng, P., 1995. *Introduction to Wave Scattering, Localization, and Mesoscopic Phenomena*. Academic Press, San Diego.

[83] Zhang, D., Hu, W., Zhang, Y., Li, Z., Cheng, B., and Yang, G., 1994. "Experimental verification of light localization for disordered multilayers in the visible-infrared spectrum". *Phys. Rev. B,* **50**, pp. 9810–9814.

[84] Wiersma, D., Bartolini, P., Lagendijk, A., and Righini, R., 1997. "Localization of light in a disordered medium". *Nature,* **390**, pp. 671–673.

[85] Anderson, P., 1958. "Absence of diffusion in certain random lattices". *Phys. Rev.,* **109**, pp. 1492–1505.

[86] McGurn, A., Christensen, K., Mueller, F., and Maradudin, A., 1993. "Anderson localization in one-dimensional randomly disordered optical systems that are periodic on average". *Physical Review B,* **47**, pp. 13120–13125.

[87] Sigalas, M., and Soukoulis, C., 1995. "Elastic-wave propagation through disordered and/or absorptive layered systems". *Phy. Rev. B,* **51**, pp. 2780–2789.

[88] van Tiggelen, B., Lagendijk, A., and Wiersma, D., 2000. "Reflection and transmission of waves near the localization threshold". *Phys. Rev. Lett.,* **84**, pp. 4333–4336.

[89] Chang, S., Cao, H., and Ho, S., 2003. "Cavity formation and light propagation in partially ordered and completely random one-dimensional systems". *IEEE Journal of Quantum Electronics,* **39**, pp. 364–374.

[90] Yannopapas, V., Modinos, A., and Stefanou, N., 2003. "Anderson localization of light in inverted opals". *Phy. Rev. B,* **68**, p. 193205.

[91] Skipetrov, S., and van Tiggelen, B., 2004. "Dynamics of weakly localized waves". *Phy. Rev. Lett.,* **92**, p. 113901.

[92] McGurn, A., Sheng, P., and Maradudin, A., 1992. "Strong localization of light in two-dimensional disordered dielectric media". *Optical Communications,* **91**, pp. 175–179.

[93] Sigalas, M., Soukoulis, C., Chan, C., and Turner, D., 1996. "Localization of electromagnetic waves in two-dimensional disordered systems". *Phy. Rev. B,* **53**, pp. 8340–8348.

[94] Rusek, M., and Orlowski, A., 1999. "Anderson localization of electromagnetic waves in confined dielectric media". *Phys. Rev. E,* **59**, pp. 3655–3660.

[95] Wang, K., and Ye, Z., 2003. "Simulation study of localization of electromagnetic waves in two-dimensional random dipolar systems". *Phys. Rev. E,* **68**, p. 066609.

[96] Ye, Z., and Gupta, B., 2003. "About wave localization in two-dimensional random media". *Phys. Lett. A,* **313**, pp. 485–490.

[97] Haney, M., and Snieder, R., 2003. "Breakdown of wave diffusion in 2d due to loops". *Phys. Rev. Lett.,* **91**, p. 093902.

[98] Wang, K., and Ye, Z., 2003. "Diffusive and localization behavior of electromagnetic waves in a two-dimensional random medium". *Phys. Rev. E,* **68**, p. 046608.

[99] Vlasov, Y., Kaliteevski, M., and Nikolaev, V., 1999. "Different regimes of light localization in a disordered photonic crystal". *Phys. Rev. B,* **60**, pp. 1555–1562.

[100] Schuurmans, F., Megens, M., Vanmaekelbergh, D., and Lagendijk, A., 1999. "Light scattering near the localization transition in macroporous gap networks". *Phys. Rev. Lett.,* **83**, pp. 2183–2186.

[101] Chabanov, A., Stoytcher, M., and Genack, A., 2000. "Statistical signitures of photon localization". *Nature,* **404**, pp. 850–853.

[102] Chabanov, A., and Genack, A., 2001. "Photon localization in resonant media". *Phys. Rev. Lett.,* **87**, p. 153901.

[103] Wiersma, D., Vanalbada, M., and Lagendijk, A., 1995. "Random laser". *Nature,* **373**, pp. 203–204.

[104] Burin, A., Ratner, M., Cao, H., and Chang, S., 2002. "Random laser in one dimension". *Phys. Rev. Lett.,* **88**, p. 093904.

[105] Cao, H., Xu, J., Ling, Y., Burin, A., Seeling, E., Liu, X., and Chang, R., 2003. "Random lasers with coherent feedback". *IEEE Journal of Selected Topics in Quantum Electronics,* **9**, pp. 111–119.

[106] van Soest, G., Poelwijk, F., and Lagendijk, A., 2002. "Speckle experiments in random lasers". *Phy. Rev. E,* **65**, p. 046603.

[107] Mujumdar, S., Cavalieri, S., and Wiersma, D., 2004. "Temperature-tunable random lasing: Numerical calculations and experiments". *Journal of the Optical Society of America B-Optical Physics,* **21**, pp. 201–207.

[108] Noginov, M., Zhu, G., Frantz, A., Novak, J., Williams, S., and Fowlkes, I., 2004. "Dependence of ndsc3(bo3)4 random laser parameters on particle size". *Journal of the Optical Society of America B-Optical Physics,* **21**, pp. 191–200.

[109] Patra, M., 2002. "Theory of photon statistics of random lasers". *Phys. Rev. A,* **65**, p. 043809.

[110] Feng, Y., Bisson, J., Lu, J., Huang, S., Takaichi, K., Shirakawa, A., Musha, M., and Ueda, K., 2004. "Thermal effects in quasi-continuous-wave nd^{3+}: $Y_3al_5o_12$ nanocrystalline-powder random laser". *Appl. Phys. Lett.,* **84**, pp. 1040–1042.

[111] Redmond, S., Armstrong, G., Chan, H., Mattson, E., Mock, A., Li, B., Potts, R., Cui, M., Rand, S., Oliveira, S., Marchal, J., Hinklin, T., and Laine, R., 2004. "Electrical generation of stationary light in random scattering media". *J. Opt. Soc. Am. B,* **21**, pp. 214–222.

[112] Kaviany, M., 1995. *Principles of Heat Transfer in Porous Media*. Springer, New York.

[113] Maxwell-Garnett, J., 1904. "Colours in metal glasses and in metallic films". *Philosophical Transactions of the Royal Society of London, Series A, Comtaining Papers of a Mathematical or Physical Character,* **203**, pp. 385–420.

[114] Levy, O., and Stroud, D., 1997. "Maxwell garnett theory for mixtures of anisotropic inclusions: Application to conducting polymers". *Phys. Rev. B,* **56**, pp. 8035–8046.

[115] Ruan, X., and Kaviany, M., 2005. "Photon localization and electromagnetic field enhancement in laser irradiated, random porous media". *Microscale Thermophysical Engineering,* **9**, pp. 63–84.

[116] Williams, G., Bayram, S., Rand, S., Hinklin, T., and Laine, R., 2002. "Laser action in strongly scattering rare-earth-metal-doped dielectric nanophosphors". *Phys. Rev. A,* **65**, p. 013807.

[117] Li, B., Williams, G., Rand, S., Hinklin, T., and Laine, R., 2002. "Continuous-wave ultraviolet laser action in strongly scattering nd-doped alumina". *Opt. Lett.,* **27**, pp. 394–396.

[118] Zhang, Z., and Flik, M., 1993. "Predicted absorption of $YBa_2Cu_3O_7$/YSZ/Si multilayer structures for infrared detectors". *IEEE Transactions on Applied Superconductivity,* **3**, pp. 1604–1607.

[119] Kong, J., 2000. *Electromagnetic Wave Theory*. EMW Publishing, Cambridge.

[120] Hecht, E., 2002. *Optics*. Addison Wesley, San Francisco.

[121] Kraus, J., and Fleisch, D., 1999. *Electromagnetics with Applications*. MaGraw-Hill, Boston.

[122] Kittel, C., 1996. *Introduction to Solid State Physics*. John Wiley, New York.

[123] Yang, H., Hong, K., Feofilov, S., Tissue, B., Meltzer, R., and Dennis, W., 1999. "Electron-phonon interaction in rare earth doped nanocrystals". *J. Luminescence,* **83-84**, pp. 139–145.

[124] Loong, C., Vashishta, P., Kalia, R., Jin, W., Degani, M., Hinks, D., Price, D., Jorgensen, J., Dabrowski, B., Mitchell, A., Richards, D., and Zheng, Y., 1992. "Phonon density of states and oxgen-isotope effect in $Ba_{1-x}K_xBiO_3$". *Phys. Rev. B,* **45**, pp. 8052–8064.

[125] Allen, M., and Tildesley, D., 1991. *Computer Simulation of Liquids*. Clarendon, Oxford.

[126] Meyer, R., Lewis, L., Prakash, S., and Entel, P., 2003. "Vibrational properties of nanoscale materials: from nanoparticles to nanocrystalline materials". *Phys. Rev. B,* **68**, pp. 104303(1–9).

[127] Paton, M., and Maslen, E., 1965. "A refinedment of crystal structure of yttria". *Acta Cryst.,* **19**, pp. 307–310.

[128] O'Connor, B., and Valentine, T., 1969. "A neutron diffraction study of crystal structure of c-form of yttrium sesquioxide". *Acta Crystallogr., Sect. B: Struct. Crystallogr. Cryst. Chem.,* **B25**, p. 2140.

[129] Konard, A., Herr, U., Tidecks, R., Kummer, F., and Samwer, K., 2001. "Luminescence of bulk and nanocrystalline cubic yttria". *J. Appl. Phys.,* **90**, pp. 3516–3523.

[130] Chou, F., Lukes, J., Liang, X., Takahashi, K., and Tien, C., 1999. "Molecular dynamics in microscale thermophysical engineering". *Ann. Rev. Heat Transfer,* **10**, pp. 141–176.

[131] Buckingham, R.", 1938.". *Proc. R. Soc. London, Ser. A,* **168**, p. 234.

[132] Lewis, G., and Catlow, C., 1985. "Potential models for ionic oxides". *J. Phys. C,* **18**, pp. 1149–1161.

[133] Brinkman, H., Briels, W., and Verweij, H., 1995. "Molecular dynamics simulations of yttria-stabilized zirconia". *Chem. Phys. Lett.,* **247**, pp. 386–390.

[134] Kilo, M., Jackson, R. A., and Borchardt, G., 2003. "Computer modelling of ion migration in zirconia". *Philosophical Magzine,* **83**.

[135] McGaughey, A., and Kaviany, M., 2004. "Thermal conductivity decomposition and analysis using molecular dynamics simulations. part i. lennard-jones argon". *Int. J. Heat and Mass Transfer,* **47**, pp. 1783–1798.

[136] Auzel, F., 2002. "A fundamental self-generated quenching center for lanthanide-doped high-purity solids". *Journal of Luminescence,* **100**, pp. 125–130.

[137] Boulon, G., Guyot, Y., Ito, M., Bensalah, A., Goutaudier, C., Panczer, G., and Gacon, J., 2004. "From optical spectroscopy to a concentration quenching model and a theoretical approach to laser optimization for Yb^{3+}-doped $YLiF_4$ crystals". *Molecular Physics,* **102**, pp. 1119–1132.

[138] Lei, G., Anderson, J., Buchwald, M., Edwards, B., Epstein, R., Murtagh, M., and Sigel, G., 1998. "Spectroscopic evaluation of yb^{3+}-doped glasses for optical refrigeration". *IEEE J. Quantum Electron.,* **34**, pp. 1839–1845.

[139] Nurtdinova, L., Semashko, V., Naumov, A., Abdulsabirov, R., and Korableva, S., 2005. "Spectroscopic indications of the possible optical cooling effect in fluoride crystals activated by yb^{3+} and tm^{3+} ions". *Physics of the Solid State,* **47**, pp. 1463–1466.

[140] Zhang, W., Zhang, W., Xie, P., Yin, M., Chen, H., L.Jing, Zhang, Y., Lou, L., and Xia, S., 2003. "Optical properties of nanocrystalline y_2o_3:eu depending on its odd structure". *J. Colloid Interface Sci.,* **262**, pp. 588–593.

[141] Kuklja, M., and Pandey, R., 1999. "Atomistic modeling of native point defects in yttrium aluminum garnet crystals". *J. Am. Ceram. Soc.,* **82**, pp. 2881–2886.

[142] Kuklja, M., 2000. "Defects in yttrium aluminium perovskite and garnet crystals: Atomistic study". *J. Phys.: Condens. Matter,* **12**, pp. 2953–2967.

[143] Lundstrom, M., 2000. *Fundamentals of Carrier Transport*, second edition ed. Cambridge University Press, Cambridge, MA.

[144] Cohen-Tannoudji, C., Diu, B., and Laloe, F., 1992. *Quantum Mechanics*. Wiley, New York.